공학박사 학위논문

Study on Growth, Atomic Structure, and Catalytic Properties of Strained Heterostructured Oxide Nanocrystals

변형된 이종구조 산화물 나노 결정의 성장,
원자 구조 및 촉매 특성에 관한 연구

2020 년 8 월

서울대학교 대학원
화학생물공학부
조 민 지

Abstract of the Dissertation

Study on Growth, Atomic Structure, and Catalytic Properties of Strained Heterostructured Oxide Nanocrystals

by

Min Gee Cho

Doctor of Philosophy

School of Chemical and Biological Engineering

The Graduate School

Seoul National University

Strain engineering of the inorganic nanocrystal is a promising approach necessary to address emerging global energy, resource, and environmental issues. When different materials are combined to produce heterostructured

nanocrystal, the epitaxially-strained lattices can be formed at the heterointerface. In particular, the strain effect at the nanoscale can alter the surface lattice spacing and tune the electronic structure of the surface atoms, thus modifying the catalytic activity. The strain can be tuned by a lattice mismatch between the substrate and the overgrowth phase with a different crystal structure or crystallographic orientation. The strain engineering has been developed in heterostructured nanocrystals with different material combinations, including metals, semiconductors, and oxides. However, studies on the strained structure in oxide nanocrystals are limited because the synthesis of such structures has not been well established. In this thesis, I have designed and synthesized a model system that could investigate the strain effect on the regulation of the surface electronic structure for the design of better catalysts. The strained heterostructured oxide nanocrystals were produced using seed-mediated growth. The unique structure of these nanocrystals has been successfully studied with electron microscopy.

The first part of this thesis is an overview of epitaxial growth in thin-film technology and its analogy to three-dimensional (3D) polyhedral epitaxial growth. Chapter 2 describes the design principles for producing highly ordered multigrain nanostructures. Identification of the principles was achieved by synthesizing the nanocrystals with misfit-strain-induced uniform grain boundary defects, imaging the deformed structure at the nanometer scale using

a scanning transmission electron microscopy (STEM), and measuring the strain field. The seed-mediated approach was used to grow Mn_3O_4 grains on a cubic Co_3O_4 nanocrystal core. The facets of the cube nanocrystal substrates can guide the growth direction of the shell, creating a gap between the lattices of the adjacent Mn_3O_4 grains. Unlike the previous studies on the heteroepitaxial strains, the grain boundary (GB) defects in this new multigrain nanocrystal were induced by the geometric misfit strain between the adjacent Mn_3O_4 grains. Since the defects occur along the edges of the core, a uniform core shape is a prerequisite for achieving uniform GB defects. The strain tensor near the GB lattices reveals that the Mn_3O_4 shell accommodates a large epitaxial strain per GB without dislocation.

Chapter 3 presents the epitaxially strained CeO_2/Mn_3O_4 nanocrystals for antioxidant applications. The Mn_3O_4 lattices are highly strained due to the large lattice mismatch between CeO_2 and Mn_3O_4. The heterostructured nanocrystals with different compositions were prepared to study the strain effect by comparing the surface oxygen vacancy and the characteristics of surface reducibility. Due to the enhanced ability to scavenge the reactive oxygen species (ROS), the nanocrystal with strained Mn_3O_4 layer can protect the hematopoietic intestinal stem cells from irradiation.

Keywords: Epitaxial growth, heterostructured oxide nanocrystals, multigrain nanocrystals, strain engineering, atomic-scale imaging, electrocatalysis.

Student Number: 2012-22587

Contents

List of Tables

List of Figures

Chapter 1 Introduction: Synthetic Methods for Epitaxially Strained Heterostructured Nanocrystals

1.1 Thin-film epitaxy in nanomaterials

Over the last several decades, the study of thin-film epitaxy has been of great interest in the field of two-dimensional (2D)-based materials.[1] Deposition of secondary material with a well-defined orientation on a crystalline substrate material results in the formation of the epitaxial thin film. The epitaxially grown layer will have a single crystallographic orientation with respect to the substrate. For non-epitaxial growth, the overgrowth phase will be amorphous or multiple crystalline films. In most cases of epitaxy, crystal growth is performed with different material compounds than the substrate, which is called heteroepitaxy.[2]

1.1.1 Thin-film deposition techniques

1.1.1.1 Vapor phase deposition

Epitaxial growth of thin film on a substrate is performed with typical thin-film deposition techniques that include both depositions of epitaxial and non-epitaxial layers. The deposition techniques can be categorized into two broad categories—chemical and physical processes. For the chemical deposition, there are plating, chemical solution deposition (CSD), chemical vapor

deposition (CVD), and atomic layer deposition. Physical deposition includes molecular beam epitaxy (MBE), pulsed laser deposition, and sputtering. Both chemical and physical vapor deposition (PVD) is a technique commonly used for their homogeneous coating capability with the controlled thickness of the thin layer.

Although the vapor deposition technique is used to produce high-quality and high-performance materials, there are some limitations. For example, the PVD technique involves the process of vaporizing the condensed phase and then condensing the vapor phase back to a thin film on the substrate. Because the technique is based on a line-of-sight transfer between target and substrate, there can be a geometric shadowing effect, leading to a lack of directional variation and conformal coating capability. In the CVD technique, the volatile precursors of the secondary material are transferred to the substrate surface, and chemically modified to adsorb on the surface, producing the desired film. The film can be coated with a conformal and precision surface and endure harsh environments, including low/high temperature and high stress. However, chemical modification usually has limitations such as the reaction with other volatile precursors, high temperature required process, and the inability to mask the coating sites.

1.1.1.2 Solution phase deposition

On the other hand, the chemical solution deposition (CSD) is characterized by the process of chemical transformations of precursors dissolved or suspended in a solvent. These techniques range from the sol-gel process to the metal-organic decomposition. For the fabrication of thin-film oxide, the sol-gel process is known as a very effective deposition method in terms of low cost, scalability, and controllability of the composition, structure, and morphology. In addition, the chemical modification occurs at a relatively low temperature and the thermally induced structural disorder of the substrate can also be minimized. The sol-gel process, also known as wet chemistry, involves the formation of a colloidal suspension by dissolving secondary precursor compounds, such as alkoxides, metal salts, or other suitable reagents, in an appropriate solvent. The dissolution of metal cations by water or alcohol molecules produces hydroxo (OH^-) or oxo (O^{2-}) ligands by hydrolysis, resulting in the conversion of metal cations to metal hydroxides.[3] Following the hydrolysis of the precursor solution (sol), the sol particles, the metal hydroxides, are transformed into a gel-like phase (gel) by condensation and then into a solid thin film on a substrate. The condensation step leads to the formation of M–O–M bonds and produces water or alcohol molecules. In this thesis, the work is done with the sol-gel process.

1.1.2 Growth modes

In thin-film epitaxy, the epitaxial growth of materials is considered as a promising approach to producing heterostructures with the desired composition, structures, and interfaces. When thin films grow epitaxially on a crystal surface (substrate), the deposition films tend to follow the crystallographic arrangement of the substrate material. This growth behavior is governed by the interaction strength between the secondary material monomer (adsorbate) and the surface of the substrate, as well as the surface energy of both the substrate and the deposited film. Dictating the growth mechanism by which the thin film will follow requires the consideration of the change of the total Gibbs free surface energy.[4,5]

$$\Delta G = \gamma_1 - \gamma_2 + \gamma_{12}$$

where γ_1 and γ_2 are the surface energies of the substrate and the deposited film, respectively, and γ_{12} is the interfacial energy between the substrate and the deposited film. The growth mode falls into three types: i) Volmer-Weber growth, ii) Frank-van der Merwe growth, and iii) Stranski-Krastanov growth (Figure 1.1).

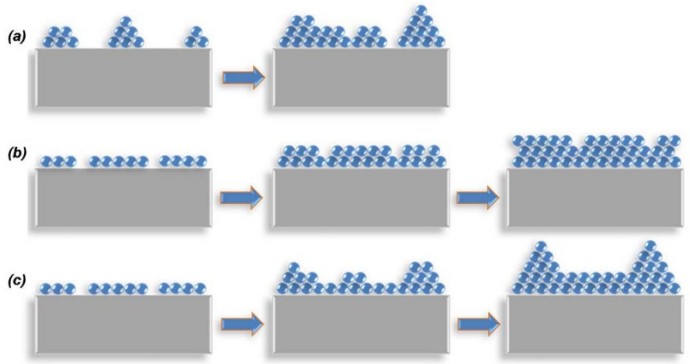

Figure 1.1. Three primary growth modes for thin-film deposition. Illustrations of the basic growth modes including (a) Volmer–Weber (island), (b) Frank–Van der Merwe (layer-by-layer), and (c) Stranski–Krastanov (layer-plus-island) growth. (From ref. [1] L. W. Martin, Y. H. Chu, R. Ramesh, *Mater. Sci. Eng. R Reports.* **68**, 89–133 (2010).)

1.1.2.1 Volmer-Weber growth

In Volmer-Weber (VW) growth, i.e., the three-dimensional (3D) island growth, the film grows on a large lattice-mismatched substrate and does not wet the substrate surface (γ_{12} is high).[6] In the early stages of the film formation, adatoms of the deposited material are physically adsorbed on the substrate. After physisorption, the adatoms can diffuse on the surface or form chemical bonds with the substrate (chemisorption) to form nuclei. In this growth mode, the absorbate–absorbate interactions are often stronger than the absorbate–substrate interactions, forming 3D islands on the substrate. The epitaxial growth also depends on the surface energy of the substrate and film. In the VW mode, the secondary material exposes a surface with higher energy than the substrate surface ($\gamma_2 > \gamma_1$). The difference in total Gibbs free energy is negative ($\Delta G < 0$). For example, the surface energy of the Au cluster is much higher than that of the TiO_2 substrate and therefore the growth of Au film on the TiO_2 substrate proceeds as an island growth mode.[7]

1.1.2.2 Frank-van der Merwe growth

Frank-van der Merwe (FM) growth, often referred to as layer-by-layer growth, has well-balanced adsorbate–substrate and adsorbate–adsorbate interactions. If the secondary material deposits on the same material or on a well lattice-matched substrate (γ_{12} is small), it tends to form continuous layers

over the substrate surface. In most cases of FM growth, adatoms prefer to deposit on the substrate surface rather than the film surface. By doing so, it exposes the lower energy surface ($\gamma_2 < \gamma_1$), which is the film surface, resulting in the complete wetting of the substrate. Since the adhesion force is stronger than the cohesion force, the sequential formation of the 2D layer is thermodynamically favored, thus achieving uniform coverage. The sign of total Gibbs free energy change for FM growth is positive ($\Delta G > 0$).

1.1.2.3 Stranski-Krastanov growth

The incomplete wetting ($\Delta G < 0$) promotes the 3D island growth (VW mode). If the lattice misfit between the substrate and the deposited layer is small enough, the layer-by-layer growth (FW mode) is favored, which is the case of complete wetting ($\Delta G > 0$). The film deposition will follow the Stranski-Krastanov (SK) growth mode when there is a significant misfit. The SK growth mode includes both 2D layer and 3D island growth. In the early stages of the film deposition, the surface adhesion force is stronger than the adatom cohesion force, leading to the layer-by-layer growth ($\Delta G > 0$). As the 2D layer thickens, the 2D layer growth proceeds to 3D island growth ($\Delta G < 0$), where islands are formed at the top of the 2D layer. This transition depends on the interplay between strain and surface energy.[8,9] While the epitaxial film grows following the FM mode, the deposited layer is forced to match the

lattice of the substrate. As a result, the layer becomes elastically strained to fit the substrate. A wetting layer, a homogeneously strained layer without dislocation, is pseudomorphous to the substrate. The elastic strain energy increases as the layer thickens. The deposited material grows as a coherent layer up to the critical layer thickness (h_c), where the strained layer cannot accommodate the accumulated strain. The critical thickness of pseudomorphous growth depends on the lattice misfit, with a smaller misfit leading to a thicker wetting layer. When grown above the critical thickness, 3D islands are formed to relax the misfit strains to reduce the total energy.[8]

The strain relaxation by the formation of the island often accompanies misfit dislocations with lower energy. By introducing dislocations at the interface between the wetting layer and the 3D island, strain energy is reduced at the expense of increased surface energy of the islands (Figure 1.2). In nanometer-scale heteroepitaxy, islands without misfit dislocations can be formed on the wetting layer. In 1990, Eaglesham and Cerullo reported the deposition of dislocation-free Ge islands on Si (001) substrate.[10] The strain relaxation takes place in the island, producing elastic deformation of the wetting layer and the island (Figure 1.3). The deformation and the free lateral surface of coherent 3D islands can partially lower the elastic strain energy of the island and the total free energy.

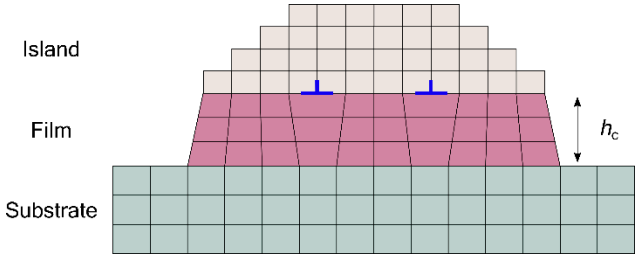

Figure 1.2. Illustration showing island formation in SK growth beyond the critical layer thickness (h_c). Edge dislocations (blue line) are formed at the interface of coherent film and island.

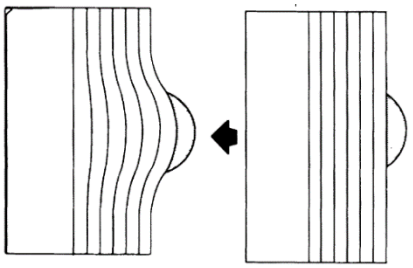

Figure 1.3. Schematic showing island strain relaxation by local elastic deformation of near-surface layers in the substrate. This shows how (100) planes can acquire radius of curvature, partially accommodating lattice mismatch and leading to coherent SK growth. (From ref. [10] D. J. Eaglesham, M. Cerullo, *Phys. Rev. Lett.* **64**, 1943–1946 (1990).)

In the heteroepitaxy, the misfit strain between the substrate and the overgrowth phase influences the epitaxial growth of thin films, which determines the shape evolution of the 3D islands. In previous research, the shape transition of the islands takes place depending on the size of the island during the growth process (Figure 1.4).[11,12] The shape transition occurs because the balancing between the strain energy and the surface and interface energy changes as the island grows. Considering not only thermodynamic but also the kinetic aspects—deposition rate of secondary material precursor and/or diffusivity of the adatom—of island growth, the faceting of the islands can be further controlled for the desired applications.[13]

The strained island in SK growth offers an attractive route for the production of uniform quantum dots. Using prepatterned substrates with ordered pit arrays and stripes can direct the nucleation and growth of the island to the predetermined sites.[14-16] Surface engineering for substrate prepatterning includes dislocation networks[17,18] or patterned topographic surface features[19]. This strategy often extends to produce periodic ripple patterns that exhibit interesting physical properties.[16]

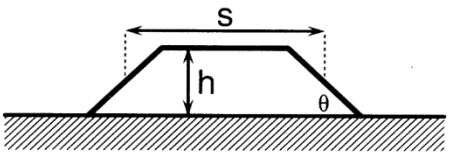

Figure 1.4. Schematic of assumed crystal shape, showing cross section in xz plane, and illustrating definition of width s, height h, and contact angle θ. (From ref. [11] J. Tersoff, R. M. Tromp, *Phys. Rev. Lett.* **70**, 2782–2785 (1993))

1.2 Strain engineering

1.2.1 Synthesis of heterostructured nanocrystals

Heterostructured nanomaterials have been widely studied due to their potential candidates for the applications, including catalysis, electronics, and magnetics.[20-23] The interface between the two different phases plays an important role in altering the physicochemical properties of the materials which affect the activity and stability of the catalytic performance.[24] Figure 1.5 shows that catalytic activity of CeO_2-based nanoparticles toward CO oxidation is directly affected by the perimeter metal atoms at the metal and support (CeO_2) interface.[25]

In thin-film epitaxy, the CVD method has been widely used for the strain engineering of atomically thin 2D materials.[26] Theoretical study on structural phase transitions of 2D Mo- and W-dichalcogenide monolayers suggested that transformation of a semiconducting and metallic crystal structure can be achieved via the in-plane epitaxial strain (Figure 1.6).[27]

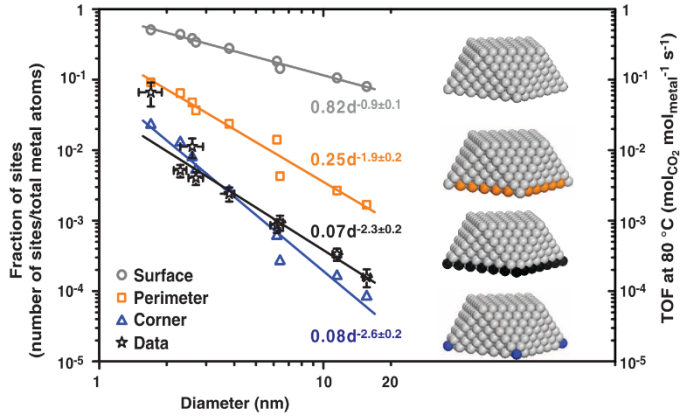

Figure 1.5. Plot showing the fraction of sites with a particular position as a function of particle size for ceria-based samples. Calculated number of sites with a particular geometry (surface and perimeter or corner atoms in contact with the support) as a function of diameter and turnover frequency at 80°C of the all ceria-based samples. (From ref. [25] M. Cargnello, *et al. Science* **341**, 771–773 (2013).)

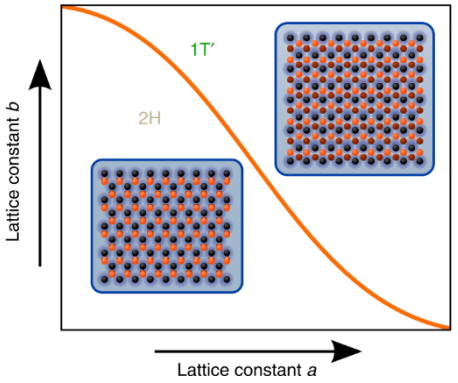

Figure 1.6. Substrate-based application of strain to a transition metal dichalcogenides monolayer with the chemical formula MX_2. One way in which the lattice parameters a and b of an MX_2 monolayer can be tuned is by an underlying substrate (shown as blue). (From ref. [27] K. A. N. Duerloo, Y. Li, E. J. Reed, *Nat. Commun.* **5** (2014).)

A wide range of heterostructured nanocrystals can be synthesized using solution-based approaches. Wet chemistry has been used as one of the most fundamental tools for the nucleation and growth of the shell material on the seed nanocrystals.[28-31] In the seed-mediated growth method, typically, the precursor of the overgrowth phase materials is added to the solution containing preformed nanocrystals. Using well-faceted nanocrystal seeds allowed the nucleation and growth of the secondary material in a controlled manner to produce shape-controlled core/shell nanocrystals (Figure 1.7).[32] If the synthetic conditions are well controlled, the sequential stepwise synthesis of high-order colloidal hybrid nanoparticles can be achieved (Figure 1.8).[33] This method enables the shell material to be nucleated and epitaxially grown on the nanocrystal seed substrate with a lattice mismatch.

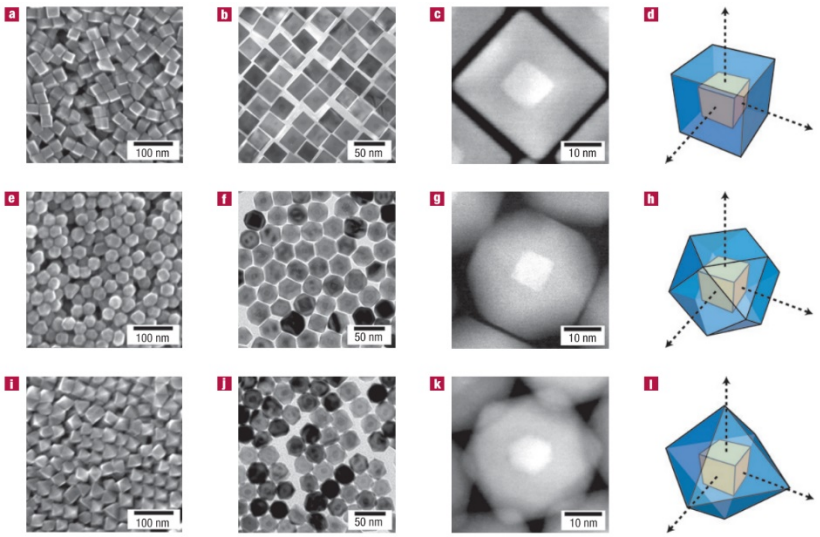

Figure 1.7. Shaped binary metal nanocrystals. (a-l), Cubic Pt seeds were used to direct the epitaxial overgrowth of Pd to form Pt/Pd core–shell cubes (a-d), cuboctahedra (e–h) and octahedra (i–l). Low magnification SEM images showing the overall morphology (a,e,i). The presence of a cubic Pt seed at the core of each particle is shown in TEM images (b,f,j). From the high resolution STEM images (c,g,k), the orientation of the cubic Pt seed within the Pd shell are revealed (d,h,l). (From ref. [32] S. E. Habas, H. Lee, V. Radmilovic, G. a Somorjai, P. Yang, *Nat. Mater.* **6**, 692–7 (2007).)

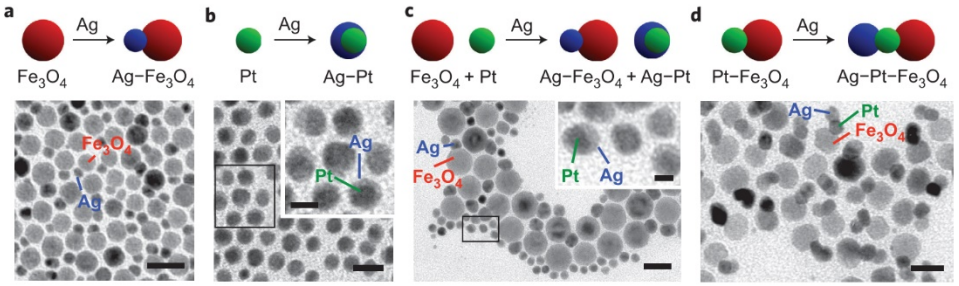

Figure 1.8. A series of experiments of heterogeneous nucleation in the prototype Ag–Pt–Fe_3O_4 system: Ag–Fe_3O_4 (a), Ag–Pt (b), mixture of Ag–Fe_3O_4 and Ag–Pt (c) and Ag–Pt–Fe_3O_4 (d) nanoparticles. The scale bars are 20 nm (main panels) and 5 nm (insets). (From ref. [33] M. R. Buck, J. F. Bondi, R. E. Schaak, *Nat. Chem.* **4**, 37–44 (2012).)

1.2.2 Strain in heterostructured nanocrystals

In a strained heterostructured nanocrystal, the strain can be induced by the difference in the bulk lattice parameters between the core and the shell material. The lattice strain (s) in the shell nanocrystal relative to core nanocrystal is given by the following equation, where a_{shell} and a_{core} are the bulk lattice parameters of the shell and the core, respectively.

$$s = ((a_{shell} - a_{core})/a_{core}) \times 100$$

As analogous to 2D SK growth mode, the overgrowth material (i.e., shell) grown on the substrate nanocrystal (i.e., core) can be divided into two phases—coherent layer and relaxed 3D island (Figure 1.9).[34] During the pseudomorphic growth, the strain can be imparted in the overgrowth phase at the interface by the lattice mismatch between the core and the shell. The epitaxially grown film undergoes the elastic or plastic deformation depending on the degree of the mismatch. If the mismatch is relatively small, the film grown on the substrate would be elastically deformed to the extent that it can recover its natural lattice parameters. For example, when Au (shell material) nucleates on the $CoPt_3$ core nanocrystal, the interface energy is increased by the lattice mismatch between the Au and the $CoPt_3$ (Figure 1.10). If the size of the $CoPt_3$ seed nanocrystals used does not exceed the misfit dislocation period

of $CoPt_3$/Au, a coherent layer with a strained lattice is formed, followed by 3D islands on top of the strained layer.

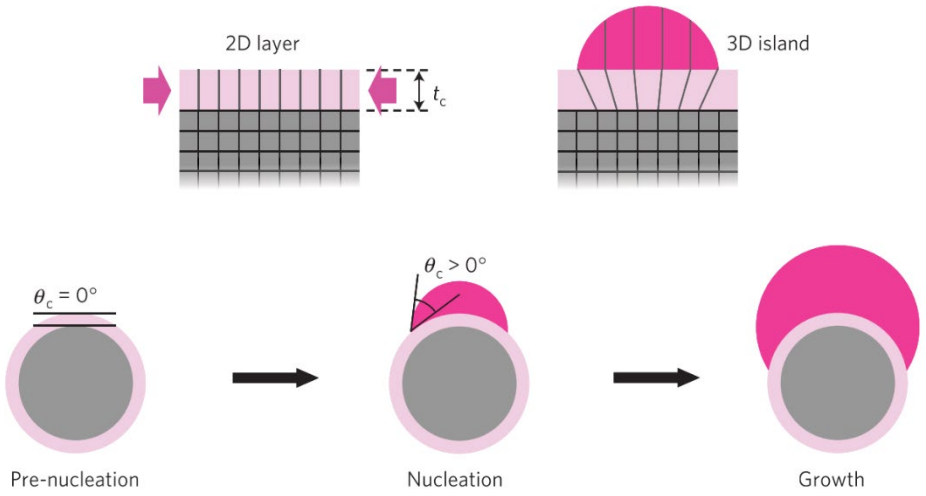

Figure 1.9. Illustration of 2D and 3D Stranski–Krastanov model. (Upper row) Lattice structure of the overgrowth phase in the 2D SK growth model. (Bottom row) Morphological evolution of the seed/Au heterostructure during the pre-nucleation, nucleation and growth periods. (From ref. [34] S. G. Kwon, *et al. Nat. Mater.* **14**, 215–223 (2014).)

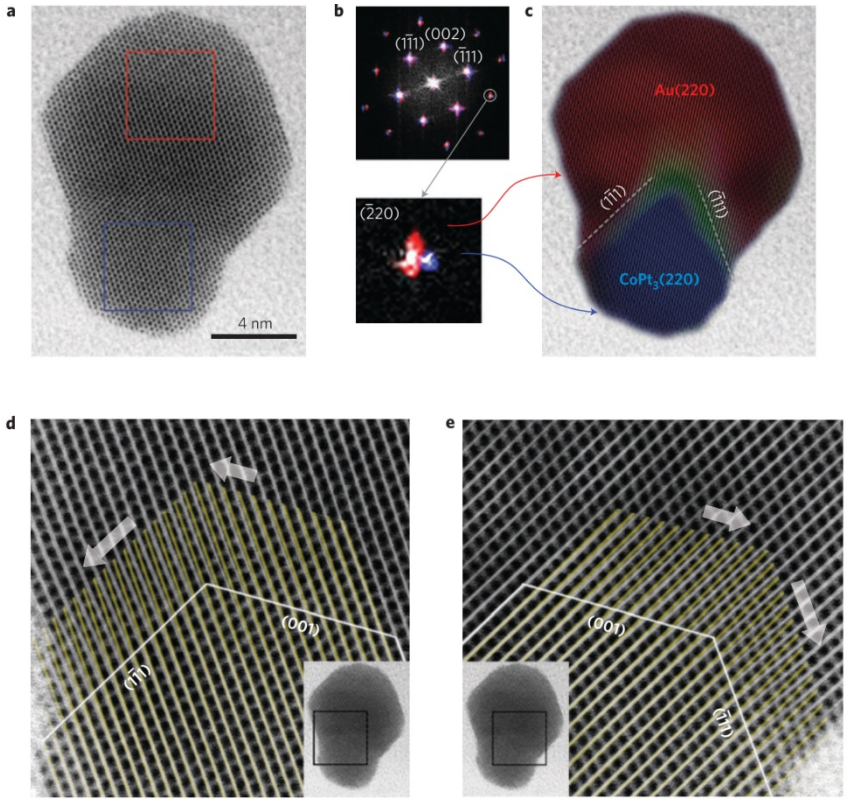

Figure 1.10. Study on the heteroepitaxial structure of $CoPt_3$/Au nanodumbbells. (a-c) Atomic-resolution annular bright-field STEM (a), FFT (b) and inverse FFT (c) images of the nanodumbbell. The seed (blue) and Au (red) domains in the (c) were obtained by inverse FFT of $CoPt_3$ and Au (220) spots in (b). (d,e) Magnified images of the area indicated in the insets. The direction of the displacement of the lattice planes (white) with respect to the seed lattice (yellow) is indicated with arrows. (From ref. [34] S. G. Kwon, *et al. Nat. Mater.* **14**, 215–223 (2014).)

Larger lattice mismatch leads to the larger interfacial strain that can be accommodated by the plastic deformation, such as misfit dislocations. As the elastic strain energy increases with the interface area of the core and the shell, there is a high possibility that misfit dislocations can be introduced at the interface when using a large core. In the case of heterostructured InAs/InSb nanowires, the misfit dislocations were formed at the interface between InAs and InSb when InAs core nanowires with a radius greater than 10 nm were used (Figure 1.11).[35] This result has been expected from the previous literature.[36] With the InAs nanowires of a radius of more than 10 nm, the formation of misfit dislocation at the InAs–InSb interface is energetically favorable to release the accumulated large strain energy.

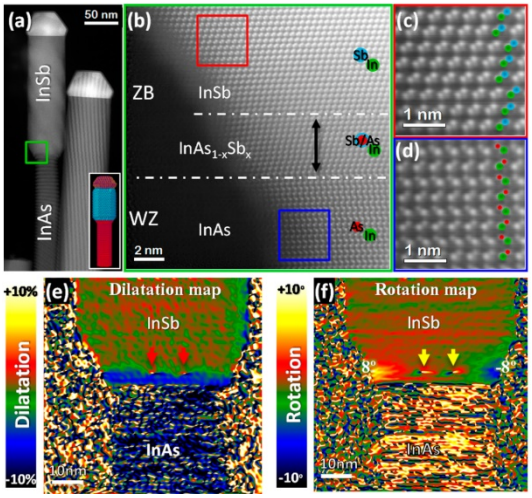

Figure 1.11. Formation of dislocations in heterostructured InAs/InSb nanowires. (a) HAADF image of InAs/InSb nanowires. (b) Atomic resolution image of the heterointerface, green square in (a). (c,d) Magnified detail of the InSb/InAs structure. (e-f) Dilatation (e) and rotation (f) map after applying GPA to the (−11−1) plane of the zinc blende region. Red and yellow arrows indicate the presence of misfit dislocations. (From ref. [35] M. De La Mata, C. Magén, P. Caroff, J. Arbiol, *Nano Lett.* **14**, 6614–6620 (2014).)

Anisotropy in a lattice mismatch of different crystallographic directions can be used to tune the morphology of the heterostructured nanocrystal. For example, the lattice parameter between $Cu_{1.8}S$ nanorod core and CdS shell is well matched to each other along *c* direction, whereas the lattice mismatch along *a*-axis differs substantially (Figure 1.12).[37] To minimize the interface energy, the Cd^{2+} tends to exchange the Cu^{+} along the *a* direction while forming the interface along the *c* direction. On the other hand, $Cu_{1.8}S$ and ZnS form an interface along the *a* direction to avoid a large lattice mismatch along the *c* direction.

The shell morphology can also be controlled by changing the reactivity of the secondary material precursor. Banin group reported the core/shell ZnSe/ZnS nanocrystals with different shell morphology from flat, island-like to helical shells (Figure 1.13).[38] At the initial stage of shell growth, the uniform ZnS shell grows as a wetting layer below the critical thickness. The ZnS shell grows further at the top of the wetting layer, leading to flat-, islands- and helical-shell morphologies. The growth behavior of the shell was controlled by the growth rate of the shell precursor, zinc oleate. By reducing the ratio of zinc to oleic acid, the reactivity of zinc precursor decreases, slowing down the growth rate. The reduced growth rate allows the shell growth to approach the thermodynamic limit and to achieve minimal total energy.

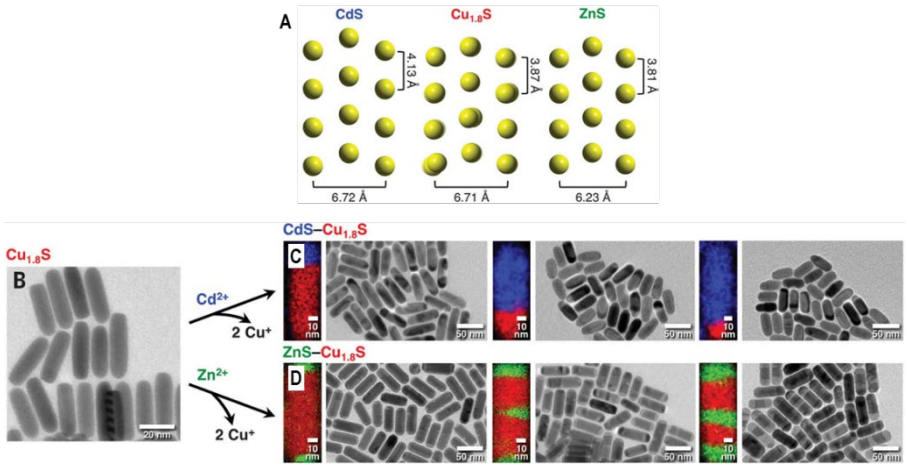

Figure 1.12. Formation of bimetallic nanostructures. (A) Crystal structure projections of wurtzite CdS, roxbyite $Cu_{1.8}S$, and wurtzite ZnS. (B) TEM image of $Cu_{1.8}S$ rods. (C,D) CdS–$Cu_{1.8}S$ capped rods (C) and ZnS–$Cu_{1.8}S$ striped rods (D) are produced though partial cation exchange with Cd^{2+} and Zn^{2+} using $Cu_{1.8}S$ rods. (From ref. [37] J. L. Fenton, B. C. Steimle, R. E. Schaak, *Science* **360**, 513–517 (2018).)

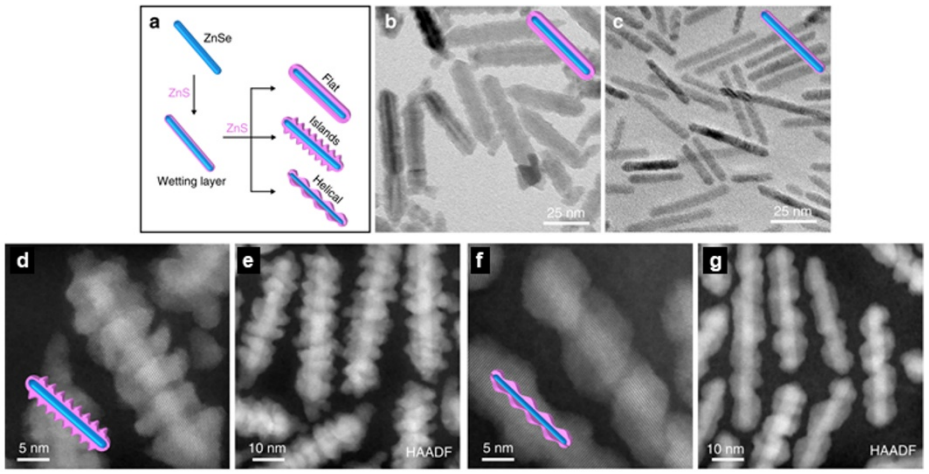

Figure 1.13. Control of shell morphologies of ZnSe/ZnS nanorods. (a) Schematic illustration of the control of shell growth of ZnS on a ZnSe nanorod. (b-g) TEM and STEM images of ZnSe/ZnS core/flat-shell (b), ZnSe/ZnS core/wetting layer (c), ZnSe/ZnS core/islands-shell (d,e), and ZnSe/ZnS core/helical-shell (f,g) nanorods. (From ref. [38] B. Ji, *et al. Nat. Commun.* **10**, 2 (2019).)

1.2.3 Characterization of strained nanocrystals for catalysis

It is well known that the epitaxial strain can efficiently modify the properties of functional materials.[39] The ability to control and manipulate the strain in epitaxial films is a key consideration for next-generation devices, such as optical, electronic, and magnetic devices.[40] To achieve such control, a fundamental understanding of the structural deformation and related physicochemical and mechanical properties is critical.

Although traditional thin-film epitaxy has been considered to be one of the most effective tools for producing high-quality heterostructured nanocrystalline materials, the defects generated within the heteronanostructures have recently attracted considerable interest in enhancing the material properties.[41] Strain engineering allows electronic structure modification of the defects, generating highly active defect sites.[42] It is therefore important to understand the effect of the deformed structure of heterostructured nanocrystals on catalytic performance in the design of the catalysts with better catalytic activity. However, the lack of uniformity in the deformed structure makes it difficult to understand the relationship between the structure and the catalytic properties. As the result of the catalytic activity measurements is the average of the ensemble properties of heterogeneous nanocrystals with non-uniform defects, the production of uniform nanocrystals is essential. The uniformity of seed nanocrystals and the precisely controlled

synthetic parameters of seed-mediated growth, such as ligand and pH of the solution, can increase the possibility of achieving uniform heterostructured nanocrystals. The resulting uniform nanocrystals with distinct defects are then used to investigate the structure–property relationship. Elucidating the defect structure requires atomic-resolution imaging using (scanning) transmission electron microscopy ((S)TEM) because the deformation is hard to capture without going down to the atomic level. The high precision strain distribution in the nanocrystals can be mapped by computer-vision based analysis, in combination with atomic-scale imaging.

The effect of strained lattices in nanomaterials on enhanced catalytic activity for electrochemical oxygen reduction has been intensively studied over the last decades.[43] The surface strain in the Pt-based core/shell multimetallic nanocrystals is often induced by the lattice mismatch between the core and the shell materials and can be tuned by different lattice constants of Pt-M alloyed core. For example, the control of atomic composition in the alloy core/shell nanoparticle system has been studied for the tuning of electrocatalytic activity. By changing the composition of the Cu precursor, the lattice parameter of the shell in Pt–Cu bimetallic nanoparticle is changed, resulting in the tuning of the shell strain (Figure 1.14).[44] Another important approach to controlling the strain can be the use of the different crystal structures of the core. Different crystal phases, such as the face-centered cubic

structure and the face-centered tetragonal structure, have different lattice parameters and tune the strain by causing a different degree of lattice distortion in the shell.[45]

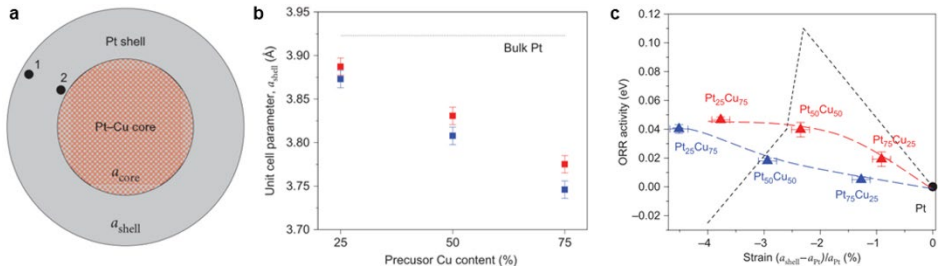

Figure 1.14. Relationship between lattice strain and oxygen reduction reaction activity. (a) Scheme of a simple two-phase model of a core/shell Pt–Cu/Pt particle. (b) Plot showing unit cell parameter, a_{shell}, as a function of the alloy precursor Cu atomic composition. (c) Experimental and predicted relationships between lattice strain and oxygen reduction reaction activity. (From ref. [44] Strasser, P. *et al.*, *Nat. Chem.* **2**, 454–460 (2010).)

The ability to produce a well-defined structure of the core nanocrystal enabled the study of the facet-dependent surface strains. The epitaxial shell on the a well-faceted core nanocrystal can give rise to biaxially[46] or highly[47] strained heterostructured nanocrystals. In the heterostructured PtPb/Pt system, the crystal structures for PtPb and Pt are hexagonal and cubic phase, respectively, with different stacking sequences. Therefore, two types of interfacial planes can be formed between the PtPb nanoplates core and the Pt shell, resulting in a biaxially strained Pt layer. The increase in the activity for oxygen reduction reactions of core/shell PtPb/Pt nanoplate was attributed to the tensile strain on Pt {110} facets induced by the lattice mismatch with PtPb {001} plane (Figure 1.15). Similarly, as the lattice mismatch between the PdCu B2 intermetallic core and the Pt–Cu alloy shell varies from facet to facet, the surface strain of the shell also varies. For example, the mismatch obtained from the bulk lattice parameter between PdCu B2 {110} and Pt−Cu {111} planes is much smaller (~4.7%) than between PdCu B2 {100} and Pt−Cu {110} planes (~8.7%) (Figure 1.16).

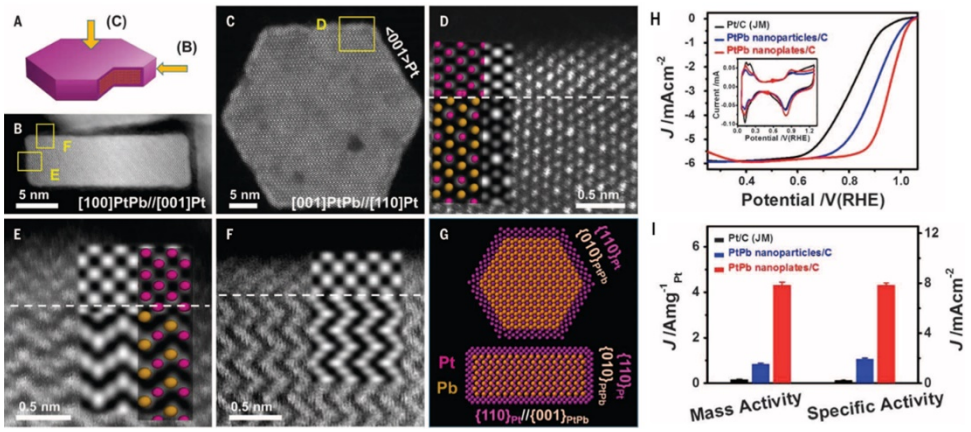

Figure 1.15. Structure analysis and electrocatalytic performance of core/shell PtPb/Pt nanoplates. (A) A model of a hexagonal nanoplate (B,C) STEM images from in-plate view (B) and out-of-plate view (C). (D-F) High-resolution STEM images from the selected area in (C). (G) The schematic atom models of the nanoplate showing the top interface [(110)Pt//(100)PtPb] and the side interface [(110)Pt//(001)PtPb]. (H-I) ORR polarization curves (H) and specific and mass activities (I) of different catalysts. (From ref. [46] L. Bu, *et al. Science* **354**, 1410–1414 (2016).)

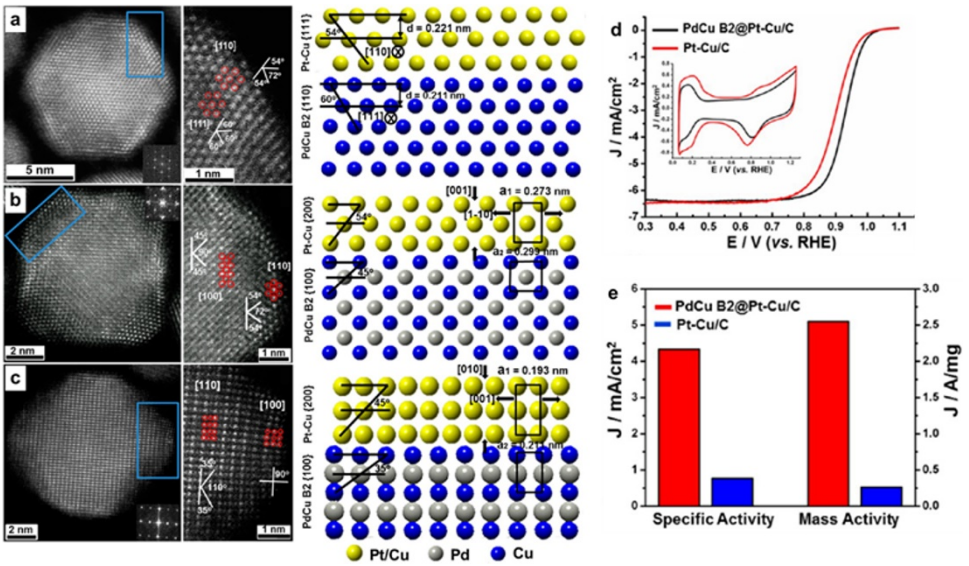

Figure 1.16. Structure analysis and electrocatalytic performance of core/shell PdCu B2/Pt−Cu nanoparticles. (a-c) STEM images and 2D atomic models of core/shell PdCu B2/Pt−Cu nanoparticle along PdCu B2 [111] (a), [100] (b), and [110] (c) zone axes. (d) ORR polarization curves with an inset of CVs. (e) Specific and mass activities of each catalyst. (From ref. [47] C. Wang, *et al. Nano Lett.* **17**, 5526–5532 (2017).)

1.3 Dissertation Overview

The main focus of this thesis is strained oxide nanomaterial science. This thesis encompasses aspects of the design, synthesis, and characterization of strained oxide nanocrystals, as well as their application to the electrocatalysis and radioprotectants. The ability to synthesize well-defined defects within the nanocrystals has enabled us to observe and reveal the strained structure with high precision and to correlate the structure and the catalytic properties. Chapter 1 presents the introduction of the method of thin-film epitaxy and growth mode, as well as epitaxial strains in nanomaterials.

In Chapter 2, I present the design and synthesis of multigrain oxide nanocrystals with controllable grain boundary defects via geometric misfit strain. The precise control of the colloidal polyhedral nanocrystal heteroepitaxy enables us to grow grains ordered in a high three-dimensional symmetry and to produce uniform GB defects. The multigrain nanocrystals consisting of Co_3O_4 nanocube cores and Mn_3O_4 shells are separated into mutually orthogonal multiple grains. At the sharp edges of the Co_3O_4 nanocubes, tilt boundaries of the Mn_3O_4 grains exist in the form of disclinations due to a large geometric misfit between adjacent tetragonal Mn_3O_4 grains. Four design principles to produce the highly ordered multigrain nanostructures with GBs were identified. Using these principles, we produced

a wide range of multigrain nanocrystals containing GBs with various material combinations including Co_3O_4/Mn_3O_4, Fe_3O_4/Mn_3O_4, Fe_3O_4/Co_3O_4, Mn_3O_4/Co_3O_4, and Pd/Au. Computer vision-based image processing combined with atomic imaging of the nanocrystals using high-angle annular dark-field scanning transmission electron microscopy (HAADF-STEM) made it possible to study the atomic scale (with a precision of $\sim 10^{-2}$ nm) structure of the GB defects.

In Chapter 3, I present epitaxially strained CeO_2/Mn_3O_4 nanocrystals as an enhanced antioxidant for radioprotection. Nanomaterials with antioxidant properties are of interest as candidate materials for treating reactive oxygen species (ROS)-related diseases. However, it is important for clinical applications to maintain efficacy while using low doses to minimize toxicity. The heterostructured CeO_2/Mn_3O_4 nanocrystals are synthesized using seed-mediated growth. The nanocrystals with surface strains serve as highly catalytic antioxidants that can protect tissue-resident stem cells from irradiation-induced ROS damage. When manganese ions are deposited on the surface of CeO_2 nanocrystals, strained layers of Mn_3O_4 islands are formed, increasing the number of oxygen vacancies. The CeO_2/Mn_3O_4 nanocrystals show better electrocatalytic activity for hydrogen peroxide and oxygen reduction reactions than CeO_2 or Mn_3O_4 alone. With enhanced catalytic activity, the nanocrystals can protect the regenerative capabilities of intestinal

stem cells in an organoid model after irradiation with a lethal dose. A small amount of nanocrystals prevents acute radiation syndrome and increases the survival rate of mice treated with lethal doses of total body irradiation.

1.4 References

[1] L. W. Martin, Y. H. Chu, R. Ramesh, Advances in the growth and characterization of magnetic, ferroelectric, and multiferroic oxide thin films. *Mater. Sci. Eng. R Reports* **68**, 89–133 (2010).

[2] C. Tan, J. Chen, X. J. Wu, H. Zhang, Epitaxial growth of hybrid nanostructures. *Nat. Rev. Mater.* **3**, 1–13 (2018).

[3] S. Park, C. H. Kim, W. J. Lee, S. Sung, M. H. Yoon, Sol-gel metal oxide dielectrics for all-solution-processed electronics. *Mater. Sci. Eng. R Reports* **114**, 1–22 (2017).

[4] I.V. Markov, Crystal Growth for Beginners: Fundamentals of Nucleation, Crystal Growth, and Epitaxy, World Scientific, Singapore, 2003.

[5] L. Carbone, P. D. Cozzoli, Colloidal heterostructured nanocrystals: Synthesis and growth mechanisms. *Nano Today* **5**, 449–493 (2010).

[6] Z. Zhang, M. G. Lagally, Atomistic processes in the early stages of thin-film growth. *Science* **276**, 377–383 (1997).

[7] M. Valden, X. Lai, D. W. Goodman, Onset of catalytic activity of gold clusters on titania with the appearance of nonmetallic properties. *Science* **281**, 1647–1650 (1998).

[8] O. E. Shklyaev, M. J. Beck, M. Asta, M. J. Miksis, P. W. Voorhees, Role of strain-dependent surface energies in Ge/Si(100) island formation. *Phys. Rev. Lett.* **94**, 176102 (2005).

[9] J. Tersoff, F. K. Legoues, Competing relaxation mechanisms in strained layers. *Phys. Rev. Lett.* **72**, 3570–3573 (1994).

[10] D. J. Eaglesham, M. Cerullo, Dislocation-free Stranski-Krastanow growth of Ge on Si(100). *Phys. Rev. Lett.* **64**, 1943–1946 (1990).

[11] J. Tersoff, R. M. Tromp, Shape transition in growth of strained islands: Spontaneous formation of quantum wires. *Phys. Rev. Lett.* **70**, 2782–2785 (1993).

[12] F. M. Ross, R. M. Tromp, M. C. Reuter, Transition states between pyramids and domes during Ge/Si island growth. *Science* **286**, 1931–1934 (1999).

[13] F. Liu, F. Wu, M. G. Lagally, Effect of Strain on Structure and Morphology of Ultrathin Ge Films on Si(001). *Chem. Rev.* **97**, 1045–1062 (1997).

[14] H. Hu, H. J. Gao, F. Liu, Theory of directed nucleation of strained islands on patterned substrates. *Phys. Rev. Lett.* **101,** 2–5 (2008).

[15] P. Liu, C. Lu, Y. W. Zhang, Formation of surface structures during heteroepitaxial thin film growth on prepatterned substrates. *Phys. Rev. B - Condens. Matter Mater. Phys.* **76,** 1–5 (2007).

[16] G. Chen, *et al.* Formation of Ge nanoripples on vicinal si (1110): From Stranski-Krastanow seeds to a perfectly faceted wetting layer. *Phys. Rev. Lett.* **108,** 1–5 (2012).

[17] S. Y. Shiryaev, F. Jensen, J. L. Hansen, J. W. Petersen, A. N. Larsen, Nanoscale Structuring by Misfit Dislocations in Si1-xGex/Si Epitaxial Systems. *Phys. Rev. Lett.* **78**, 503–506 (1997).

[18] H. Brune, M. Giovannini, K. Bromann, K. Kern, Self-organized growth of nanostructure arrays on strain-relief patterns. *Nature* **394**, 451–453 (1998).

[19] B. Yang, F. Liu, M. G. Lagally, Local Strain-Mediated Chemical Potential Control of Quantum Dot Self-Organization in Heteroepitaxy. *Phys. Rev. Lett.* **92**, 025502 (2004).

[20] B. C. Steimle, J. L. Fenton, R. E. Schaak, Rational construction of a scalable heterostructured nanorod megalibrary. *Science* **367**, 418–424 (2020).

[21] P.-C. Chen, *et al.* Interface and heterostructure design in polyelemental nanoparticles. *Science* **363**, 959–964 (2019).

[22] X. Peng, M. C. Schlamp, A. V. Kadavanich, A. P. Alivisatos, Epitaxial growth of highly luminescent CdSe/CdS core/shell nanocrystals with photostability and electronic accessibility. *J. Am. Chem. Soc.* **119**, 7019–7029 (1997).

[23] U. Banin, Y. Ben-Shahar, K. Vinokurov, Hybrid Semiconductor–Metal Nanoparticles: From Architecture to Function. *Chem. Mater.* **26**, 97–110 (2014).

[24] Z. C. Zhang, B. Xu, X. Wang, Engineering nanointerfaces for nanocatalysis. *Chem. Soc. Rev.* **43**, 7870–7886 (2014).

[25] M. Cargnello, *et al.* Control of Metal Nanocrystal Size Reveals Metal-Support Interface Role for Ceria Catalysts. *Science* **341**, 771–773 (2013).

[26] Z. Dai, L. Liu, Z. Zhang, Strain Engineering of 2D Materials: Issues and Opportunities at the Interface. *Adv. Mater.* **31**, 1–11 (2019).

[27] K. A. N. Duerloo, Y. Li, E. J. Reed, Structural phase transitions in two-dimensional Mo-and W-dichalcogenide monolayers. *Nat. Commun.* **5** (2014).

[28] C. de Mello Donegá, Synthesis and properties of colloidal heteronanocrystals. *Chem. Soc. Rev.* **40**, 1512–1546 (2011).

[29] J. M. Hodges, *et al.* Insights into the seeded-growth synthesis of colloidal hybrid nanoparticles. *Chem. Mater.* **29**, 106–119 (2017).

[30] J. Lee, J. Yang, S. G. Kwon, T. Hyeon, Nonclassical nucleation and growth of inorganic nanoparticles. *Nat. Rev. Mater.* **1**, 16034 (2016).

[31] M. H. Oh, *et al.* Galvanic Replacement Reactions in Metal Oxide Nanocrystals. *Science* **340**, 964–968 (2013).

[32] S. E. Habas, H. Lee, V. Radmilovic, G. A. Somorjai, P. Yang, Shaping binary metal nanocrystals through epitaxial seeded growth. *Nat. Mater.* **6**, 692–7 (2007).

[33] M. R. Buck, J. F. Bondi, R. E. Schaak, A total-synthesis framework for the construction of high-order colloidal hybrid nanoparticles. *Nat. Chem.* **4**, 37–44 (2012).

[34] S. G. Kwon, *et al.* Heterogeneous nucleation and shape transformation of multicomponent metallic nanostructures. *Nat. Mater.* **14**, 215–223 (2014).

[35] M. De La Mata, C. Magén, P. Caroff, J. Arbiol, Atomic scale strain relaxation in axial semiconductor III-V nanowire heterostructures. *Nano Lett.* **14**, 6614–6620 (2014).

[36] K. L. Kavanagh, Misfit dislocations in nanowire heterostructures. *Semicond. Sci. Technol.* **25** (2010), doi:10.1088/0268-1242/25/2/024006.

[37] J. L. Fenton, B. C. Steimle, R. E. Schaak, Tunable intraparticle frameworks for creating complex heterostructured nanoparticle libraries. *Science* **360**, 513–517 (2018).

[38] B. Ji, *et al.* Strain-controlled shell morphology on quantum rods. *Nat. Commun.* **10**, 2 (2019).

[39] M. Luo, S. Guo, Strain-controlled electrocatalysis on multimetallic nanomaterials. *Nat. Rev. Mater.* **2**, 17059 (2017).

[40] A. M. Smith, A. M. Mohs, S. Nie, Tuning the optical and electronic properties of colloidal nanocrystals by lattice strain. *Nat. Nanotechnol.* **4**, 56–63 (2009).

[41] W. Li, *et al.* Defect Engineering for Fuel-Cell Electrocatalysts. *Adv. Mater.* **1907879**, 1–20 (2020).

[42] J. M. Rondinelli, N. A. Spaldin, Structure and Properties of Functional Oxide Thin Films: Insights From Electronic-Structure Calculations. *Adv. Mater.* **23**, 3363–3381 (2011).

[43] M. Mavrikakis, B. Hammer, J. K. Nørskov, Effect of strain on the reactivity of metal surfaces. *Phys. Rev. Lett.* **81**, 2819–2822 (1998).

[44] Strasser, P. *et al.*, Lattice-strain control of the activity in dealloyed core-shell fuel cell catalysts. *Nat. Chem.* **2**, 454–460 (2010).

[45] S. Zhang, *et al.* Tuning Nanoparticle Structure and Surface Strain for Catalysis Optimization. *J. Am. Chem. Soc.* **136**, 7734–7739 (2014).

[46] L. Bu, *et al.* Biaxially strained PtPb/Pt core/shell nanoplate boosts oxygen reduction catalysis. *Science* **354**, 1410–1414 (2016).

[47] C. Wang, *et al.* Facet-Dependent Deposition of Highly Strained Alloyed Shells on Intermetallic Nanoparticles for Enhanced Electrocatalysis. *Nano Lett.* **17**, 5526–5532 (2017).

Chapter 2 Design and Synthesis of Multigrain Nanocrystals via Geometric Misfit Strain

2.1 Introduction

Topological defects associated with grain boundaries (GB defects) have significant effects on the electrical, optical, magnetic, mechanical, and chemical properties of nanocrystalline materials[1,2]. However, elucidating the contribution of specific GB defects to such properties has been a challenging task due to the non-uniformity in grain size and shape, and the random misorientation between the grains[3-5]. Here, we demonstrate that precise control of the heteroepitaxy of colloidal polyhedral nanocrystals enables highly ordered grain growth with defined three-dimensional (3D) symmetry and the production of uniform GB defects, providing an unprecedented opportunity to overcome the limitations of prior sample preparation methods. We synthesized a prototypical multigrain nanocrystal consisting of a Co_3O_4 nanocube core with each facet of the core attached to a Mn_3O_4 shell. The individual shells are symmetry-related interconnected grains[6]. At the sharp edges of the Co_3O_4 nanocubes, the tilt boundaries of these Mn_3O_4 grains join *via* disclinations due to the large geometric misfit between the adjacent tetragonal Mn_3O_4 grains. We set four design principles to produce such highly ordered multigrain nanostructures *via* the geometric misfit strain. First, the

shape of the substrate nanocrystal guides the crystallographic orientation of the overgrowth phase[7]. Second, the size of the substrate must be smaller than the characteristic distance between the dislocations. Third, the incompatible symmetry between the overgrowth phase and the substrate increases the geometric misfit between the grains. Finally, under near-equilibrium conditions for the GB formation, the surface energy of the shell is balanced by the increasing elastic energy through ligand passivation[8-10]. Based on these principles, we produced various combinations of multigrain nanocrystals containing distinct GB defects.

2.2 Experimental Section

2.2.1 Synthesis of nanocrystals

Co_3O_4 nanocubes. A mixture of 0.37 g of cobalt(II) perchlorate (Aldrich) and 2.7 g of oleylamine (Acros) in 15 mL of 1-octanol (Aldrich) was heated to 120 °C under air and aged for 2 hr. During the heating, 0.7 mL of distilled water was added before the temperature reaches 120 °C. After the reaction, an excess amount of acetone and ethanol was added and Co_3O_4 nanocubes were retrieved by centrifugation.

CoMn-CL. An organic/aqueous suspension was prepared by adding a mixture of oleylamine (5 mmol), oleic acid (0.5 mmol), and hydrochloric acid (3.15 mmol, Aldrich) to 15 mL of *o*-xylene (Aldrich) containing 0.080 g of Co_3O_4 nanocubes. The as-prepared suspension was heated to 60 °C under air and aged for one hour with magnetic stirring. And then, 4 mL of 0.5 M aqueous solution of manganese(II) formate was rapidly injected into the suspension at 90 °C and aged for 1.5 h under air. After the reaction, the nanocrystals were washed with ethanol and retrieved by centrifugation. As-prepared heterostructured Co_3O_4/Mn_3O_4 nanocrystals are well dispersible in non-polar solvents including hexane, toluene, xylene, and tetrahydrofuran (THF).

CoMn-CL+I. Synthetic procedure is the same as that for CoMn-CL except that manganese(II) chloride (Aldrich) (0.8 mL of 2.5 M) and xylenes (Aldrich) were used instead of manganese(II) formate and *o*-xylene.

CoMn-no GB. Synthetic procedure is the same as that for CoMn-CL except that manganese(II) chloride (0.8 mL of 2.5 M), xylenes, and hydrochloric acid (4.5 mmol) were used instead of manganese(II) formate, *o*-xylene, and hydrochloric acid (3.15 mmol).

Co_3O_4/Mn_3O_4 core/shallow shell nanocrystals. Synthetic procedure is the same as that for CoMn-no GB except that the amount of oleylamine was reduced to 4 mmol.

Co_3O_4/Mn_3O_4 nanocrystals with closed looped six grains. The synthetic procedure of CoMn-no GB sample was repeated for several times with as-synthesized nanocrystals from each step. The synthetic procedure of CoMn-CL sample with modified reaction solution (3.15 mmol of formic acid was used instead of hydrochloric acid) was repeated for several times. With > 30 nm-sized Co_3O_4 nanocube, the synthetic procedure of CoMn-CL sample was repeated for several times.

Co_3O_4/Mn_3O_4 nanocrystals with dislocations. The synthetic procedure of CoMn-CL sample was repeated for three times, and then the nanocrystals were dispersed in the mixture of oleylamine (5 mmol), oleic acid (0.5 mmol), nitric

acid (3.15 mmol), and xylenes. The as-prepared suspension was heated to 130 °C under air and aged with magnetic stirring. And then, 0.8 mL of 1.25 M aqueous solution of manganese(II) nitrate (Aldrich) was rapidly injected into the suspension at 90 °C and aged at 130 °C for 1.5 h under air. After the reaction, the nanocrystals were washed and retrieved by the same method used for the CoMn-CL sample. Then, the synthetic procedure of CoMn-CL sample was applied once to the nanocrystals to obtain the final product.

Fe_3O_4 nanocrystals. The nanocrystals were synthesized *via* a thermal decomposition method with a typical Schlenk line technique[11]. Mixture of iron(III) acetylacetonate (15.892 g, Acros), oleic acid (33.9 g), and benzyl ether (312 g, Aldrich) was heated to 290 °C at a rate of 20 °C/min and then annealed at that temperature for 30 min while being vigorously stirred. After the reaction, the solution was rapidly cooled to room temperature and washed with 200 ml of toluene and 500 ml of ethyl alcohol.

Fe_3O_4/Mn_3O_4 core/shell nanocrystals. An organic/aqueous suspension was prepared by adding a mixture of oleylamine (5 mmol), oleic acid (0.5 mmol), and nitric acid (3.15 mmol) to 15 mL of xylenes containing 0.078 g of Fe_3O_4 nanocrystals. Synthetic procedure is the same as that for CoMn-CL+I except that manganese(II) nitrate (0.8 mL of 2.5 M) as manganese precursor, 120 °C as aging temperature, and 2 h as aging time were used.

Mn_3O_4 nanocrystals. Synthetic procedure is the same as that described in the ref. 12.

Mn_3O_4(or Fe_3O_4)/Co_3O_4 core/shell nanocrystals. An organic/aqueous suspension was prepared by adding a mixture of oleylamine (5 mmol), oleic acid (0.5 mmol), and acetic acid (3.15 mmol) to 15 mL of xylenes containing 0.076 g of Mn_3O_4 nanocrystals (or 0.078 g of Fe_3O_4 nanocrystals) and 1.0 mmol of cobalt(II) acetate. The as-prepared suspension was heated to 60 °C under air and aged with magnetic stirring. After that, 0.8 mL of distilled water was rapidly injected into the suspension at 90 °C and aged for 1.5 h under air. After the reaction, the nanocrystals were washed and retrieved by the same method used for the CoMn-CL sample.

Pd nanocubes[13]. An aqueous solution containing poly(vinyl pyrrolidone) (PVP, MW=55,000, 105 mg), L-ascorbic acid (60 mg), KBr (400 mg, Fisher), and 8 mL of distilled water was heated at 80 °C for half an hour. After that, 3 mL of distilled water and Na_2PdCl_4 (57 mg, Aldrich) was injected to the solution and heated at 80 °C for 3 h in the air under magnetic stirring. After the reaction, the solution was cooled down to room temperature, and the nanocrystals were washed with distilled water and retrieved by centrifugation.

Pd/Au core/shell nanocrystals[13]. As-synthesized Pd nanocubes were redispersed in 0.5 mL of distilled water, and the solution was added to 5 mL

of an aqueous solution containing PVP (5 mg) and L-ascorbic acid (3 mg). The solution was heated to 95 °C for 20 min. After that, the aqueous solution of 1.33 mmol of $HAuCl_4$ dissolved in 2 mL of distilled water was injected to the reaction solution. The reaction solution was heated at 95 °C and aged for 15 min. After the reaction, the nanocrystals were washed with distilled water. The reaction was repeated twice with as-synthesized nanocrystals from each step.

2.2.2 Structural and chemical analysis

The transmission electron microscopy (TEM) images were obtained using a JEOL JEM-2100F transmission electron microscope operated at 200 kV. The energy-filtered TEM (EFTEM) images were recorded with a JEOL JEM-2100F. High-angle annular dark-field scanning TEM (HAADF-STEM) images and electron energy-loss spectroscopy (EELS) analysis were obtained by using JEM-ARM200F operated at 200 kV (Cold Field Emission Type, JEOL) in National Center for Inter-university Research Facilities, Seoul National University. JEM-ARM200F microscope is equipped with 965 GIF Quantum ER (GATAN) EELS detector. Energy windows used for Mn L-edge map and Co L-edge map are 638–664 eV and 776.2–804.2 eV, respectively. Background is subtracted by the window of ~620 eV (width ~18 eV) for Mn and 750 eV (width ~25 eV) for Co. For HAADF-STEM imaging and EELS spectra, we adopted a convergence semi-angle and inner detect collection

angle of 19 mrad and 40 mrad, respectively. The acquisition time per pixel for EELS spectra was 0.5 s. Pixel time used to acquire HAADF-STEM image was 31.7 μs. Elemental analysis was performed *via* inductively coupled plasma-atomic emission spectroscopy (ICP-AES) (Shimadzu). X-ray diffraction patterns were obtained using a Rigaku D/max 2500 diffractometer equipped with a rotating anode and a Cu Kα radiation source (λ=0.15418 nm). XAFS Experiments were carried out at BL10C beamline in PLS-II and supported in part by MSIP and POSTECH. The Mn 3s X-ray photoelectron spectroscopy (XPS) measurements were carried out at Busan Center, Korea Basic Science Institute by using K-alpha (Thermo Scientific Inc.) with monochromatic Al Kα as an excitation source.

2.3 Result and Discussion

2.3.1 Synthesis and characterization of Co_3O_4 and Co_3O_4/Mn_3O_4 nanocrystals.

The geometric misfit strain in core/shell nanocrystals was investigated using nanocrystals of polyhedral Co_3O_4 core and heteroepitaxial Mn_3O_4 shell as a model system. We prepared ~11-nm-sized Co_3O_4 nanocubes with {100} facets as a substrate for the growth of Mn_3O_4 (Figure 2.1). The formation of Mn_3O_4 grains on the nanocube was carried out by the reaction of $MnCl_2$ or $Mn(HCOO)_2$ in an organic/aqueous (xylene/water) reverse micelle solution in the presence of oleylamine, oleic acid, and HCl[12,14]. X-ray diffraction (XRD) data confirmed that tetragonal Mn_3O_4 (a=b = 5.765 Å, c=9.442 Å, JCPDS #80-0382) was the deposited phase (Figure 2.2). It has a spinel structure elongated along the c-axis due to the Jahn–Teller (J–T) effect of Mn^{3+} with an electron configuration of $t_{2g}^3e_g^1$, whereas the Co_3O_4 core has a cubic spinel structure (a=b=c=8.084 Å, JCPDS #42-1467). As shown in Figure 2.3, the lattice of Mn_3O_4 {220} coincides with Co_3O_4 {400} at a misfit of less than 1%, explaining the consistent values in the in-plane interatomic distance (d_{in}) for both phases (see section 2.3.7 for more details on the Co_3O_4–Mn_3O_4 interface).

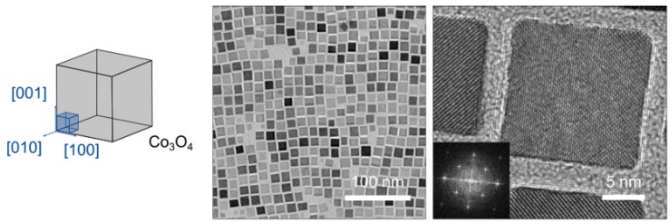

Figure 2.1. Low- and high-magnification TEM images of the ~11 nm-sized Co_3O_4 nanocube cores.

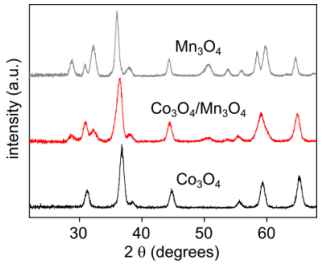

Figure 2.2. XRD patterns of Co_3O_4, Mn_3O_4, and Co_3O_4/Mn_3O_4 nanocrystals.

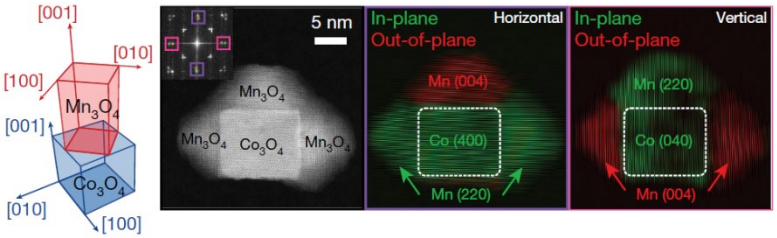

Figure 2.3. Illustration of the orientation relationship between Mn_3O_4 and Co_3O_4 unit cells. HAADF-STEM image and corresponding FFT of the Co_3O_4/Mn_3O_4 nanocrystal taken along the Co_3O_4 <100> and Mn_3O_4 <110> zone axes that shows the orientation relationship between the Co_3O_4 core and Mn_3O_4 grains. The in-plane (outer) spots in the FFT pattern are mapped in green (2.04 Å) and the out-of-plane (inner) spots are mapped in red (2.36 Å).

2.3.2 Epitaxially guided growth and gap closing of Mn_3O_4 grains on a Co_3O_4 nanocube

In Figure 2.3, the high-resolution high-angle annular dark-field scanning transmission electron microscope (HAADF-STEM) images and the Fourier-filtered images reveal that for each facet of the cubic core, a Mn_3O_4 grain grows in <001> directions perpendicular to Co_3O_4 {100}, and Mn_3O_4 {110} are parallel to Co_3O_4 {010}. The growth direction of the shell is guided by the lattice matching along six {100} surface planes of the Co_3O_4 core, which leads to the segmentation of the shell into multigrain (Figure 2.4). An irregularly shaped core induces an inconsistent lattice coincidence, which prevents the formation of an ordered grain structure (Figure 2.5)[15].

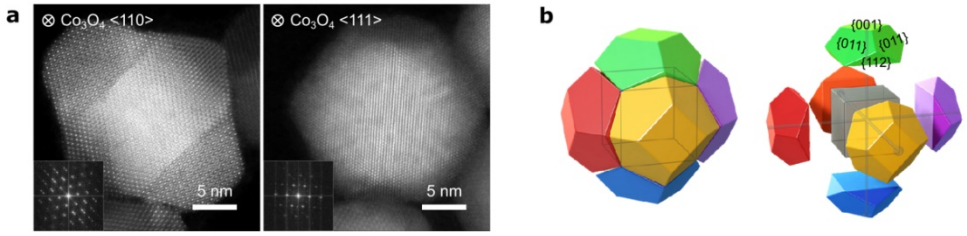

Figure 2.4. Morphology and grain geometry of Co_3O_4/Mn_3O_4 nanocrystal. **a**, High-resolution HAADF-STEM images taken along Co_3O_4 <110> and <111> zone axes showing the overall morphology of Co_3O_4/Mn_3O_4 nanocrystals. **b**, 3D model of the Co_3O_4/Mn_3O_4 nanocrystals.

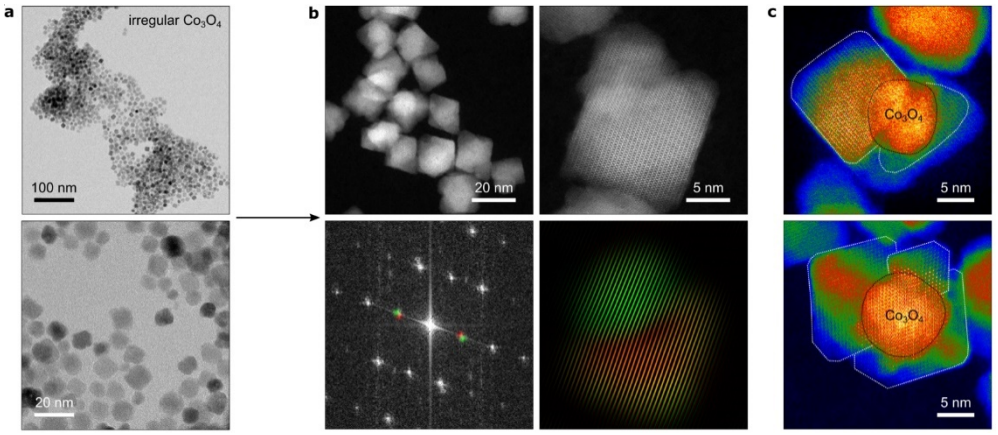

Figure 2.5. Effect of the shape of the core on the grain boundary structure of the shell and lattice distortions of Mn_3O_4 grains near the edges of a Co_3O_4 nanocube. **a-c**, Cores with irregular shapes cannot effectively guide the growth direction of the grains. TEM images of the irregular-shaped Co_3O_4 cores (**a**). Low- and high-magnification HAADF-STEM images, and FFT images of the Co_3O_4/Mn_3O_4 nanocrystals made from the irregular-shaped Co_3O_4 cores (**b**). The overall morphology of Co_3O_4/Mn_3O_4 is a truncated octahedron. However, growth directions of neighboring grains are not all orthogonal. Grains on more than two neighboring facets of Co_3O_4 are grouped into one growth direction (**b**, red-coloured regions). The intensities of TEM images are coloured from red (high intensity) to blue (low intensity) (**c**). The coloured intensity clearly shows the unpredictable growth directions of unguided Mn_3O_4 grains and their octahedron shape.

The tetragonal symmetry of Mn_3O_4 produces a gap with an angle of ~8.4° between the {112} planes of adjacent Mn_3O_4 grains along the edges of the Co_3O_4 core[16] (Figure 2.6). Twinned disclinations of Mn_3O_4 {112} with respect to Co_3O_4 {110} are thus formed around the boundary to close the gap. Accordingly, the fast Fourier transform (FFT) of the TEM image with the zone axis along Co_3O_4 [100] shows the extension of the square lattice of Co_3O_4 into Mn_3O_4 (Figure 2.7). A similar FFT analysis with the zone axis along Co_3O_4 [110] further supports the distortion of the Mn_3O_4 lattice structure near the Co_3O_4 nanocube edges (Figure 2.8). Each Mn_3O_4 grain has a truncated square pyramidal shape enclosed by {100} and {011} facets (Figure 2.4). The overall morphology of each Co_3O_4/Mn_3O_4 multigrain nanocrystal can be described as a truncated octahedron consisting of a cubic Co_3O_4 core and Mn_3O_4 grains orthogonally grown from the basal planes of the core.

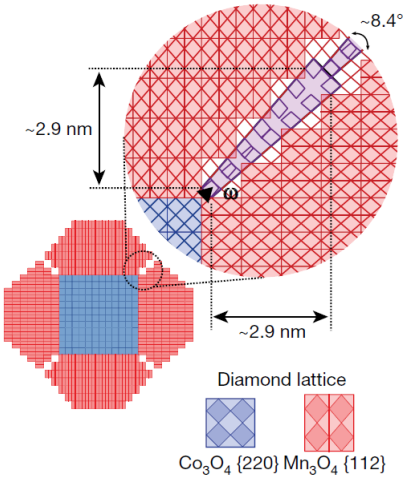

Figure 2.6. Illustration of the gaps between adjacent Mn_3O_4 grains resulting in disclinations at the Mn_3O_4 GBs. The misorientation angle between the neighbouring Mn_3O_4 {112} is ~8.4°. The disclination line is designated as a black triangle with Frank vector, $\overline{\boldsymbol{\omega}}$.

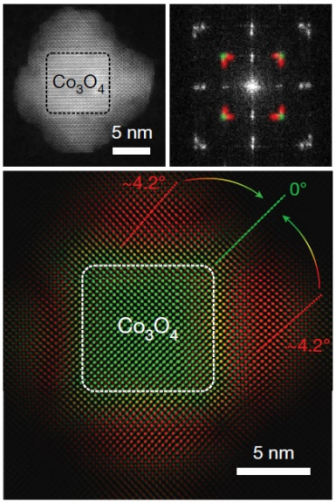

Figure 2.7. The GBs observed in the HAADF-STEM image and a corresponding lattice spacing map. The green and red spots in the FFT image were used to visualize the lattice spacing distribution in the nanocrystal. In the map, the interface between the Co_3O_4 nanocrystal and the Mn_3O_4 GBs is mapped as green, showing that the lattice spacing at the interface is 2.85 Å (Lattice spacings of the Mn_3O_4 {112} planes not affected by the Co_3O_4 core range from 2.96 to 3.09 Å (red)).

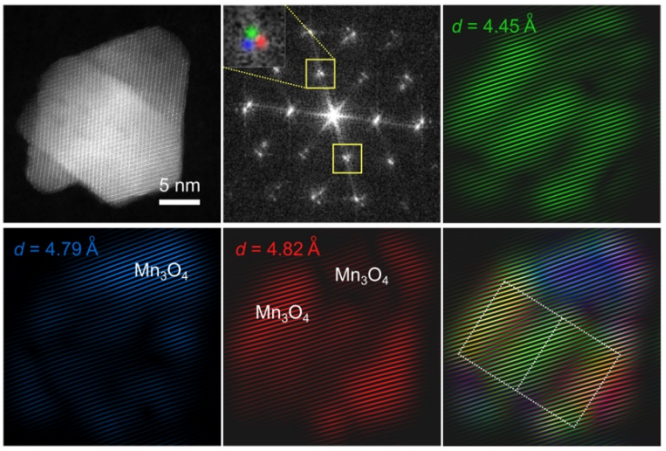

Figure 2.8. The GBs observed from the Co_3O_4 [110] zone axis. Three clustered Mn_3O_4 {011} spots (in blue, green, and red colours) in the yellow boxes reflect the differences in angle and lattice parameter of the three Mn_3O_4 grains. The FFT images reveal the strains at the Mn_3O_4 grain boundaries. The d-spacing value of the Mn_3O_4 GBs is 4.45 Å, and the values of the Mn_3O_4 grains are in the range of 4.79 and 4.82 Å. The disclinations exist at the Mn_3O_4 GBs at the edges of the Co_3O_4 nanocube core.

2.3.3 Extension of SK growth to 3D polyhedral substrates

The overall growth process can be considered to be a generalization or extension of the Stranski-Krastanov (SK) mode growth of a thin film on a two-dimensional (2D) substrate to a finite-sized 3D case. In SK growth, the thin film grows up to a critical layer thickness (h_c), which is determined by the interplay between the strain and the surface energy, followed by 3D island growth[17,18]. From the perspective of extending the SK growth to 3D nanocrystal substrates, as illustrated in Figure 2.9, the mechanism by which the grains grow to form the core/shell nanocrystals can be described as follows: The shell initially grows *via* a layer-by-layer mode on the facets of the polyhedral nanocrystal core, forming a coherent layer (CL) and accumulating epitaxial strain (Figure 2.9a). When the growth thickness exceeds h_c, the growth mode changes to island growth for strain relaxation. In particular, unless there is a GB that exerts geometric misfit-induced stress (Figure 2.7), the Co_3O_4/Mn_3O_4 core/shell nanocrystals with the minimal lattice-mismatch exhibit almost no characteristics of CL because the strain energy is so small (Figure 2.10).

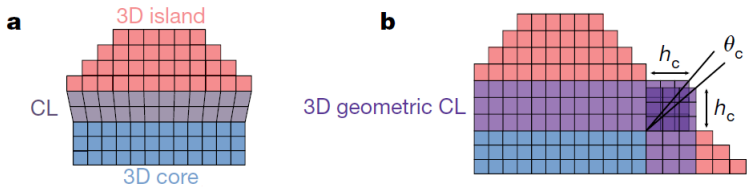

Figure 2.9. Extension of SK growth to 3D polyhedral substrates. **a-b**, Schematic illustration of traditional SK growth without geometric misfit strain (**a**) and extended SK growth with '3D geometric CL' induced by geometric misfit strain along the sharp edges of the core (**b**).

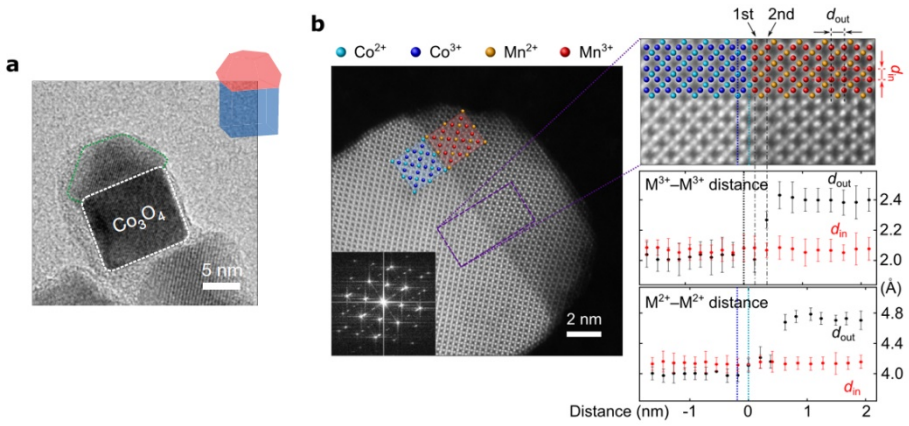

Figure 2.10. Co_3O_4/Mn_3O_4 nanocrystals without GB. **a**, TEM image of a Co_3O_4/Mn_3O_4 nanocrystal without GB. **b**, Lattice match between Co_3O_4 {400} and Mn_3O_4 {220} is reflected in the atomic resolution HAADF-STEM image. Illustration of atomic positions in Co_3O_4 and Mn_3O_4 unit cells viewed from [100] and [110] directions, respectively, is shown in STEM image. M^{3+}–M^{3+} and M^{2+}–M^{2+} distances (M=Co, Mn) along in-plane (d_{in}) and out-of-plane (d_{out}) directions are plotted as a function of relative distance from the first Co^{3+} and Co^{2+} layer, respectively. The error bars represent the standard deviation.

The CLs grown on the facets of the core are differently oriented and meet each other at a certain angle (θ_c) around the sharp edges of the core, forming tilt boundaries (Figure 2.9b). Consequently, a geometric strain arises due to the mismatch between the CL lattices rendered by anisotropic strain relaxation of the shell material[19-21]. The mismatch is particularly pronounced in the nanocrystals with an isotropic-lattice-core (i.e., cubic lattice) and anisotropic-lattice-shell (i.e., tetragonal lattice). The h_c of the CL observed for 2D epitaxy is modified in 3D epitaxy to the value at which the geometric misfit strain, in addition to the epitaxial strain, can be accommodated by the shell material. For example, the Mn_3O_4 lattice at the GBs can accommodate the elastic distortion required to create a continuous disclination with a length of three Mn_3O_4 unit cells (~ 2.9 nm; h_c)[22]. Therefore, each Mn_3O_4 shell can be divided into two regions; the '3D geometric CL' with grain boundaries (GBs) and the islands grown further from the CL (Figure 2.9b).

When the GB formation is driven energetically, precise management of the kinetic effects during the shell growth is the key to obtain the desired coverage and morphology of the shell grains[23]. In our synthetic method using oleylammonium salts, the acid/base ratio of the solution and the concentration of counteranions can be varied (Figure 2.11). The deposition rate, a kinetic parameter, and the surface energy of the growing nanocrystals, a thermodynamic parameter, are affected by both the acid/base ratio and the

counteranion concentration. The former is more sensitive to the acid/base ratio that controls the supersaturation level, and the latter is responsive to the counteranions bound to the surface. Using this synthetic system, we can limit the shell growth in a near-equilibrium thin-film growth regime.

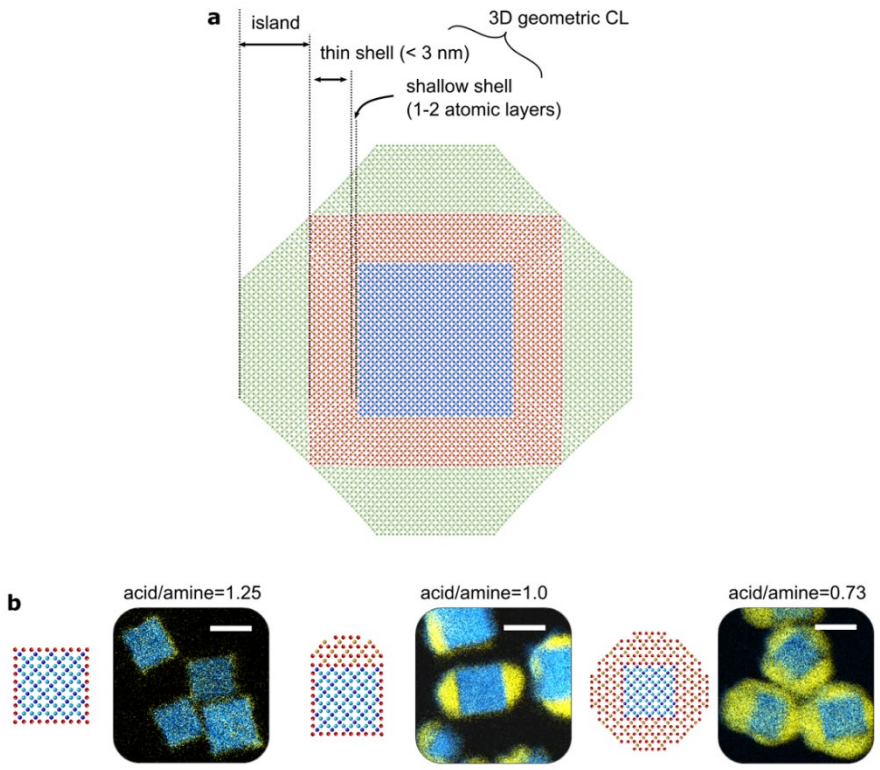

Figure 2.11. Morphology and GB structure control of multigrain Co_3O_4/Mn_3O_4 nanocrystals. **a**, 2D illustration showing the range of Mn_3O_4 grain thickness in analogy to SK growth mode. The '3D geometric CL' is determined by the geometric misfit strain along the core edge. The CL consists of two types of shells—the shallow shell made of one or two atomic layers as described above residing just above the core and a ~3 nm thick conformal shell. **b**, Number of the grains is controllable by changing the acid/amine ratio of the oleylammonium solution. Scale bars, 10 nm.

By changing the counteranions that passivate the surface of the shell, the morphology of the grains could be controlled to have CLs with (CoMn-CL+I) or without islands (CoMn-CL) (Figure 2.12). To compare the stabilizing effects of different types of counteranions, $MnCl_2$ and $Mn(HCOO)_2$ were tested. With $HCOO^-$ ions, lateral growth (i.e., wetting of the core surface) of the grains is promoted without the formation of the islands because the low surface energy can compensate for the energy expended on the epitaxial strain and even the large geometric strain to form the GBs (Figure 2.12a). On the other hand, when $MnCl_2$ is used, Mn_3O_4 islands with high surface energy tend to grow on the CLs to relax the strain, and the creation of CLs/GBs is inhibited (Figure 2.12b). For almost the same elemental composition, the Mn_3O_4 shell of CoMn-CL has larger coverage, meaning not only more grains and GBs, but also a lower height/edge-length ratio than those of CoMn-CL+I. This behaviour of the shell material, which switches the growth mode between lateral and vertical ones depending on the ligand stabilization capability, minimizes the total free energy while incorporating the geometric misfit strain[9]. To further drive the near-equilibrium growth, we designed the experiments to repeat the shell growth under the same supersaturated conditions (Figure 2.13). As a result, the shell coverage increased, and subsequently the GB number also rose, producing the nanocrystals with a near-equilibrium structure in which the grains form a closed loop.

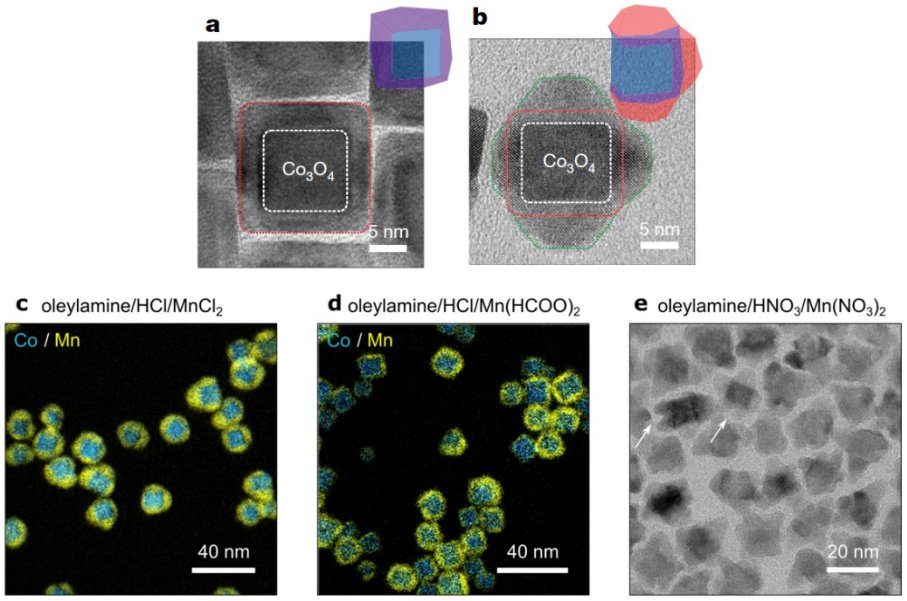

Figure 2.12. Control of morphology of grains. **a-b**, TEM images showing the effects of the counteranions in manganese (II) precursors on the morphology of Mn_3O_4 grains without island (**a**) and with island (**b**). Red and green lines in the high-resolution TEM images indicate the CL and the islands of Mn_3O_4, respectively. **c-e**, TEM images show the effect of counteranions of manganese (II) precursor on the morphology of Mn_3O_4 grains. The island growth is minimized when changing the counteranion of the precursor from chloride (**c**) to formate (**d**). The shell tends to follow the non-equilibruim growth regime when using the nitrate (**e**). In the non-equilibrium regime, even Mn_3O_4 grains grown on one side of the core are divided into several grains and grow further above the thickness of 10 nm.

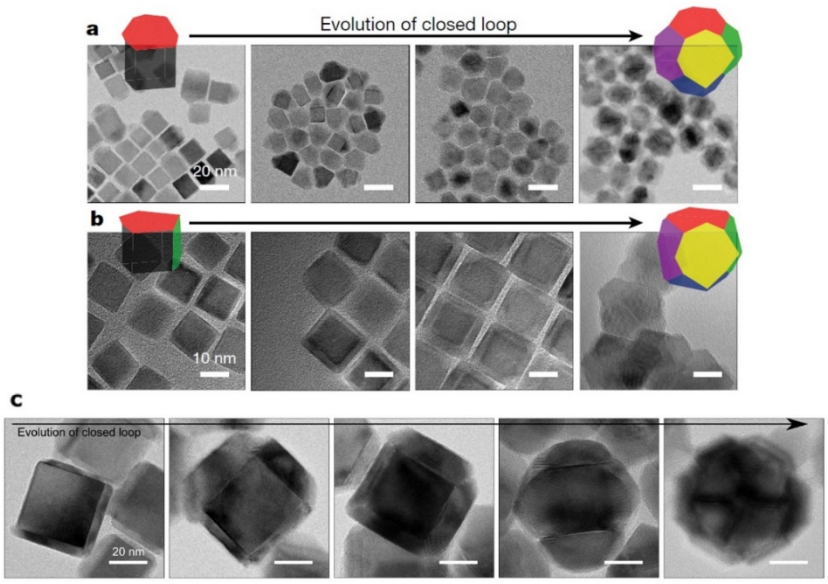

Figure 2.13. Evolution of closed loop of grains. **a-b**, The development of grains and GBs monitored while repeating the synthetic procedure using chloride (**a**) and formate (**b**) ligands with 11 nm-sized core. **c**, The development of grains and GBs by repeating the synthetic procedure using both chloride and formate ions with 30 nm-sized core.

Furthermore, we could tailor the structures of the GB defects (e.g., disclinations and dislocations) either by using different types of counteranions that can promote non-equilibrium shell growth or changing the core size (Figure 2.14) (see section 2.3.8 for more details on the non-equilibrium growth). Because of the stress-relief through the formation of dislocations at the core/shell interface or in the GBs, the GBs were extended along with the periodic/zigzag dislocations.

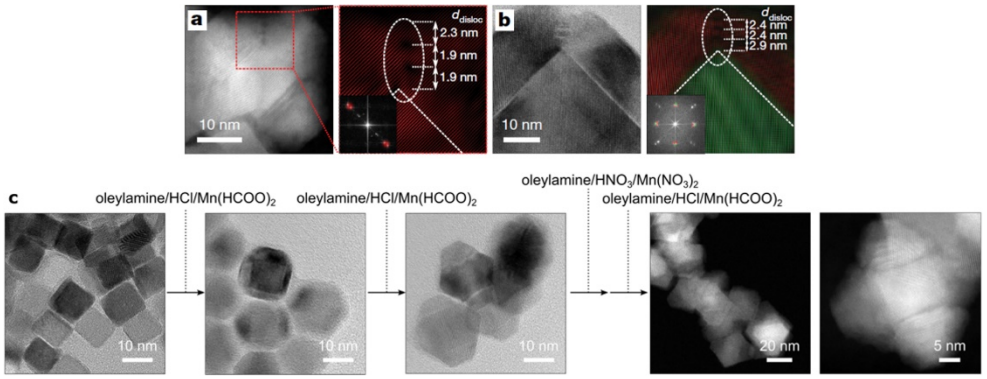

Figure 2.14. Tuning the structure of GB defects. **a-b**, STEM, TEM, and FFT images of Co_3O_4/Mn_3O_4 nanocrystals synthesized using 11 nm (**a**) and 30 nm-sized (**b**) Co_3O_4 nanocubes as cores and having GBs longer than a critical thickness. The FFT images show the induced dislocation and its spacing at the Mn_3O_4 GB. **c**, The formation of dislocations at the GB is achieved by multi-step synthesis. When synthesized with formate ions, the lateral growth of the grains is preferred, which leads to the GB formation. After that, the non-equilibrium growth is induced using nitrate ions. The Mn_3O_4 shell tends to grow further above the critical thickness of the GB with disclinations (~2.9 nm) and forms the dislocations around the GB region.

2.3.4 GB defects in Co_3O_4/Mn_3O_4 nanocrystals

The structure of the GB defects is illustrated based on the green-squared area in the HAADF-STEM image of the nanocrystal with both GB and island in (Figure 2.15). Here, d_{in} and d_{out} are defined as the interatomic spacings among the M^{2+} cations (M=Co, Mn) that are parallel (in-plane) and perpendicular (out-of-plane) to the interface, respectively, on the 2D projection of the lattice. The d_{out}/d_{in} ratio of 1.03 and the square-like shape of the unit cell at the GB in Figure 2.15b result from the rotation of Mn_3O_4 {112} planes around the Mn_3O_4 <220> axes. The FFT of the STEM images of all the CoMn-CL and CoMn-CL+I samples with GBs taken along the Co_3O_4 [100] zone axis consistently show the Bragg reflections of Mn_3O_4 (112) dispersed toward Co_3O_4 (220) reflections (Figure 2.16).

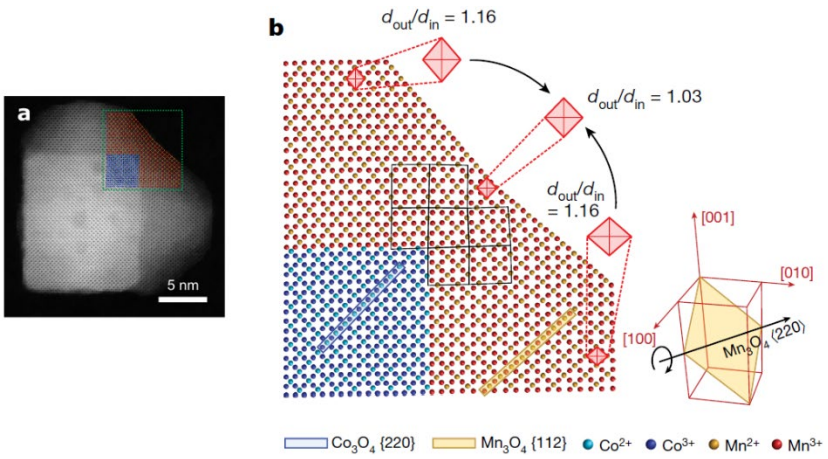

Figure 2.15. STEM image and 2D illustration showing grain boundary. **a**, HAADF-STEM image of the multigrain Co_3O_4/Mn_3O_4 nanocrystal with grain boundary. **b**, 2D illustration of the atomic arrangement of the nanocrystal with both GB and island. Black rectangles represent the distorted Mn_3O_4 unit cells viewed along the [110] direction. Mn_3O_4 {112} planes rotate around <220>.

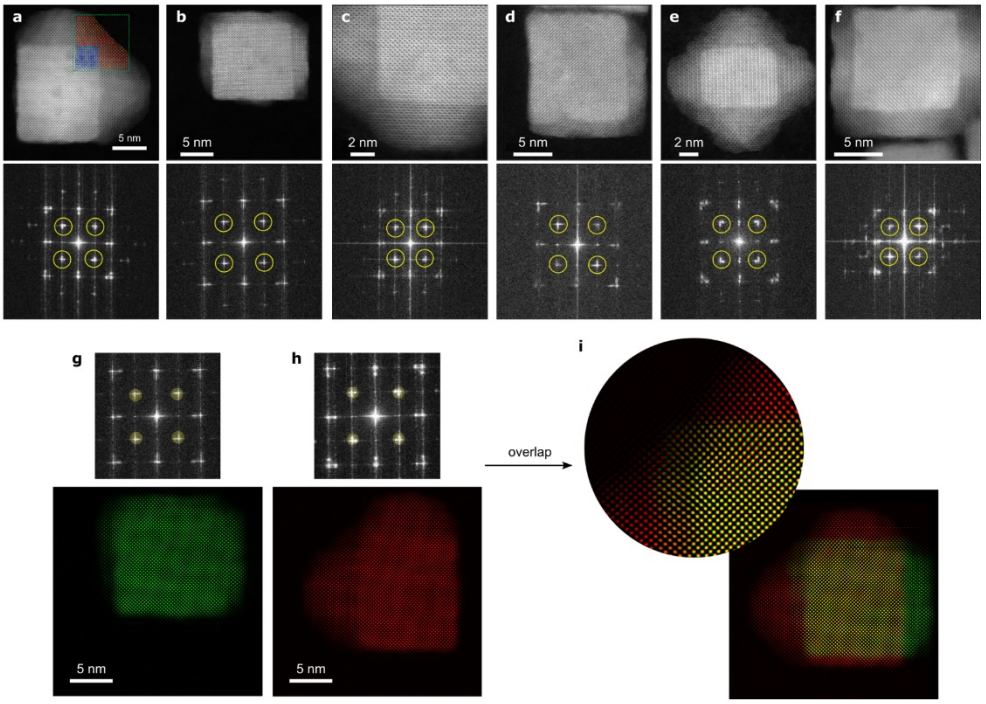

Figure 2.16. Uniformity of grain boundary structures between Co_3O_4/Mn_3O_4 multigrain nanocrystal samples. **a-f**, The HAADF-STEM images and corresponding FFT patterns of multigrain Co_3O_4/Mn_3O_4 nanocrystals. The clustered FFT reflections in yellow circles represent Mn_3O_4 {112} and Co_3O_4 {220} lattices. The Bragg reflections of Mn_3O_4 (112) planes dispersed toward Co_3O_4 (220) reflections mean that all samples have GBs in which Mn_3O_4 {112} planes rotate to match Co_3O_4 {220} planes. **g-h**, FFT patterns of nanocrystal with GB without island (**g**) and with both GB and island (**h**). **i**, Overlap between (**g**) and (**h**) FFT images and enlarged GB region show that the GB structure is almost the same with or without island.

Strain field mapping was conducted by image-processing the atomic-resolution HAADF-STEM image (Figure 2.17 and 2.18) (see section 2.3.10 for more details on the method). The extent of local distortion was presented in terms of the aspect ratio of the diamond lattice consisting of Co_3O_4 {220} or Mn_3O_4 {112} planes. The colour map images clearly show that the strain field has narrow bands of reduced d_{out}/d_{in} lattices at the GBs around the nanocube edges. The statistical distributions of the aspect ratios were extracted from the white dashed regions that correspond to the lateral views of two adjacent grains sharing a GB. The most common d_{out}/d_{in} values for the nanocrystals with islands are near 1.16, which is close to the $c/\sqrt{2}a$ value of the regular Mn_3O_4 lattice (also see Figure 2.19). On the other hand, lower values are observed for the nanocrystals without islands, which can be attributed to the distribution of tensile and compressive strains induced along Mn_3O_4 [220] and [004], respectively, due to the gap closing.

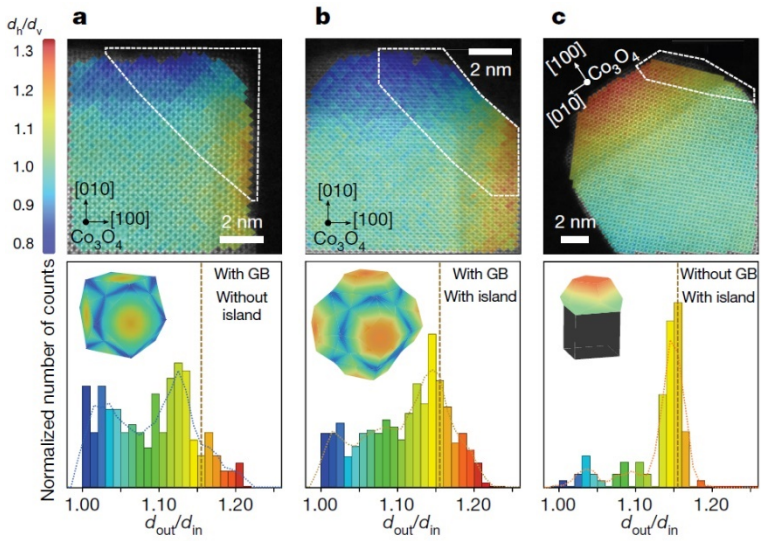

Figure 2.17. a-c, Computer-vision based image processing results for the diamond lattices consisting of Co_3O_4 {220} or Mn_3O_4 {112} planes and histograms for the aspect ratio distribution of the diamond lattices in the white-lined regions of the nanocrystals with GB/without island (**a**), with both GB and island (**b**), and without GB/with island (**c**). Coloured maps show the distribution of strained diamond lattice cells. In the maps, the horizontal length (d_h; Co_3O_4 [100] direction) of the lattice cells is divided by the vertical length (d_v; Co_3O_4 [010] direction) to distinguish the orientations of the grains. In the histogram, ratios greater than 1 are used to obtain the d_{out}/d_{in} values, i.e. the larger of d_h/d_v and d_v/d_h. The insets show 3D models illustrating the strain field of the Mn_3O_4 grains. Vertical dotted lines represent the aspect ratio (1.16) of unstrained Mn_3O_4.

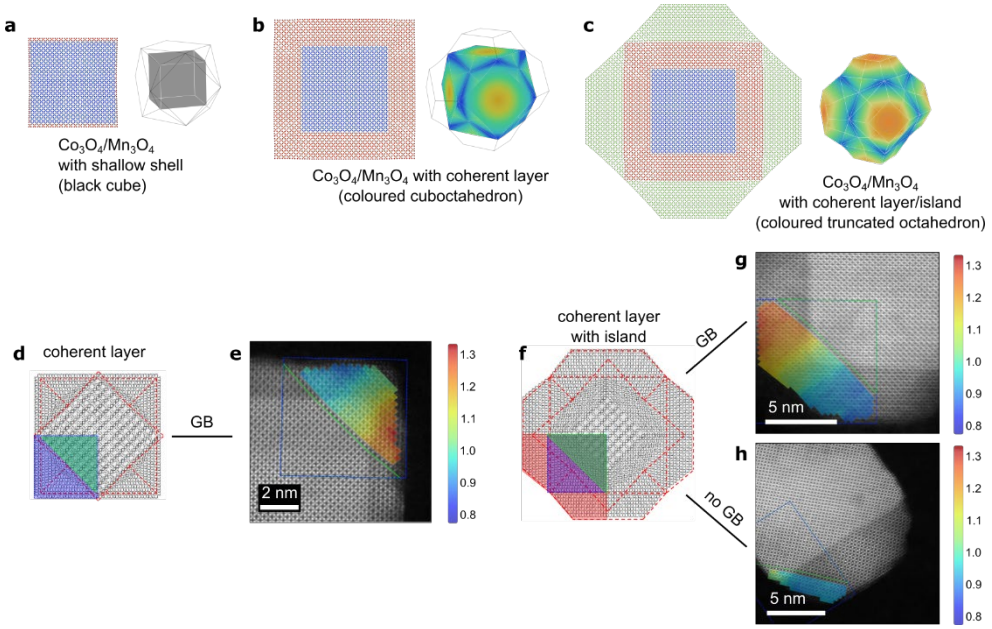

Figure 2.18. Comparison of Co_3O_4/Mn_3O_4 nanocrystal with- and without island. **a-c**, 2D atomic arrangements and 3D models of Co_3O_4/Mn_3O_4 nanocrystal with shallow Mn_3O_4 shell with one to two atomic layers (**a**), with GB/without island (**b**), and with both GB and island (**c**) samples. The 3D geometric coherent layer was grown in the transparent region of 3D model in (**a**), and their limit thickness was about ~2.9 nm. Islands were grown in the transparent region (truncated pyramidal region) of 3D model in (**b**). (blue dots, red dots, and green dots in 2D represent Co_3O_4, coherent layers of Mn_3O_4, and islands of Mn_3O_4, respectively.) **d-h**, 3D illustrations, compartments, and STEM images of Co_3O_4/Mn_3O_4 multigrain nanocrystals with coherent layer (**d,e**), coherent layer together with island (**f,g**), and with island/without coherent layer (**h**) for a fair comparison of strain distributions. The blue

coloured square contains a 2D projection of GB between two grains viewed along [110] direction of Mn_3O_4, attached on lateral plane of the Co_3O_4 cube. The green coloured triangle indicates the surface of island on another Mn_3O_4 grain on top of Co_3O_4 cube viewed along [001] direction of Mn_3O_4. The diamond lattice in the blue square of the vertex projection are enclosed by Mn_3O_4 {112} planes, while those in the green triangle are enclosed by Mn_3O_4 {220} planes. Red coloured region indicates {011} planes of Mn_3O_4 island, attached on lateral plane of the Co_3O_4 cube. To exclude the overlapped region by the top grain in the projection, we considered the aspect ratios in the blue and red regions only. The aspect ratios were calibrated to correct the scan distortion (the ratios were divided by 1.066 for (**e**), 1.06 for (**g**), and 1.063 for (**h**). The values in the Co_3O_4 region were used as zero strain. Histograms for each distribution of the computed aspect ratios are shown in Figure 2.17.

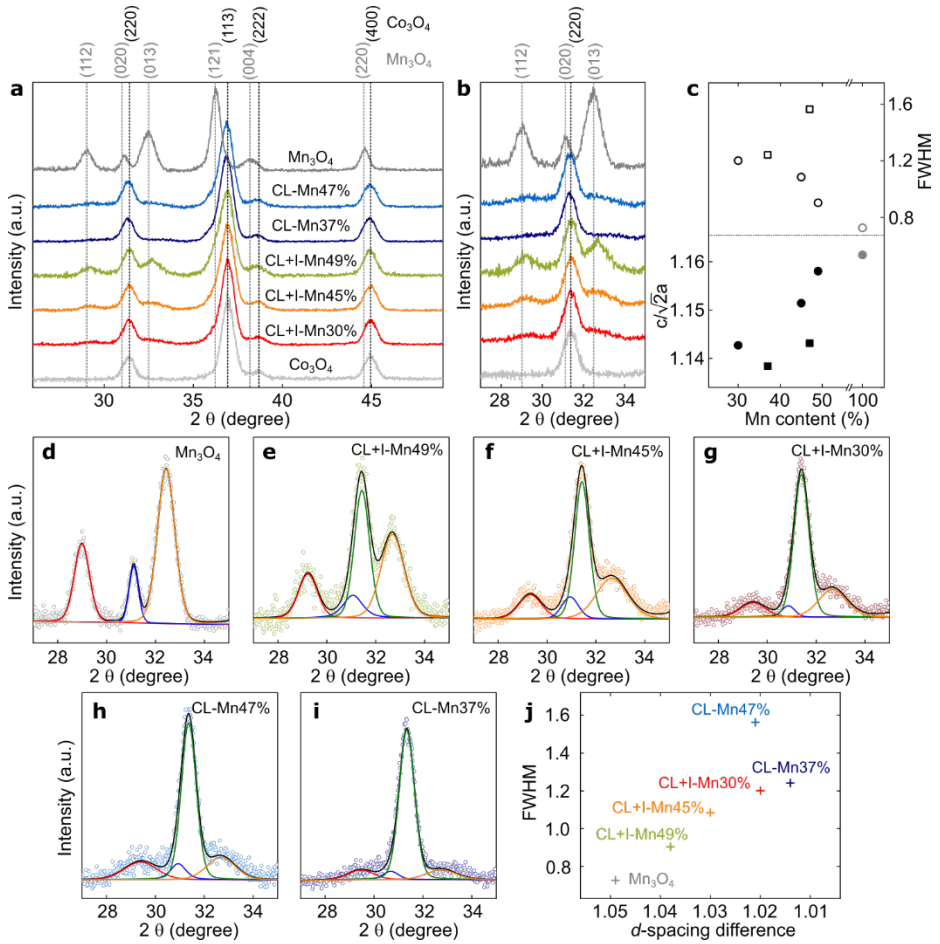

Figure 2.19. XRD analysis of CoMn-CL+I and CoMn-CL samples with different Mn contents. **a-b**, XRD patterns of thickness-controlled samples. **c**, Full-width at half-maximum (FWHM) of the Mn_3O_4 (112) peak at ~29 degree and estimated $c/\sqrt{2}a$ values (a and c are lattice parameters obtained from the XRD analysis) of Mn_3O_4 nanocrystals (dark gray), Mn content-controlled CoMn-CL+I (black circles), and CoMn-CL (black squares) samples. All patterns were aligned to Co_3O_4 (400) peak at 44.9 degrees with FWHM of 0.7676 degrees using Si (400) peak as a reference. Co_3O_4 XRD pattern is

refined using Rietveld analysis. The samples were redesiginated with their Mn contents (for example, CL+I-Mn49% sample is CoMn-CL+I containing 49% Mn). The value of $c/\sqrt{2}a$ is estimated by using the lattice parameters of (112) and (220) planes, and plotted as a function of Mn contents (%). The lattice parameter of (*hkl*) plane was estimated by using the following equation:

$$\frac{1}{d^2} = \frac{h^2+k^2}{a^2} + \frac{l^2}{c^2}$$

d-i, XRD patterns in the range of 27–35 degree with individual peak profiles and calculated peak profiles. **j**, FWHM of (112) peak at ~29 degree as a function of the difference in d-spacing between Mn_3O_4 (112) peak and Mn_3O_4 (220) peak at ~44.9 degree. The $c/\sqrt{2}a$ value of as-synthesized Mn_3O_4 nanocrystals (dark gray) using the above equation matches well with the known ratio of normal (unstrained) Mn_3O_4, which is 1.16 (a=b=5.765 Å, c=9.442 Å, JCPDS #80-0382). Since the islands are less strained, the average d_{out}/d_{in} value of the islands from TEM images, which can be related to $c/\sqrt{2}a$ from XRD, is close to that of normal Mn_3O_4. The $c/\sqrt{2}a$ value decreases by reducing the percentage of unstrained Mn_3O_4 in the nanocrystal, which is achieved by reducing the amount of Mn in the multigrain nanocrystal. The FWHM of CL-47% sample is much greater than that of CL+I-Mn49% sample and the difference in *d*-spacing is much smaller. Regardless of the different FWHM values, the areas under the (112) peak profile of each sample are

almost the same (~37 counts × degrees). These data show that the *d*-spacings of (112) planes in CL-Mn47% sample are more diverse than those in CL+I-Mn49% sample. The result means that the Mn_3O_4 (112) grain boundary plane of CL-Mn47% sample is more strained than that of CL+I-Mn49% sample. When rhombohedral distortion exists, the (112) peak is divided into (112), (1-12), (-112), and (-1-12) peaks. Broadening of Mn_3O_4 (112) reflection in all the samples can be attributed to rhombohedral distortion.

The local strain distribution is reflected in the electron diffraction (ED) patterns and powder XRD data through the reasonably uniform grain configuration in the nanocrystals (Figure 2.19, 2.20, and 2.21). The GB areas and gap angles are almost identical for all the GBs, implying that the residual stresses associated with the gap closing between two grains near each GB are almost the same. At the given residual stress, an island appears to have a less normal strain per plane than a CL according to the strain field mapping. The Mn_3O_4 (112) XRD peak for the CoMn-CL nanocrystals is broader than that for the CoMn-CL+I nanocrystals at a similar Mn content, which indicates a higher proportion of nonuniform deformation due to the smaller volume or the absence of islands. Such uniformity in the GB structure provides a valuable opportunity to investigate the properties of strained GB structures, which are otherwise hard to achieve[5]. For instance, one can obtain the correlation between the microscopic defect structures and the ensemble properties.

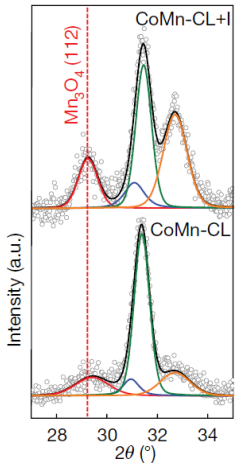

Figure 2.20. XRD patterns and calculated peak profiles of Co_3O_4/Mn_3O_4 nanocrystals with GBs. Individual peak profiles are Mn_3O_4 (112) (red), (020) (blue), (013) (orange), and Co_3O_4 (220) (green). FWHM of Mn_3O_4 (112) peak increases significantly from 0.90° for CoMn-CL+I to 1.56° for CoMn-CL.

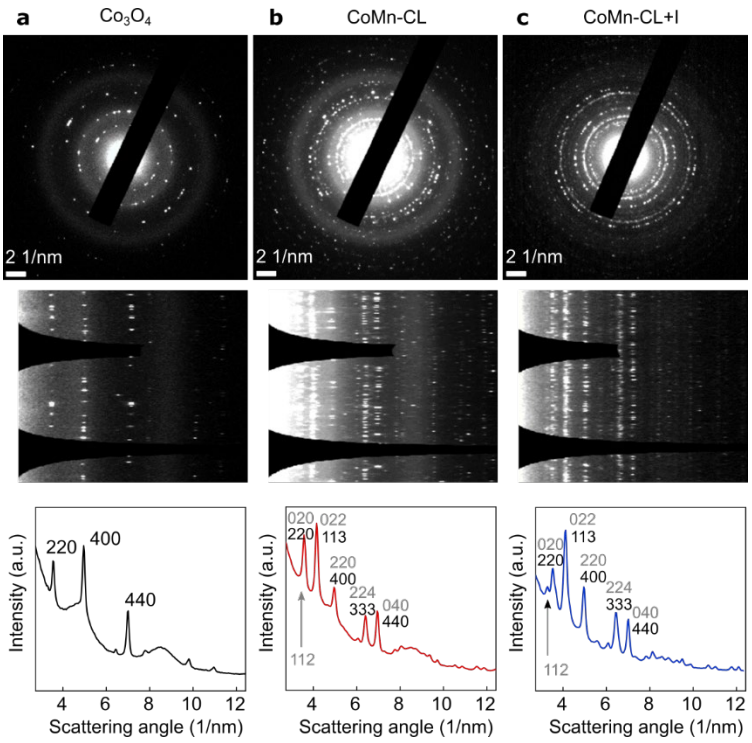

Figure 2.21. a-c, Selected-area electron diffraction (SAED) pattern of Co_3O_4 (**a**), CoMn-CL (**b**), and CoMn-CL+I (**c**) samples. Black coloured letters and gray coloured letters in plots represent Co_3O_4 planes and Mn_3O_4 planes, respectively. The peak of (112) scattering angle is clearly shown in CoMn-CL+I sample.

2.3.5 Strain tensor measurements of Co_3O_4/Mn_3O_4 nanocrystal

When the gap closes, not only is there normal strain and the accompanying Poisson's effect, but also shear strain and rotation of unit cells at the GBs due to the high elastic anisotropy of orthotropic Mn_3O_4[24]. The more accurate strain tensor measurement[25], which is on the scale of 0.5 nm, shows that the normal strain and the rotation are the principal deformation components (Figure 2.22, 2.23, and 2.24) (see section 2.3.11 for the algorithm). In both the nanocrystals with and without islands, the aspect ratios of the unit cells at the GBs are close to unity. Furthermore, the sizes of the unit cells increase with increasing distance from the Co_3O_4/Mn_3O_4 interface, and the values are very similar for those at the same distance. Interestingly, the Mn_3O_4 shell accommodates a large 3D strain (~8% for each axis) per GB without producing any dislocations. The value is quite large compared to Au decahedral nanoparticles, another material well known to exhibit GBs within nanocrystals[16]. Moreover, we demonstrated that the GBs in the form of disclinations could also be created in the core/shell nanocrystals of other material combinations, such as Fe_3O_4/Mn_3O_4, Mn_3O_4/Co_3O_4, Fe_3O_4/Co_3O_4, and Pd/Au, *via* geometric misfit.

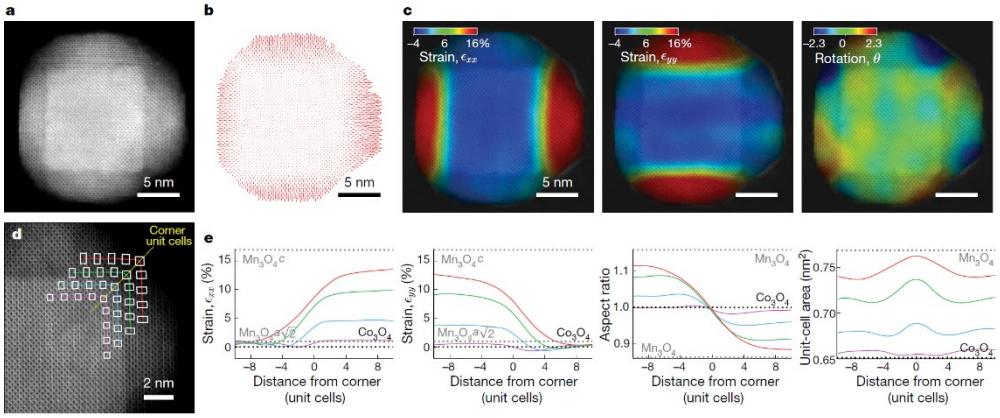

Figure 2.22. Strain tensor measurements of Co_3O_4/Mn_3O_4 nanocrystal. **a**, HAADF-STEM image of the nanocrystal. **b**, A map of displacement based on the atomic position of Co_3O_4. **c**, Infinitesimal strains and rotation for *x* and *y* directions and rotation of the unit cell. **d**, Line traces (coloured lines) and unit cells (white rectangles) showing the change in aspect ratio and volume of the unit cells. **e**, The infinitesimal strains for *x* and *y* directions, aspect ratio, and unit cell area over the line traces shown in (**d**).

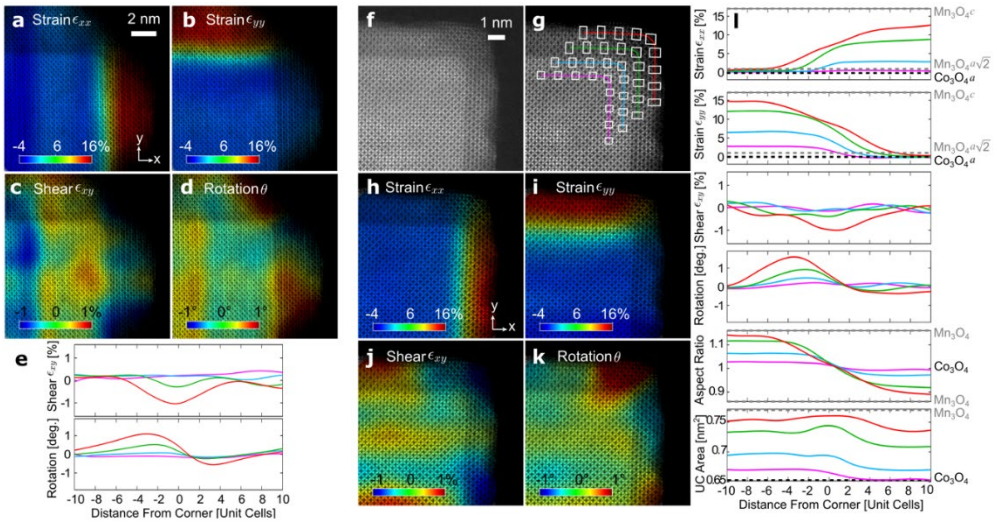

Figure 2.23. Strain tensor measurements of CoMn-CL+I and CoMn-CL. **a-e**, Strain tensor measurements for the nanocrystals with both CL and island. Location of line traces are shown in Fig. 4d and plotted in (**e**) with distorted unit cells shown in white, where strains are exaggerated by a factor of 6. **f-l**, Strain tensor measurements for the nanocrystals with CL and without island. HAADF STEM image in (**f**) was taken along the Co_3O_4 [100] zone axis. Line traces (**l**) at the locations shown in (**g**), for strain in the x-direction, strain in the y-direction, shear, rotation, unit cell aspect ratio, and unit cell area, respectively, from top to bottom. Infinitesimal strains (**a-b**, **h-i**) colored from -4% (blue) to +16% (red) for x and y directions, respectively. Shear strain (**c**,**j**) colored from -1% to +1%. Infinitesimal rotation (**d**,**k**) colored from -1 to +1 degrees. Where appropriate, dashed lines of reference values are shown for Co_3O_4 and Mn_3O_4.

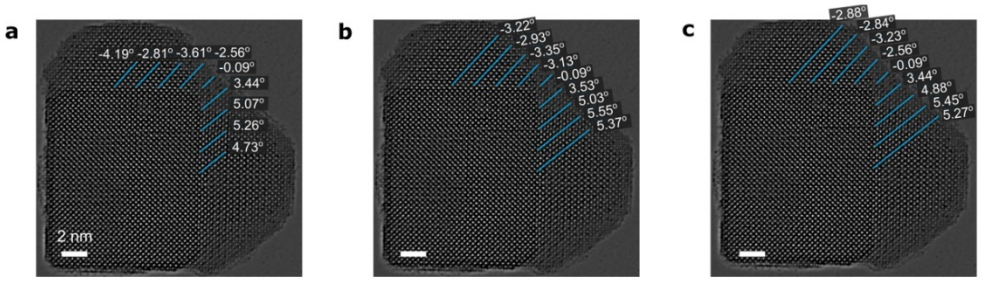

Figure 2.24. a-c, Lattice angles of Mn_3O_4 (112) planes relative to Co_3O_4 (220) planes in Co_3O_4/Mn_3O_4 nanocrystal with GB/island are estimated based on the peak fitting method. The angle is measured in the range of 2 unit cells (**a**), 4 unit cells (**b**), and 5 unit cells (**c**). The average lattice angles were measured from the relaxed middle island region to the GB region, which decreased from ~4.5° to 0°. The lattice near the GB surface tends to be distorted more than that in the middle of the island. For example, the angle of -4.19° in (**a**) is gradually decreased to -3.22° (**b**) and -2.88° (**c**).

2.3.6 The GB defects in other material combinations

A similar local 3D strain field to that in the Co_3O_4/Mn_3O_4 nanocrystals is observed in the core/shell Fe_3O_4/Mn_3O_4 nanocrystals (Figure 2.25). On the well-defined truncated octahedron Fe_3O_4 core, Mn_3O_4 {011} planes meet each other with a misorientation angle of ~15.4°. The lattice misorientation is originated from the symmetry incompatibility between cubic Fe_3O_4 and tetragonal Mn_3O_4. In Mn_3O_4/Co_3O_4 nanocrystals, the symmetry incompatibility between the tetragonal Mn_3O_4 and cubic Co_3O_4 grains induces a tensile strain along the Co_3O_4 {400} planes—lattice-matching with the Mn_3O_4 {004} planes—and a lattice misorientation between the Co_3O_4 {222} planes—lattice-matching with the Mn_3O_4 {022} planes (Figure 2.26). The strain and the misorientation collectively lead to the creation of an anisotropic grain geometry of Co_3O_4 shell. The 2D illustration shows the large tensile strain of about ~14.4% induced in the Co_3O_4 planes sharing the interface along the Mn_3O_4 <001> direction. Due to the large symmetry difference between Mn_3O_4 and Co_3O_4, the angle between Co_3O_4 {200} and {222} planes and that between Mn_3O_4 {400} and {011} are different. Therefore, the Co_3O_4 {222} planes grown on the Mn_3O_4 {011} planes are not only highly strained but also misoriented from those grown on the Mn_3O_4 {004} planes. Thus, the shell lattice on the top/corner facets is geometrically strained, and the strain spreads out toward the shells on the corner facets, resulting in the segmentation of the shells

into the multiple grains. This geometric misfit strain leads to the segmentation that occurs in the middle region of the core facets. The estimated averaged angle difference between the lattices of adjacent grains is ~8.3º. The dispersion of the spots in the FFT image clearly shows the large strain.

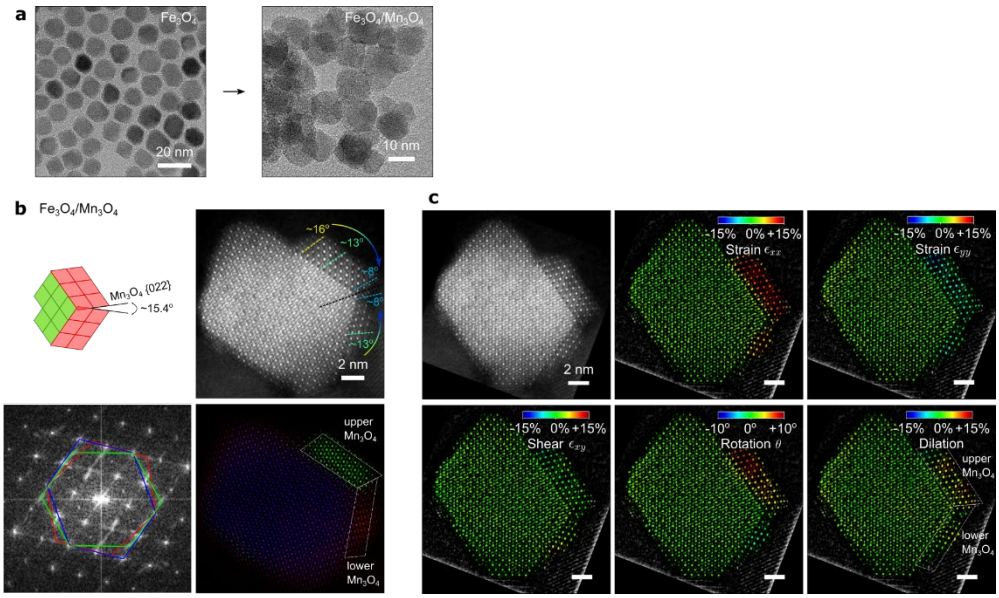

Figure 2.25. Geometric misfit strain induced GB defects in Fe_3O_4/Mn_3O_4 nanocrystals. **a**, TEM images of Fe_3O_4 core nanocrystals and Fe_3O_4/Mn_3O_4 nanocrystals. **b**, HAADF-STEM image is obtained along Fe_3O_4 <110> direction. The illustration shows the gap closing of Mn_3O_4 {022} planes and the GB formation between neighboring Mn_3O_4 grains in Fe_3O_4/Mn_3O_4 nanocrystals. The octahedral coordinations of Fe^{3+} viewed along <110> (green diamond) and those of Mn^{3+} viewed along <100> (red diamond) show the orientational relationship between the Fe_3O_4 core and the epitaxially grown Mn_3O_4. The misorientation between neighboring Mn_3O_4 {022} is ~15.4°. As the growth direction is guided by the octahedron Fe_3O_4 core, Mn_3O_4 shells can be segmented into grains based on their lattice angles. **c**, Strain tensor measurements in terms of infinitesimal strains for *x* and *y*

directions, shear strain, rotation, and dilation of the Fe_3O_4/Mn_3O_4 nanocrystal. The dilation values are estimated by the sum of strain e_{xx} and e_{yy}, which are obtained by measuring the changes in the projected unit cell area.

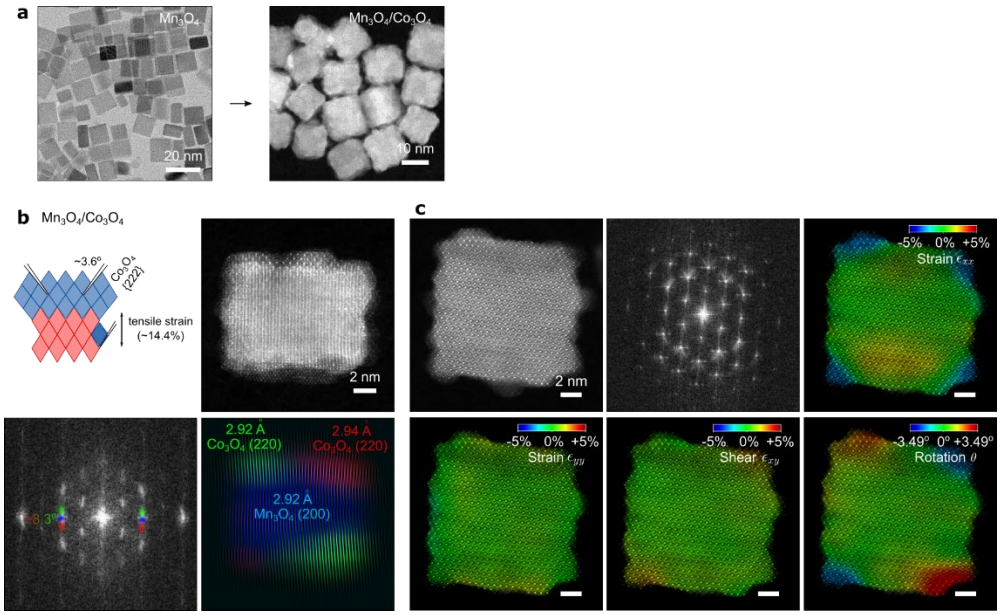

Figure 2.26. Geometric misfit strain induced GB defects in Mn_3O_4/Co_3O_4 nanocrystals. **a**, TEM and STEM image of Mn_3O_4 core nanocrystals and Mn_3O_4/Co_3O_4 nanocrystals, respectively. **b**, HAADF-STEM images obtained along Mn_3O_4 <100> direction. The illustration shows the gap closing of Co_3O_4 {222} planes. The octahedral coordinations of Mn^{3+} viewed along <100> (red diamond) and those of Co^{3+} viewed along <110> (blue diamond) show the orientational relationship between the Mn_3O_4 core and the epitaxially grown Co_3O_4 as well as between the Co_3O_4 grains. The misorientation, ~3.6°, between Co_3O_4 {222} planes in top Co_3O_4 grains is originated from the symmetry incompatibility between core and shell. When the Co_3O_4 shell is grown on the Mn_3O_4 {100} or {110} planes creating the interface along Mn_3O_4 <001> direction, the shell is under tensile strain

(~14.4%). This considerably high strain minimizes the growth of the Co_3O_4 on the Mn_3O_4 {100} planes. **c**, Strain tensor measurements in terms of infinitesimal strains for *x* and *y* directions, shear strain, and rotation of the Mn_3O_4/Co_3O_4 nanocrystal.

We also observed different geometries in grain-division for the cubic core/cubic shell samples. For example, in the Fe_3O_4/Co_3O_4 nanocrystals, when Co_3O_4 grains are grown on the eight {111} facets of a Fe_3O_4 octahedron-shaped core, the growth guidance by Fe_3O_4 core have some degree of freedom (or frustration) in their lattice orientation (Figure 2.27). In addition to that, the symmetry difference between the core and the shell, which leads to the geometric misfit strain, arises from the strained lattice as a result of lattice misfit (~3.7%) between Fe_3O_4 and Co_3O_4. The lattice misorientation and the change in the lattice parameter of the Co_3O_4 planes are shown from the Bragg reflections in the FFT image. The tensile strain induced in each Co_3O_4 shell grown on the facets of the core results in the rotation of the lattice.

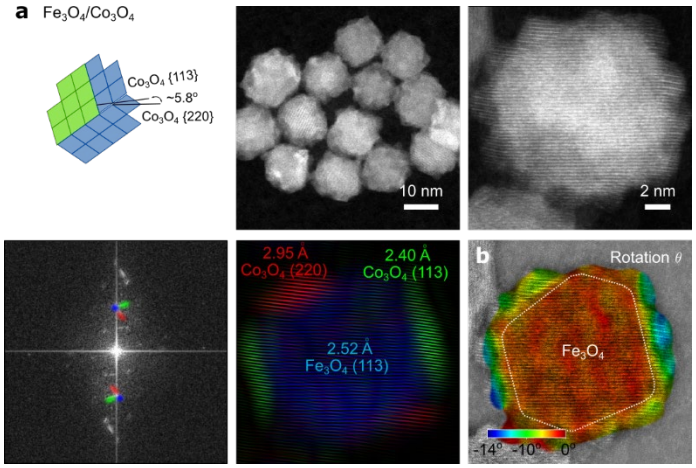

Figure 2.27. Geometric misfit strain induced GB defects in Fe_3O_4/Co_3O_4 nanocrystals. **a**, Formation of multigrains of Co_3O_4 grown on the Fe_3O_4 core induced by geometric misfit strain. The growth guidance by Fe_3O_4 core and the large lattice misfit strain (~3.7%) result in the grain segregation of the Co_3O_4 shell. **b**, The rotational tensor measurement shows that the Co_3O_4 {113} planes, which is epitaxially grown along the Fe_3O_4 {113} planes, gradually bend as thicker the shell due to the epitaxial strain relaxation and the gap closing between neighboring grains.

The metallic pair, Pd/Au nanocrystals, exhibit an octahedral grain geometry similar to the Co_3O_4/Mn_3O_4 nanocrystals (Figure 2.28). The Pd core and the Au shell both have a cubic phase (Fm-3m), and the lattice mismatch between them is about ~4.7% along (200) lattices when estimated from bulk lattice parameters. When the epitaxial strain energy is high enough, the interface plays a critical role in inducing the geometric misfit strain in the nanocrystal. The symmetry difference between Pd and Au arises from the pseudomorphic epitaxial shell near the Pd/Au interface. The lattice angle change due to the epitaxial strain at the interface causes the gaps between the Au {220} lattices at the edges of the Pd nanocube core. Consequently, the Au shells grown on the Pd nanocubes are segmented by the tilt boundaries near the edges of the core and show disclinations of ~4° for the gap closing. This lattice misorientation at the GBs is observed in both core/shell nanocrystals with 14 (**b**) and 9.5 nm (**d**) core sizes.

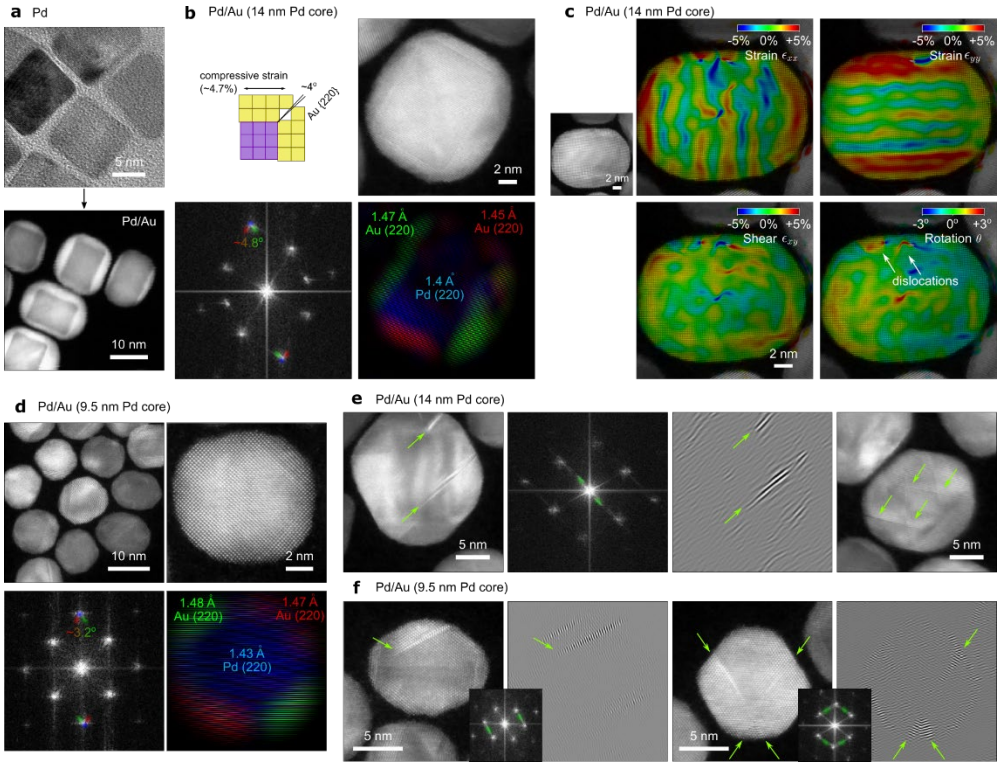

Figure 2.28. Formation of metallic multigrain nanocrystals induced by geometric misfit strain. **a**, TEM and STEM image of Pd core nanocrystals and Pd/Au nanocrystals, respectively. **b**, HAADF-STEM and corresponding FFT images of multigrain Pd/Au nanocrystals obtained using 14 nm (diagonal) Pd core obtained along <100> axis of the core. Gap closing of Au {220} planes due to the misorientation is ~4.8°. **c**, Strain tensor measurements in terms of infinitesimal strains for *x* and *y* directions, shear strain, and rotation. **d**, The grain division is also observed in the Pd/Au nanocrystals with 9.5 nm-sized core. **e-f**, Dislocations in the core/shell Pd/Au nanocrystals. HAADF-STEM images were taken along Pd <110> zone axis. Dislocations form in both kinds

of Pd/Au nanocrystals with 14 (**e**) and 9.5 nm-sized (**f**) cores. The density of the dislocations seems higher in the nanocrystals with 14 nm-sized cores than with the 9 nm-sized cores. The {111} slip planes are indicated by green arrows. The dislocations cause the sectioning of the Au grains, resulting in the generation of sub-grains.

2.3.7 Chemical compositions at the Co_3O_4/Mn_3O_4 interface and the Mn_3O_4 GBs

In Figure 2.10b, d_{in} and d_{out} are defined as the interatomic spacings of M^{3+}–M^{3+} and M^{2+}–M^{2+} distances (M=Co, Mn) parallel (in-plane) and perpendicular (out-of-plane) to the interface, respectively, on the 2D projection of the lattice. When plotted against the distance from the interface, the d_{out} value of the second M^{3+} atomic plane of the Mn_3O_4 lattice is significantly smaller (~5.6%) than the value for third and later the atomic planes, while d_{in} is almost independent of the distance. On the other hand, d_{out} value of the M^{2+} atomic plane near Co_3O_4/Mn_3O_4 interface is larger (~3%) than the rest of the atomic planes. Electron energy loss spectroscopy (EELS) spectra in Figure 2.29 show the dominance of Co^{2+} and Mn^{n+} (n>3) ions at the interface. DFT calculation of the surface energy revealed that, $Mn^{o}{}_2O_4$ (Mn^{o}=Mn at octahedral sites) surface and $Mn^{o}{}_2O_4$-Co^{t} (Co^{t}=Co at tetrahedral sites) interface are energetically more favourable than other types of surfaces or interfaces for the whole range of oxygen chemical potentials where both Co_3O_4 and Mn_3O_4 are stable (Table 2.1). Therefore, the abrupt change in the interatomic distance at the interface is attributed to the electron transfer from Mn^{3+} to Co^{2+} that results in creating Mn^{n+}(n>3)–Co^{2+} polar interface.

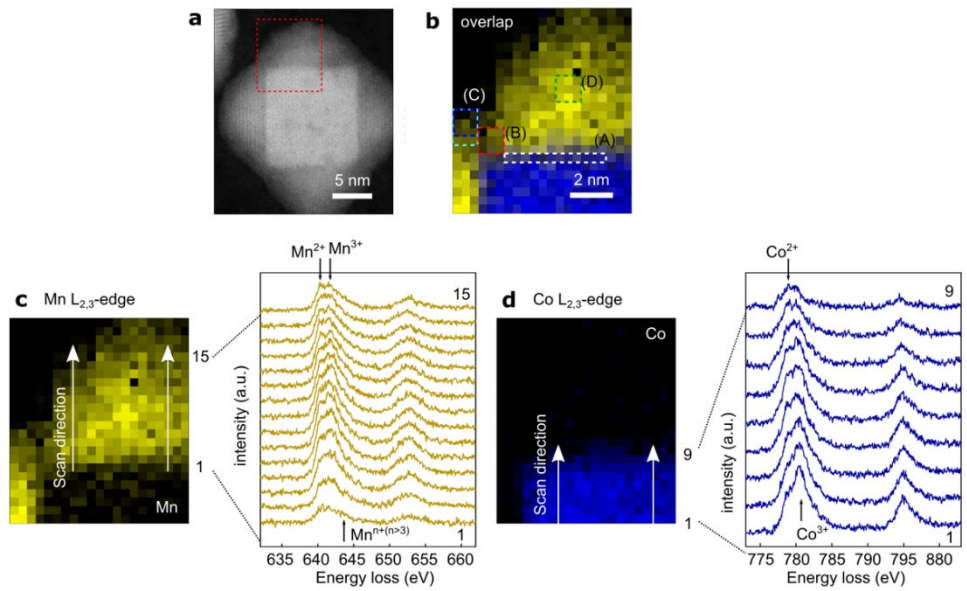

Figure 2.29. EELS analysis of a Co_3O_4/Mn_3O_4 nanocrystal. **a-b**, HAADF-STEM image (**a**) and the corresponding EELS elemental map (**b**) of a Co_3O_4/Mn_3O_4 nanocrystal show the separated domains of Co (blue) and Mn (yellow) in the nanocrystal. **c-d**, EELS spectra of Mn $L_{2,3}$-edge (**c**) and Co $L_{2,3}$-edge (**d**) measured along the scan direction. The spacing for the consecutive EELS spectra is 3.8 Å.

	Oxygen Poor Limit (μO = -1.48 eV)	Oxygen Rich Limit (μO = -1.94 eV)
$Mn^{o}_{2}O_{4}$-Co^{t}- $Co^{o}_{2}O_{4}$-Co^{t}- …[1]	79.5 meV/Å$_2$	88.9 meV/Å$_2$
$Mn^{o}_{2}O_{4}$-Mn^{t}- $Co^{o}_{2}O_{4}$-Co^{t}- …[2]	82.6 meV/Å$_2$	92.0 meV/Å$_2$
$Mn^{o}_{2}O_{4}$-Mn^{t}- $Mn^{o}_{2}O_{4}$-Co^{t}- $Co^{o}_{2}O_{4}$-Co^{t}- …[3]	76.9 meV/Å$_2$	86.3 meV/Å$_2$
$Mn^{o}_{2}O_{4}$-Mn^{t}- $Mn^{o}_{2}O_{4}$-Mn^{t}- $Co^{o}_{2}O_{4}$-Co^{t}- …[4]	87.3 meV/Å$_2$	96.7 meV/Å$_2$
$Mn^{o}_{2}O_{4}$-Mn^{t}- $Mn^{o}_{2}O_{4}$-Mn^{t}- $Mn^{o}_{2}O_{4}$-Co^{t}- …[5]	88.1 meV/Å$_2$	97.5 meV/Å$_2$
Mn^{t}-$Co^{o}_{2}O_{4}$- Co^{t}-$Co^{o}_{2}O_{4}$-…[6 or 1']	124.4 meV/Å$_2$	115.0 meV/Å$_2$
Mn^{t}-$Mn^{o}_{2}O_{4}$- Mn^{t}-$Co^{o}_{2}O_{4}$ …[7 or 2']	123.1 meV/Å$_2$	113.7 meV/Å$_2$

Superscripts o and t stand for metal cations in octahedral and tetrahedral sites, respectively.

Table 2.1. Surface energies for various surface configurations.

In the EELS spectra, the $L_{2,3}$-edges of Co and Mn overlap near the interface. Because the HAADF-STEM image (Figure 2.29a) was not taken exactly along the Co_3O_4 <100> direction, both Co and Mn L-edge spectra could be detected at the interfacial region, rendering the Co_3O_4 and Mn_3O_4 phases in the 2D-projected EELS spectra seemed generally mixed at the interface[26,27]. However, there are several limitations in characterizing the interface by STEM analysis. Firstly, even when a nanocrystal is sat along the Co_3O_4 <100> axis, the Co_3O_4 and Mn_3O_4 phases might appear mixed because their interface has surface steps and is not perfectly flat. Secondly, when a Mn_3O_4 grain grown on a lateral basal plane of the Co_3O_4 core extends toward the top basal plane, this extended Mn_3O_4 region can also be seen like an interfacial Mn_3O_4, making the interface look wider than the actual thickness. Therefore, an ensemble analysis by X-ray absorption near-edge structure (XANES) and DFT calculation combined with EELS data can provide more reliable information about the interfacial structure.

The oxidation state of Co in all the as-synthesized samples is ~2.62 as estimated by XANES, while that for the as-synthesized cores is ~2.72 (Figure 2.30). The oxidation state of Mn in Co_3O_4/Mn_3O_4 core/shallow shell nanocrystals is estimated to be 3.67. The slight reduction of Co and higher oxidation state of Mn can be attributed to the electron transfer from Mn to Co at the Co_3O_4/Mn_3O_4 interface as described above. This result is also supported

by the DFT calculation that implies a higher oxidation state of Mn in the octahedral sites at the interface. Since the average oxidation states of Co in all the core/shell samples have the same value, it is expected that the degree of electronic reconstruction is approximately the same for all the samples. Therefore, we can interpret that the electron transfer from Mn to Co occurs only until the shallow Mn_3O_4 shell covers the entire surface of the Co_3O_4 core. With the molar percentage of Mn of Mn_3O_4 shallow shell in the Co_3O_4/Mn_3O_4 core/shallow shell nanocrystals (4.9% Mn) and the average edge length of the Co_3O_4 cores (11.5 nm), we can calculate and explain the range of length of the electron transfer between Co_3O_4 and Mn_3O_4. The calculated thickness of the Mn atomic layers of the shallow shell is ~0.24 unit cell length along the *c*-axis (Figure 2.31). Furthermore, the diffusion coefficients of Mn and Co ions in the Co_3O_4/Mn_3O_4 nanocrystals were calculated using DFT (Figure 2.32). The activation energies for the interdiffusion of those ions at the heterointerface are relatively high at 90 °C, so the intermixing of the phases hardly occurs at our synthetic temperature. The difference between the diffusion coefficients of Mn and Co ions can lead to the lattice distortion or porosity via Kirkendall effect. However, we cannot observe any sign of hollowing or porosity at the interface. In conclusion, although the overlap region in the Mn and Co L-edge EELS spectra has a three pixel-length, the thickness of interfacial Mn^{n+} layers ($n>3$) that can participate in the interdiffusion is probably no more than two

layers (~2.26 Å; ~0.24 unit cell), which corresponds to a distance between an Mn^{3+} layer and the following Mn^{3+} layer in Figure 2.10b.

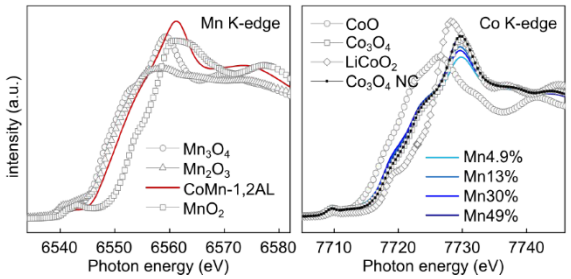

Figure 2.30. XANES spectra of Mn and Co K-edge showing the electronic reconstruction at the interface. Mn K-edge spectra of commercial manganese oxides and the Co_3O_4/Mn_3O_4 nanocrystal with shallow Mn_3O_4 shell with one to two atomic layers (CoMn-1,2AL). Co K-edge spectra of commercial cobalt oxides, as-synthesized Co_3O_4 nanocubes, and Co_3O_4/Mn_3O_4 nanocrystal samples with different Mn contents including CoMn-1,2AL, which is denoted as Mn4.9%. The oxidation state (3.67) of Mn in CoMn-1,2AL is estimated using a linear combination of XANES spectra of commercial manganese oxides. The oxidation state of Co in all as-synthesized samples is estimated to be 2.62, while that in the Co_3O_4 nanocrystal is 2.72.

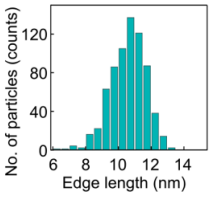

Figure 2.31. Particle size distribution of Co_3O_4 nanocubes. Considering the average edge length of Co_3O_4 core is 11.5 nm, the calculated thickness of the MnO_x atomic layers in CoMn-1,2AL sample (Mn4.9%) is about ~0.24 unit cell along *c*-axis, which is almost the same distance between the first and second Mn^{3+} layers shown in the plot in Figure 2.10b.

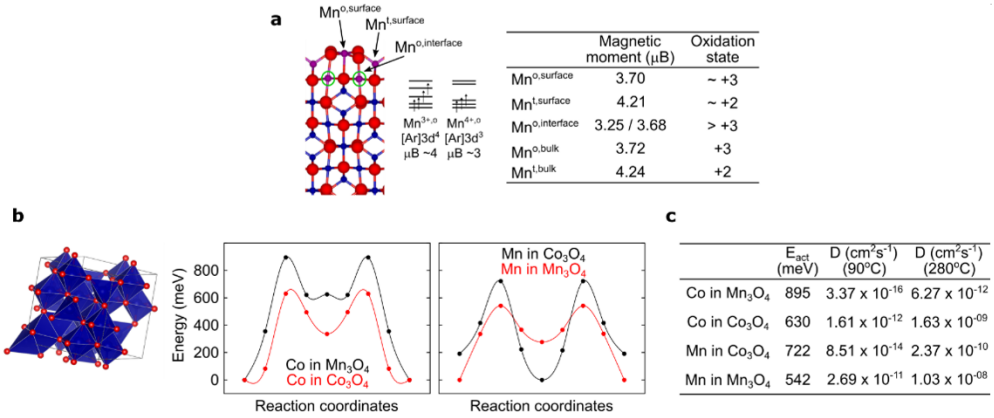

Figure 2.32. DFT calculations of the electronic structure at the interface and the diffusion coefficient of ions in the Co_3O_4/Mn_3O_4 nanocrystal. **a**, DFT calculation of electronic structure at the Co_3O_4/Mn_3O_4 interface indicates that the Mn atoms in the octahedral sites at the interface could have higher oxidation state than the octahedral Mn atoms in the bulk Mn_3O_4. Superscripts of o and t indicate octahedral and tetrahedral site, respectively. **b**, Illustration of Co_3O_4 unit cell and activation energies of Co and Mn migration in $Co_{3-x}O_4$ ($x \approx 0$) and $Mn_{3-x}O_4$ ($x \approx 0$). The reaction coordinates indicate the metastable site and can roughly correspond to octahedral site > between O–O dumbbell > tetrahedral site > between O–O dumbbell > octahedral site. **c**, Calculated activation energies for Co/Mn hopping process in the $Co_{3-x}O_4/Mn_{3-x}O_4$ ($x \approx 0$) and estimated diffusivities at 90°C, the temperature where the core/shell nanocrystals are synthesized, and 280°C. These results can support that Co_3O_4 and Mn_3O_4 phases are not energetically favorable to interdiffuse to form mixed phase at given temperature, 90°C.

The oxidation state of Mn at the Mn_3O_4 GBs shows a similar value to that for the Mn_3O_4 in the middle of the island (Figure 2.33). The Mn $L_{2,3}$-edge EELS spectra at the GB near the Co_3O_4 core (B in Figure 2.33) resemble the bulk Mn_3O_4 EELS spectra. Furthermore, the GB far from the Co_3O_4 core (C in Figure 2.33) shows a relatively small amount of Mn^{2+}. Even with the longer Mn–O bond length at the GB, the oxidation state of Mn^{2+} does not show any noticeable reduced state. By splitting the peaks of Mn 3s XPS spectra shown in Figure 2.34, we estimated the oxidation state of Mn. The magnitudes of the peak splitting are 5.9, 5.5, and 4.9 eV for MnO (Mn^{2+}), Mn_2O_3 (Mn^{3+}), and MnO_2 (Mn^{4+}), respectively. The peak splittings for the CoMn-CL and the CoMn-CL+I are 5.75 and 5.72 eV, respectively, indicating that the Mn ions in CoMn-CL are slightly more reduced than those in the CoMn-CL+I. This is because at an energy level of about 100 eV, most of the signal comes from the surface and the CoMn-CL+I exposes more shells of shallow Mn^{n+} ($n>3$) than the CoMn-CL. In the previous report, oxygen vacancies were formed at the dislocation region and Mn showed a reduced oxidation state[28]. However, in these two Co_3O_4/Mn_3O_4 samples, there is no dislocation at the GBs. Therefore, the oxygen vacancies are not generated at the GBs.

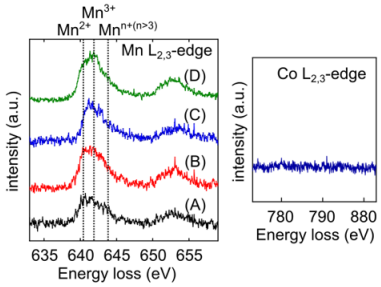

Figure 2.33. Mn- and Co $L_{2,3}$-edge EELS spectrum at the grain boundary of Mn_3O_4. The colored box regions of (A), (B), (C), and (D) in Figure 2.29b represent the Co_3O_4/Mn_3O_4 interface, a GB near the Co_3O_4 core, a GB far from the Co_3O_4 core, and the Mn_3O_4 shell far from the GB, respectively. The Mn $L_{2,3}$-edge EELS spectra resemble each other except for those from the heterointerfaces. The Co $L_{2,3}$-edge EELS spectra corresponding to the skyblue-coloured rectangular region in Figure 2.29b shows that there is no Co species.

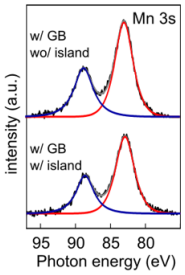

Figure 2.34. Mn 3s XPS spectra of the Co_3O_4/Mn_3O_4 nanocrystal with GB/without island (upper; CoMn-CL) and with GB/with island (lower; CoMn-CL+I).

2.3.8 Control of the defect structure of the Co_3O_4/Mn_3O_4 nanocrystals by varying the core size and the counteranion

The disclination near the GBs, for which strain energy is scaled by the square of the disclination radius (i.e., GB length), significantly increases the elastic energy. Nonetheless, since the free surface is close to the disclination (only a few nanometers away from the disclination line) and the strain relaxes through the island formation, the strain energy of the disclination remains below the critical limit where the surface energy cannot compensate the strain energy[22]. In the non-equilibrium growth process, surface and strain energy can be relaxed by the formation of plastic deformation. To induce non-equilibrium growth, we used NO_3^- anion. When using the NO_3^- ion, the surface energy cannot compensate the strain energy, resulting in the short GB, long island, and even segregation of the grains grown on the same plane (Figure 2.12e). Based on this result, the GB having the length above the critical limit is produced. We first synthesized the well-balanced Co_3O_4/Mn_3O_4 nanocrystals with ~11 nm-sized cores whose GB defects contain only elastic distortions with the length about 2.9 nm by reiterating the shell growth. On top of the pre-formed shell grains, we deposited Mn_3O_4 in the reaction solution containing NO_3^- ion. As a result, the nanocrystals with the dislocations at the GB that are longer than the critical limit are prepared (Figure 2.14a and c).

The dislocations can also be produced by the energy-balancing of surface

energy with the heteroepitaxial strain energy (i.e., large-sized core) (Figure 2.14b and 2.35). As the edge length of Co_3O_4 increases above ~20 nm, the misfit strain energy increases, and the dislocations can nucleate at the Co_3O_4/Mn_3O_4 interface (Figure 2.36). For the cores with an edge length greater than 30 nm, the stress is too high for the Mn_3O_4 to completely wet one facet of the Co_3O_4 core in the presence of Cl^- ions, octahedral shape of Mn_3O_4 grains are produced to minimize the interface area though island formation similar to the Volmer-Weber mode (Figure 2.37a). On the other hand, the lateral growth of the shell is preferred when using $HCOO^-$ ions, creating the GBs (Figure 2.37b). Furthermore, by repeating the synthetic procedure, the closed loop of the grains containing dislocations can be formed (Figure 2.14b and Figure 2.38). The dislocations at the Co_3O_4/Mn_3O_4 interface releasing the large strain energy help the GB to grow further above the critical thickness.

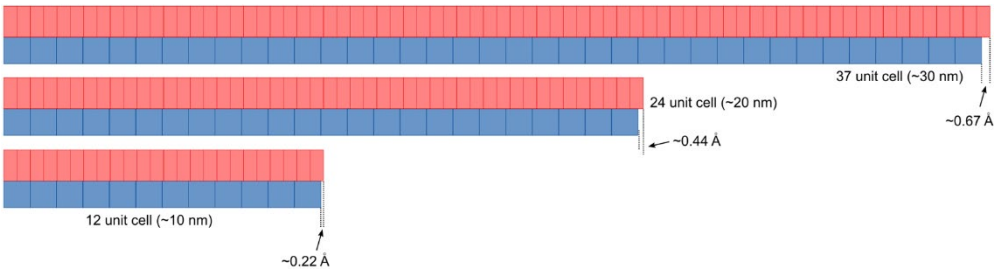

Figure 2.35. Illustration of unit cells suggesting the increase in epitaxial strain energy at the interface as the core size increases.

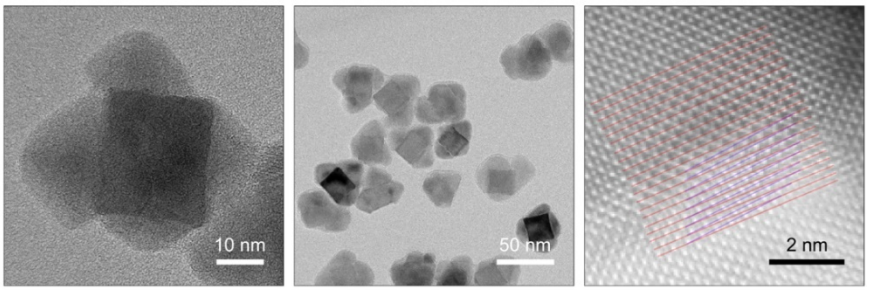

Figure 2.36. TEM images and HAADF-STEM image of Co_3O_4/Mn_3O_4 nanocrystals with 20 nm-sized cores. Epitaxial strain energy is much larger with the 20 nm-sized Co_3O_4 core than with 11 nm-sized one, preventing the GB formation and inducing screw dislocations at the Co_3O_4/Mn_3O_4 interface.

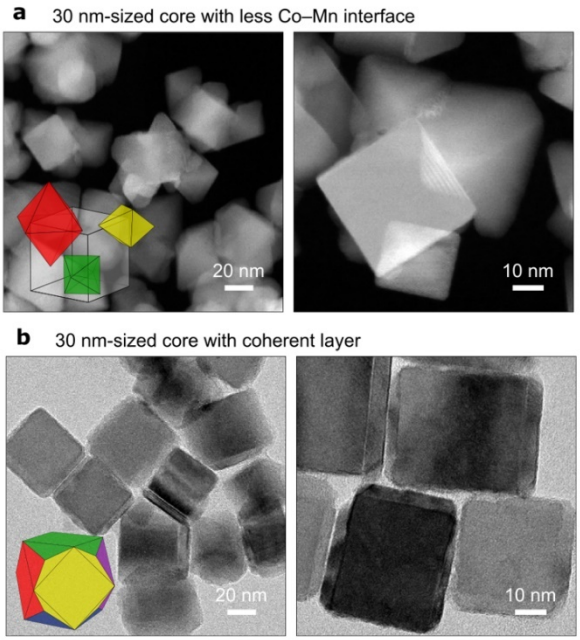

Figure 2.37. a-b, Control of GB formation when using large (30 nm-sized) Co_3O_4 cores with different surface ligands. The grains are more contiguous and have more GBs when using formate ligands (**b**) than when using chloride ligands (**a**).

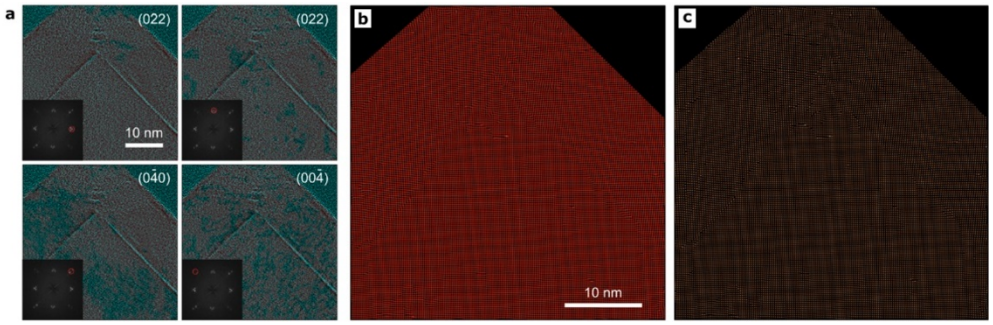

Figure 2.38. a-c, The geometric phase analysis (GPA)[30] of a Co_3O_4/Mn_3O_4 nanocrystal with a 30 nm-sized Co_3O_4 nanocube core as shown in Figure 2.14b. Bragg reflections and corresponding GPA lattice planes (**a**). Red circled Bragg reflections were selected as the reference peaks for the filtering. Red coloured GPA lattice planes in (**a**) show the distribution of dislocations. Bragg lattice mapping (**b**) and Bragg peak mapping (**c**) show the distribution of dislocations, especially zigzag-patterned dislocations, at the GB.

The Co_3O_4/Mn_3O_4 nanocrystals with islands (CoMn-CL+I) have a relatively large size distribution of grains in each nanocrystal. The number of the islands is reduced as the amount of $MnCl_2$ added to grow the grains decreases. Therefore, we prepared a set of CoMn-CL+I samples with different Mn contents and compared their XRD patterns to confirm the dependence of volume-averaged deformations on the number of islands (Figure 2.19). With decreasing the Mn content, the full width at half maximum (FWHM) of the (112) peak increases and the distance between the Mn_3O_4 (112) and (220) reflections decreases, which is in good agreement with the nonuniform rhombohedral distortion of the Mn_3O_4 unit cells localized at the GB region (~8 unit cells on the surface from the GB) (Figure 2.23). On the other hand, CoMn-CL samples with more Mn content are shown to have higher strain. Below the h_c, the shell is more strained as getting farther from the hetero-interface due to the gap closing, as confirmed by the strain tensor measurement (Figure 2.23).

2.3.9 Density functional theory (DFT) calculations

Computational Methods. Surface properties of Co_3O_4/Mn_3O_4 were calculated with a slab model which consists of 4 metal sites per surface, more than 8 metal oxide thickness and more than 15 Å vacuum. All the Mn layers at the surface and topmost Co interfacial three layers were allowed to relax below the maximum force threshold of 0.05 eV/Å within an energy cutoff of 550 eV and a gamma-point centred 3 × 3 × 1 *k*-point mesh. Surface energies for Co_3O_4/Mn_3O_4 slab were calculated from

$$E^{surface} = E[\text{Slab with } Co_xMn_yO_z] - x\mu Co - y\mu Mn - z\mu O / A$$

where $E(Co_3O_4) = \mu Co + 4\mu O$ and $E(Mn_3O_4) = 3\mu Mn + 4\mu O$, and A is surface area.

2.3.10 Extraction of the diamond lattice of Co_3O_4 {220} or Mn_3O_4 {112} planes in HAADF-STEM

(See Figure 2.39) We performed our quantitative image analysis as follows: from the original image (Panel a), we manually chose one random reference point (blue dot in Panel b), and its four neighbours (orange dots in Panel b). In addition, we marked a “foreground” mask to specify the region of interest (blue area in Panel c).

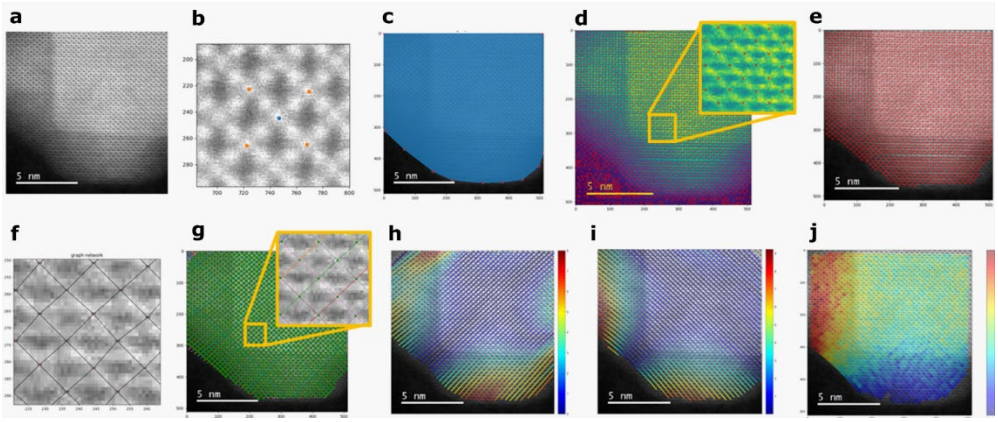

Figure 2.39. Procedure showing the quantitative image analysis of HAADF-STEM image.

We cropped a sub-patch, including the given four neighbours and used the sub-patch as an image template. When the image template is convolved with the original image, there is a firing response at each particle location. We extracted the local maxima responses (Panel d) and removed the ones outside the given "foreground" mask (Panel e).

These local maxima responses may still suffer from three types of errors: (1) extraneous particles (false positives), (2) missing particles (false negatives), and (3) correct particles but in slightly inaccurate locations (for example, the connected diagonal line segments in Panel f do not form smooth angles). The third issue may result from imaging quality, image resolution, and/or the fact that local maxima locations (x, y image coordinates) may need to be adjusted to sub-pixel level (i.e., from integer coordinates to fractional coordinates). To handle these issues, we conducted the following processes. Since we know the "representative" reference particle and its four neighbours from the manual selection, we can approximate the "representative" relative locations of the four neighbour particles to a candidate particle. We examine each candidate local maxima and check which other candidates can be its valid neighbours, where we assume that a valid neighbour candidate is the closest candidate to an approximated neighbour location, and the distance error (i.e., distance between the closest candidate and the approximated location) should be less than 5% of "representative" neighbouring distance (i.e., distance between

"representative" reference and its "representative" neighbour). This step allows us to identify true particles (resolving the first issue) and reconstructs the connectivities between the particles (Panel f). Using the lattice-like graph structure, we fit each diagonally connected group of particles of the graph with two-degree polynomials in the least square manner and then refined the position of each particle with regard to the intersection of these polynomial curves (Panel g). Using the intersections helps us not only in refining positions (resolving the third issue) but also in identifying missing particles (resolving the second issue). Panel g shows that the fitted diagonal line strips (curves) form smooth angles. Panels h and i show the diagonal curves in both directions separately. The colour represents the angle of the curves. The reference angle, set as dark blue, is the angle between the representative particle and its neighbours. From the graph, we calculated the aspect ratio of all diamond (lozenge) shapes. A perfect square shape has an aspect ratio of 1.0, and skinnier diamond shapes receive higher values. The distribution of the aspect ratios is illustrated in Panel j.

2.3.11 Strain tensor measurements for HAADF-STEM images

(See Figure 2.40) For each HAADF-STEM image, the image was first low pass filtered to simplify the geometry of each projected unit cell. Next, the centre position of each unit cell was measured by fitting the valleys with a two-dimensional Gaussian function with a negative peak height. Next each unit cell was given a unique lattice coordinate identifier (a,b), defined for the linear (unstrained) reference lattice defined by $r = r_0 + au + bv$, where r is the unit cell position, r_0 the origin in image coordinates, and u and v the lattice vectors also in image coordinates. r_0, u, and v were all measured from the central portion of the nanoparticle, the Co_3O_4 structure at least 4 unit cells away from the boundary with the Mn_3O_4 regions. By comparing the measured coordinates of each unit cell with those of the reference lattice, we computed the strain fields by numerical differentiation of the displacement field (measured unit cell positions minus reference positions). This was done with a Gaussian weighting kernel, averaging over an area defined by a Gaussian standard deviation of 1.5 unit cells of the reference lattice. This averaging reduces the high frequency noise created by numerical differentiation but limits the spatial resolution of the measurement to approximately 1.5 unit cells. Additionally, by using a reference lattice measured from each image, the linear drift of the sample with regard to the STEM probe due to thermal drift was removed from the measurement[25]. The strain maps are defined using the

normal infinitesimal strain conventions for strain along the x and y directions ε_{xx} and ε_{yy}, shear ε_{xy} and infinitesimal rotation θ. Finally, these strain maps were visualized by combining them with the original images - the image intensity was used for the value of each image, while the colouring was defined using the measured strains. Note that in STEM imaging, sample motion with respect to the STEM probe position can lead to drift artefacts, especially in the slow scan direction[25]. We have therefore measured the degree of drift in our experiments by performing orthogonal scan pair experiments, where the slow scan direction is rotated to 0 and 90 degrees (see Figure 2.40). The sample drift was measured and corrected using the method in ref. 25. These experiments showed negligible drift in all cases (relative to the degree of strain measured), and therefore we have opted to use single image measurements for the strain fields in order to minimize sample damage from the electron beam. Additionally, by using a reference lattice measured from each image, we remove and linear drift artefacts from the strain measurements[25].

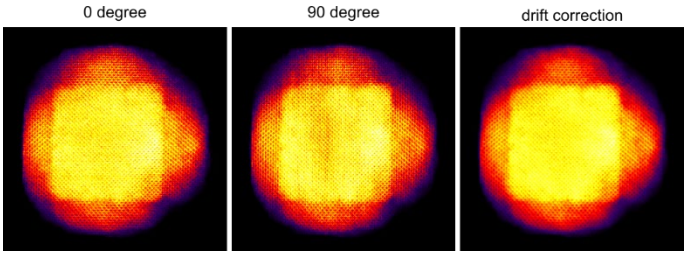

Figure 2.40. Drift correction of STEM image.

2.3.12 Geometric phase analysis (GPA) analysis

All strain and angle measurements were performed using a custom MATLAB code. For high resolution images with clear atomic resolution contrast, the angle measurements and strain fields were computed by fitting 2D Gaussian functions to all atomic column signals, and then measuring the deviation of the best-fit positions from a reference lattice. These displacement fields were interpolated into displacement maps, and then numerically differentiated to give the strain maps[29]. Plane angles were measured by fitting lines to sets of best-fit atomic positions. For lower resolution images where the atomic columns did not cover enough peak positions for accurate 2D Gaussian fitting, the geometric phase analysis (GPA) method was used to compute the strain fields, as described in ref. 30.

2.4 Conclusion

Thin films in 2D SK growth mode often exhibit periodic ripple patterns along with the island formation, which is mainly attributed to the epitaxial strain[9,31]. Pre-patterned substrates with ordered pit arrays and stripes are used for directing the island growth and ordering[32]. In our demonstration of the 3D analogy of the SK growth, each of the well-defined polyhedral nanocrystals (i.e., core) acts as a pre-patterned substrate. Consequently, a thin-film (i.e., shell) grows with a strain field patterned along the sharp edges due to the geometric misfit strain in addition to the epitaxial strain. This 3D network of strains also organizes the grains into a 3D superlattice[33]. Given that the self-organization of lattice domains in 2D epitaxial thin films has been a key element that brings various new physical phenomena, this utilization of geometric misfit strains in 3D shell growth also facilitates the possibility to further manipulate the properties of nanocrystalline materials for improved applications, such as in mechanics, catalysis, and dielectrics[34-37].

2.5 References

[1] Siegel, R. W. & Thomas, G. J. Grain boundaries in nanophase materials. *Ultramicroscopy* **40**, 376–384 (1992).

[2] Ovid'ko, I. A. Deformation of nanostructures. *Science* **295**, 2386 (2002).

[3] Read, W. T. & Shockley, W. Dislocation models of crystal grain boundaries. *Phys. Rev.* **78**, 275–289 (1950).

[4] Liu, H. H. *et al.* Three-dimensional orientation mapping in the transmission electron microscope. *Science* **332**, 833–834 (2011).

[5] Feng, B. *et al.* Atomic structures and oxygen dynamics of CeO_2 grain boundaries. *Sci. Rep.* **6**, 20288 (2016).

[6] Lu, K. Stabilizing nanostructures in metals using grain and twin boundary architectures. *Nat. Rev. Mater.* **1**, 16019 (2016).

[7] Klapper, H. & Rudolph, P. in *Handbook of Crystal Growth 2* 1093–1141 (Elsevier, 2015).

[8] Kwon, S. G. *et al*. Heterogeneous nucleation and shape transformation of multicomponent metallic nanostructures. *Nat. Mater.* **14**, 215–223 (2015).

[9] Dixit, G. K. & Ranganathan, M. Consequences of elastic anisotropy in patterned substrate heteroepitaxy. *Nanotechnology* **29**, 365305 (2018).

[10] Yang, B., Liu, F. & Lagally, M. G. Local strain-mediated chemical potential control of quantum dot self-organization in heteroepitaxy. *Phys. Rev. Lett.* **92**, 025502 (2004).

[11] Sun, S. & Zeng, H. Size-controlled synthesis of magnetite nanoparticles. *J. Am. Chem. Soc.* **124**, 8204–8205 (2002).

[12] Oh, M. H. *et al*. Galvanic replacement reactions in metal oxide nanocrystals. *Science* **340**, 964–968 (2013).

[13] Lim, B., *et al.* Synthesis of Pd−Au bimetallic nanocrystals via controlled overgrowth. *J. Am. Chem. Soc.* **132**, 2506–2507 (2010).

[14] Pan, A. *et al.* Insight into the ligand-mediated synthesis of colloidal $CsPbBr_3$ perovskite nanocrystals: The role of organic acid, base, and cesium precursors. *ACS Nano* **10**, 7943–7954 (2016).

[15] Tsivion, D., Schvartzman, M., Popovitz-Biro, R., von Huth, P. & Joselevich, E. Guided growth of millimeter-long horizontal nanowires with controlled orientations. *Science* **333**, 1003–1007 (2011).

[16] Johnson, C. L. et al. Effects of elastic anisotropy on strain distributions in decahedral gold nanoparticles. *Nat. Mater.* **7**, 120–124 (2008).

[17] Shklyaev, O. E., Beck, M. J., Asta, M., Miksis, M. J. & Voorhees, P. W. Role of strain-dependent surface energies in Ge/Si(100) island formation. *Phys. Rev. Lett*. **94**, 176102 (2005).

[18] Chen, G. et al. Formation of Ge nanoripples on vicinal Si (1110): From Stranski-Krastanow seeds to a perfectly faceted wetting layer. *Phys. Rev. Lett.* **108**, 055503 (2012).

[19] Sneed, B. T., Young, A. P. & Tsung, C.-K. Building up strain in colloidal metal nanoparticle catalysts. *Nanoscale* **7**, 12248–12265 (2015).

[20] Foster, C. M., Pompe, W., Daykin, A. C. & Speck, J. S. Relative coherency strain and phase transformation history in epitaxial ferroelectric thin films. *J. Appl. Phys.* **79**, 1405–1415 (1996).

[21] Sun, Y. *et al.* Ambient-stable tetragonal phase in silver nanostructures. *Nat. Commun.* **3**, 971–976 (2012).

[22] Romanov, A. E. & Kolesnikova, A. L. Application of disclination concept to solid structures. *Prog. Mater. Sci*. **54**, 740–769 (2009).

[23] Gránásy, L., Podmaniczky, F., Tóth, G. I., Tegze, G. & Pusztai, T. Heterogeneous nucleation of/on nanoparticles: A density functional study using the phase-field crystal model. *Chem. Soc. Rev.* **43**, 2159–2173 (2014).

[24] Gaillac, R., Pullumbi, P. & Coudert, F. X. ELATE: An open-source online application for analysis and visualization of elastic tensors. *J. Phys. Condens. Matter* **28**, 275201–275205 (2016). (URL: http://progs.coudert.name/elate/mp?query=mp-18759)

[25] Ophus, C., Ciston, J. & Nelson, C. T. Correcting nonlinear drift distortion of scanning probe and scanning transmission electron microscopies from image pairs with orthogonal scan directions. *Ultramicroscopy* **162**, 1–9 (2016).

[26] Huang, W., Yin, Y. & Li, X. Atomic-scale mapping of interface reconstructions in multiferroic heterostructures. *Appl. Phys. Rev.* **5**, 041110 (2018).

[27] MacLaren, I. & Ramasse, Q. M. Aberration-corrected scanning transmission electron microscopy for atomic-resolution studies of functional oxides. *Int. Mater. Rev.* **59**, 115–131 (2014).

[28] Bagués, N., *et al.* The misfit dislocation core phase in complex oxide heteroepitaxy. *Adv. Funct. Mater.* **28**, 1704437 (2018).

[29] Rasool, H. I., *et al.* Conserved atomic bonding sequences and strain organization of graphene grain boundaries. *Nano Lett.* **14**, 7057–7063 (2014).

[30] Hÿtch, M. J., Snoeck, E. & Kilaas, R. Quantitative measurement of displacement and strain fields from HREM micrographs. *Ultramicroscopy* **74**, 131–146 (1998).

[31] Hu, H., Gao, H. J. & Liu, F. Theory of directed nucleation of strained islands on patterned substrates. *Phys. Rev. Lett.* **101**, 216102 (2008).

[32] Zhong, Z. & Bauer, G. Site-controlled and size-homogeneous Ge islands on prepatterned Si (001) substrates. *Appl. Phys. Lett.* **84**, 1922–1924 (2004).

[33] Damodaran, A. R., *et al.* New modalities of strain-control of ferroelectric thin films. *J. Phys.: Condens. Matter* **28**, 263001 (2016).

[34] Li, X., Wei, Y., Lu, L., Lu, K. & Gao, H. Dislocation nucleation governed softening and maximum strength in nano-twinned metals. *Nature* **464**, 877–880 (2010).

[35] Mariano, R. G., Mckelvey, K., White, H. S. & Kanan, M. W. Selective increase in CO_2 electroreduction activity at grain-boundary surface terminations. *Science* **358**, 1187–1192 (2017).

[36] Fan, F., *et al.* Continuous-wave lasing in colloidal quantum dot solids enabled by facet-selective epitaxy. *Nature* **544**, 75–79 (2017).

[37] Gao, P., *et al.* Atomic-scale mechanisms of ferroelastic domain-wall-mediated ferroelectric switching. *Nat. Commun.* **4**, 2791 (2013).

Chapter 3 Epitaxially Strained CeO_2/Mn_3O_4 Nanocrystals as an Enhanced Antioxidant for Radioprotection

3.1 Introduction

The increasing use of ionizing radiation in medicine and industry has raised the risk of accidental total body irradiation (TBI), which can result in life-threatening consequences such as acute radiation syndrome (ARS).[1] Depending on the radiation exposure dose, ARS is categorized into hematopoietic (H-ARS, 1.5-4Gy), gastrointestinal (GI-ARS, 6-15Gy), and neurovascular syndromes (NV-ARS, 15Gy), all of which involve the rapid generation of ROS in the tissues within a millisecond via the radiolysis of water, causing both acute and chronic oxidative damages to the cells and organs.[2] Although Amifostine (Ethyol®) was developed as a radioprotectant,[3] its application is only approved for the protection of salivary glands, because its short elimination half-life and limited ROS-scavenging capacity require a high dose, which may cause systemic toxicity and complications, to be used under TBI conditions.[4] In this light, long-lasting radioprotectants with improved ROS-scavenging activities are highly desired.

In recent years, catalytic nanomaterials with antioxidant properties such as cerium oxide,[5] manganese oxide[6] and vanadium oxide[7] (collectively known as nanozymes)[8] have gained increasing attention for their ability to treat ROS-related diseases.[9] In particular, CeO_2 nanoparticles have been used as efficient antioxidants because their ability to cycle between Ce^{3+} and Ce^{4+} ionic states allows them to catalytically remove various ROS such as superoxide (O_2^-), hydrogen peroxide (H_2O_2), and hydroxyl radical ($^{\bullet}OH$).[10] However, the potential side effects of inorganic nanomaterials remain a critical issue,[11] leading to the necessity of decreasing their administration while maintaining the therapeutic efficacy. One possible way is enhancing the catalytic reactivity of nanomaterials through ligand and strain effects.[12] Notably, tuning the oxygen binding energy by modifying the surface strains of metallic core-shell nanomaterials has been shown to effectively enhance their catalytic activities.[13] Such strain effects have rarely been demonstrated for inorganic nanozymes that scavenge ROS. We hypothesize that it is possible to lower the required doses of nanozyme-based therapeutic agents by imposing surface strains and improving their catalytic performance.

3.2 Experimental Section

3.2.1 Synthesis of CeO_2 nanocrystals

A mixture of 0.43 g of cerium (III) nitrate (Acros), 2.7 g of oleylamine (Acros), and 0.03 g of oleic acid (Aldrich) in 15 mL of 1-dodecanol (Aldrich) was heated to 120 °C under air. The solution was aged for several minutes until it changed to yellow. During the heating process, 0.3 mL of distilled water was added at ~90 °C. After the reaction, an excess amount of acetone, ethanol, and acetonitrile was added to purify the ceria nanocrystals. The nanocrystals were collected by centrifugation.

3.2.2 Synthesis of CeO_2/Mn_3O_4 nanocrystals

A mixture of as-synthesized CeO_2 nanocrystals (0.09 g), 1.34 g of oleylamine (Acros), 0.14 g of oleic acid (Aldrich), 0.26 mL of hydrochloric acid (Aldrich), and 15 mL of xylene (Aldrich) was heated to 90 °C. Then, 0.8 mL aqueous solution of 0.13 M ('Mn thin') and 0.4-0.6 M ('CeO_2/Mn_3O_4') manganese (II) chloride was rapidly injected into the solution. After 2 hr aging, the solution was cooled down to room temperature, and the CeO_2/Mn_3O_4 nanocrystals were washed with hexane and ethanol, and retrieved by centrifugation. The as-prepared heterostructured CeO_2/Mn_3O_4 nanocrystals were well dispersed in chloroform. The relative Mn concentrations of the samples were estimated using inductively coupled plasma-atomic emission

spectroscopy (ICP-AES). The samples with Mn contents (Mn/Ce mol%) of less than 15% and around 30% were designated as 'Mn thin' and 'CeO_2/Mn_3O_4', respectively.

3.2.3 Structural and chemical analysis

The TEM and the energy-filtered TEM images were obtained using a JEOL JEM-2100F. HAADF-STEM images were obtained using a JEOL JEM-ARM200F in the National Center for Inter-university Research Facilities, Seoul National University. XRD patterns were obtained using a Rigaku D/max 2500 diffractometer with Cu Kα radiation in Seoul National University. Inductively coupled plasma-atomic emission spectroscopy (ICP-AES) (Shimadzu) was used for elemental analysis to extract the compositional (Mn-to-Ce ratio) information. XAS experiments were carried out at BL2A beamline in PLS-II. Raman and XPS spectra were obtained using a HORIBA LabRAM HV Evolution and a KRATOS AXIS-HSi, respectively, in Research Institute of Advanced Materials, Seoul National University. We chose the O 1s XPS self-consistent peak fitting model which agrees with the UV Raman results.

3.2.4 Electrochemical and Temperature-programmed reduction measurements

Before conducting the electrochemical measurements, the ligands on the nanocrystal surface were exchanged using nitrosonium tetrafluoroborate

($NOBF_4$). 0.01 g of $NOBF_4$ and 0.4 mL of dimethylformamide (DMF) was mixed in Ar atmosphere. The solution was added into the 10 mL THF solution containing the as-prepared nanocrystals. Then, the nanocrystals were collected by adding hexane. Electrochemical reductions of hydrogen peroxide and oxygen were measured at 293 K using a three-electrode system with an Autolab 302 potentiostat. For the working electrode, the nanocrystals dispersed in the solution were drop-casted on glassy carbon (diameter of 3 mm) with a loading density of 0.2 mg/cm^2. A graphite rod and a saturated calomel electrode (SCE) were used as a counter and a reference electrode, respectively. For electrochemical reduction reaction, the nanocrystals were polarized between 0 and -0.8 V (vs. SCE) at a scan rate of 50 mV/s in Ar-saturated 5 mM H_2O_2 PBS solution (pH 7.4) or in O_2-saturated PBS solution (pH 7.4). Temperature-programmed reduction (TPR) analysis was performed using a thermal conductivity detector-equipped gas chromatograph (Younglin Instruments, Co., Korea) with an injection of H_2–N_2 gas and a heating rate of 5 °C/min.

3.2.5. Synthesis of phospholipid-polyethylene glycol-capped nanocrystals

Mn_3O_4 nanocrystals were purchased from US Research Nanomaterial, Inc. (Houston, TX). A total of 50 mg of Mn_3O_4 powder was dispersed in ethanol and ultrasonicated (750W, 20 kHz) for 6 hrs. The resultant Mn_3O_4 nanocrystals were redispersed in 10 ml of DMF and treated with 0.1 M

$NOBF_4$ followed by 20 mg of oleylamine. The Mn_3O_4 nanocrystals were purified with ethanol and redispersed in chloroform.

Phospholipid-polyethylene glycol (PEG) was encapsulated on surface of CeO_2/Mn_3O_4, CeO_2 or Mn_3O_4 nanocrystals to form water dispersible nanocrystals. First, 3 ml of the nanocrystals in chloroform (10 mg/ml) was mixed with 10 ml of 1,2-distearoyl-*sn*-glycero-3-phosphoethanolamine-N-[methoxy(polyethylene glycol)-2000] (mPEG(2000)-PE, Avanti Polar Lipids Inc., Alabaster, Alabama, USA) in chloroform (10 mg/ml) and sonicated for 5 min. Chloroform was then removed by a rotary evaporator, and further dried completely in vacuum oven at 70 °C for 2 hrs. Next, 3 ml of deionized water was added to the sample and sonicated to obtain a transparent colloidal suspension. The excess mPEG(2000)-PE was removed using ultracentrifugation and the CeO_2/Mn_3O_4 nanocrystals were filtered using 0.4 μm filter. Finally, the nanocrystals were dispersed in PBS solution for the further applications.

3.2.6. Cell viability test

HeLa cells were seeded in the 96-well plate with 10,000 cells per well and cultured for 24 hrs. Subsequently, CeO_2/Mn_3O_4 nanocrystals were treated with various concentrations and incubated for another 24 hrs. 20 μl (5 mg/ml) 3-[4,5-dimethylthialzol-2-yl]-2,5-diphenyltetrazolium bromide (MTT) was added to each well and incubated at 37 °C for 4 hrs. Finally, the medium is

removed and 200 µl dimethylsulfoxide is added to each well. The absorbance was measured at 540 nm using a 96-well plate reader (Victor X4, Perkin-Elmer, USA).

3.2.7. Superoxide Dismutase (SOD) and catalase activity assays

The superoxide-scavenging activity was performed using a SOD assay kit (Sigma-Aldrich). The water dispersible nanocrystals of CeO_2/Mn_3O_4, CeO_2, Mn_3O_4 were diluted in 200 µl WST-1 (water-soluble tetrazolium salt; (2-(4-iodophenyl)-3-(4-nitrophenyl)-5-(2,4-disulfo-phenyl)-2H-tetrazolium, monosodium salt) solution in triplicate. SOD coupling reaction was initiated by adding 20 µl of xanthine oxidase solution and incubating the solution in a cell incubator for 20 min. The SOD-mimetic activity was examined by measuring absorbance at 450 nm using a microplate reader (Victor X4, Perkin-Elmer, Waltham, MA, USA). For pH-dependent analysis, the assay was carried out using the same protocol, but the pH of the buffer solution was adjusted using diluted hydrochloric acid and a pH meter. Catalase-mimetic activity assay (CELL BIOLABS INC.) was used to assess the catalase activity of the nanocrystals. A total of 25 µl of CeO_2/Mn_3O_4, CeO_2, and Mn_3O_4 nanocrystals were added into separate wells of a 96-well microplate in triplicate. To each microplate well, 25 µl of 40 µM hydrogen peroxide working solution was added, mixed thoroughly and incubated at room temperature for 30 mins. Next, 50 µl of the ADHP/HRP Working solution was added to each

well and incubated in a cell incubator for another 30 mins. The catalytic activity of the nanocrystals was examined by measuring the fluorescence using an excitation range of 530-560 nm and emission range of 590-600 nm.

3.3 Result and Discussion

We provide the proof of concept of the hypothesis by using CeO_2/Mn_3O_4 nanocrystals as a model system (Figure 3.1). Manganese ions deposited on the surface of CeO_2 nanocrystals form islands of strained Mn_3O_4 layers and increase the numbers of oxygen vacancies in the CeO_2 phase. We demonstrate that these effects facilitate the redox reactions at the Mn_3O_4 and CeO_2 surfaces, enhancing the catalytic antioxidant activities. A mouse model study also revealed that a systemic delivery of a low dose of the nanocrystals can effectively protect the tissues from total body irradiation (TBI).

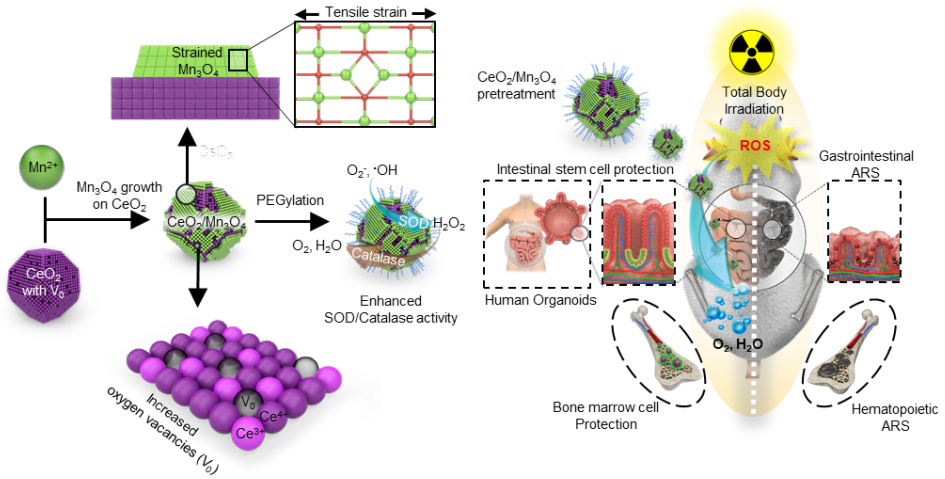

Figure 3.1. Schematic illustration of highly catalytic CeO_2/Mn_3O_4 nanocrystals preventing acute radiation syndrome.

Heterostructured CeO_2/Mn_3O_4 nanocrystals were prepared by a seed-mediated growth process.[14] The seeds, 4 nm-sized truncated octahedral CeO_2 nanocrystals, predominantly enclosed by {100} and {111} (Figure 3.2), were reacted with $MnCl_2$ to yield the CeO_2/Mn_3O_4 nanocrystals (Figure 3.3 and Figure 3.4). High-angle annular dark-field scanning transmission electron microscopy (HAADF-STEM) images and the corresponding fast Fourier transform (FFT) image show that the core is well preserved after the heterogeneous precipitation of manganese oxide on the surface (Figure 3.3). X-ray diffraction (XRD) analysis reveals that the CeO_2 nanocrystals have the cubic fluorite structure (JCPDS #34-0394) with an estimated (111) spacing of 3.14 Å (Figure 3.5). Crystallographic orientation between the CeO_2 core and Mn_3O_4 islands is illustrated in Figure 3.6 based on the *d*-spacings measured from the HAADF-STEM images. Given the lattice parameters of bulk CeO_2 {200} and Mn_3O_4 {004} (2.71 and 2.36 Å, respectively), the estimated lattice mismatch is ~13%. Because of this large mismatch, Mn_3O_4 islands experience a tensile strain to have expanded Mn_3O_4 {004} lattice (~2.55 Å). As the islands grow vertically, the highly strained Mn_3O_4 lattice gradually relaxes near the surface, as exemplified by those two nonparallel Mn_3O_4 {004} with the lattice angle difference of ~7° (Figure 3.6). This is further supported by the visible Raman characterization, which shows the peaks for the first-order F_{2g} symmetry mode of CeO_2 at 452 cm^{-1} and the A_{1g} symmetric stretching of Mn–

O bond in Mn_3O_4 at 645 cm^{-1} (Figure 3.7). Asymmetric broadening of the F_{2g} and A_{1g} peaks indicate the presence of defects and structural distortions induced by the heteroepitaxial strain.

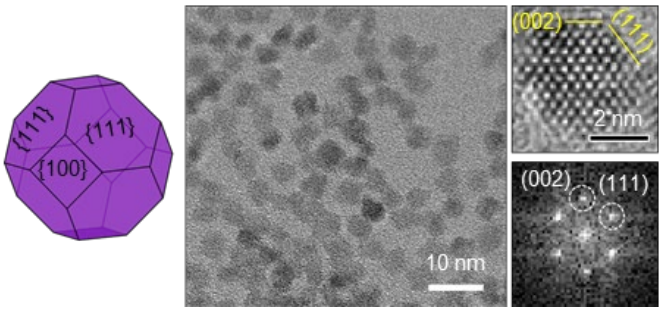

Figure 3.2. Morphology of CeO_2 nanocrystals. Three-dimensional illustration (left), TEM images (middle and top right), and the corresponding FFT pattern (bottom right) of CeO_2 nanocrystals.

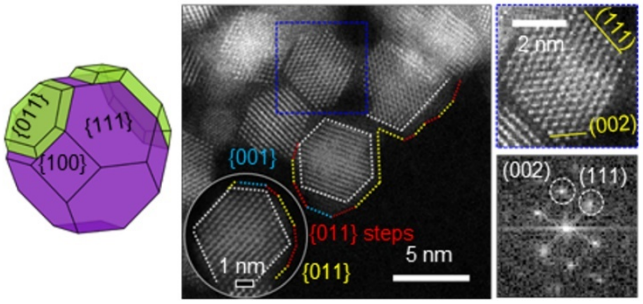

Figure 3.3. Morphology of CeO_2/Mn_3O_4 nanocrystals. Three-dimensional illustration (left), STEM images (middle and top right), and the corresponding FFT pattern (bottom right) of CeO_2/Mn_3O_4 nanocrystals.

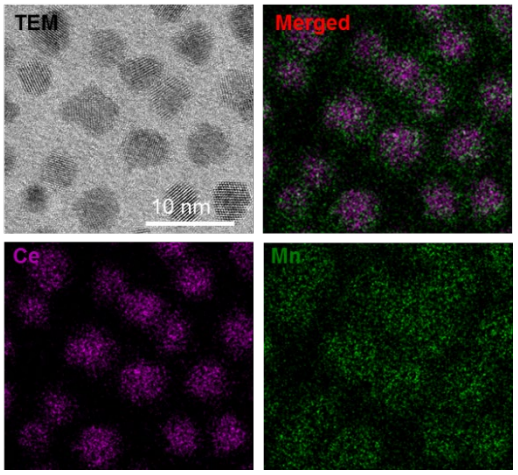

Figure 3.4. Elemental map images by energy-filtered TEM. TEM image of CeO_2/Mn_3O_4 nanocrystal and corresponding Ce M (purple), Mn L (green), and merged images show that Mn oxides were deposited onto the CeO_2 nanocrystals.

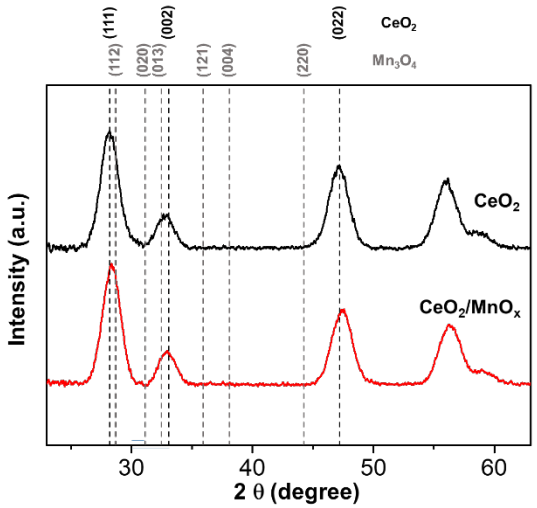

Figure 3.5. XRD patterns of CeO_2 and CeO_2/Mn_3O_4. XRD patterns reveal that the Mn_3O_4 shells were epitaxially grown on CeO_2 nanocrystals. The absence of Mn_3O_4 reference peaks (JCPDS #80-0382) means that monometallic Mn_3O_4 nanocrystals were not separately formed and the epitaxially grown Mn_3O_4 were only a few layers, not detectable in XRD.

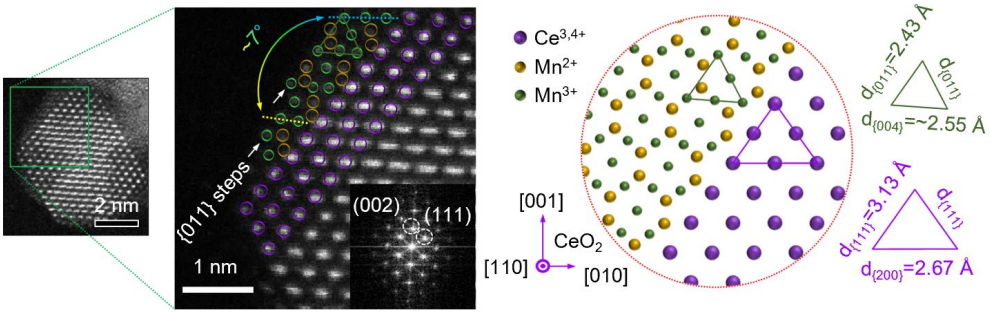

Figure 3.6. Atomic-resolution STEM images and 2D illustration showing the lattice strain in Mn_3O_4 layers.

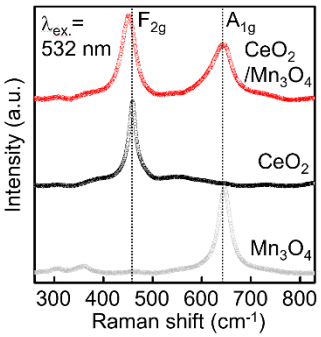

Figure 3.7. Visible Raman spectra of CeO_2/Mn_3O_4 nanocrystals.

When less than 15 mol% of Mn is deposited onto the CeO_2 nanocrystals, the oxidation state of Mn is mostly Mn^{2+} ('Mn thin' in Figure 3.8 and Figure 3.9). The reason Mn^{2+} motif deposits before the Mn^{3+} motif might be because the ionic radius of Mn^{2+} is more compatible with Ce^{4+}.[15] TEM images and the corresponding FFT patterns in Figures 3.6 and the visible Raman spectra in Figure 3.7 demonstrate that the manganese oxide phase deposited on CeO_2 was the Mn_3O_4 phase. The transition in oxidation state from the thin layer to the thick layer is likely due to the energetically stable Mn^{2+} stacking motif of the {011} planes that form the Ce-Mn interface. Because the ionic radius of Mn^{2+} is more compatible with Ce ions, the Mn^{2+} motif deposits first on the CeO_2 surface layer. Thereafter, Mn_3O_4 phase grows on the Mn^{2+} layer as shown previously. However, as more Mn is deposited, both Mn^{2+} and Mn^{3+} are observed ('CeO_2/Mn_3O_4' in Figure 3.8). The lower intensity ratio of the Mn L_3- to L_2-edge ($I(L_3/L_2)$) absorption indicates the higher oxidation state of the Mn ions in CeO_2/Mn_3O_4. Interestingly, the Mn^{2+} peak is less pronounced than that of the previously reported bulk Mn_3O_4,[16] which means that the strained Mn_3O_4 layers have slightly higher oxidation state than monometallic Mn_3O_4 nanocrystals. X-ray photoelectron spectroscopy (XPS) and X-ray absorption spectra (XAS) analyses jointly reveal that the Ce^{4+} ions in the CeO_2 nanocrystals and the deposited Mn^{2+} ions form a polar Ce^{4+}–O–Mn^{2+} interface (Figure 3.10 and Figure 3.11). These data suggest that CeO_2/Mn_3O_4

nanocrystals are composed of CeO_2 core, Ce^{4+}–O–Mn^{2+} heterointerface, and highly strained Mn_3O_4 islands.

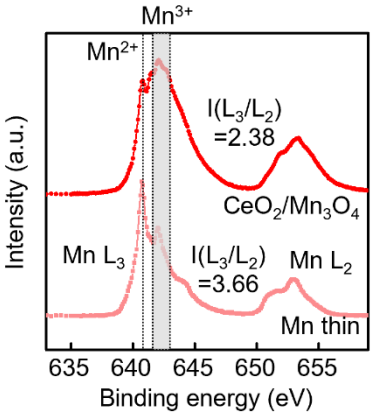

Figure 3.8. Mn $L_{2,3}$-edge XAS data of thin and optimized Mn oxide layer.

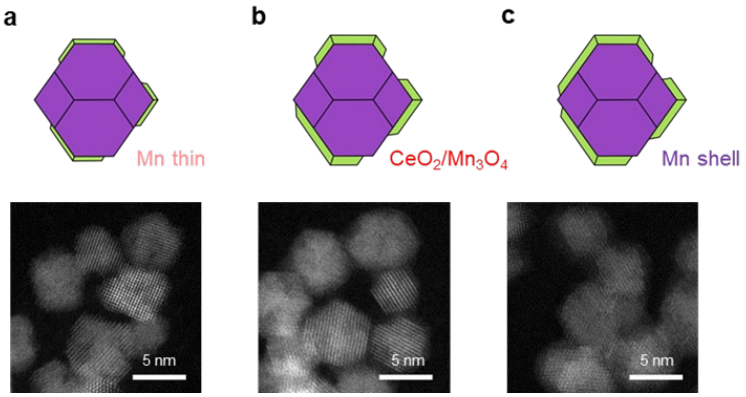

Figure 3.9. Schematic illustrations and the corresponding STEM images of various heterostructured CeO_2/Mn_3O_4 nanocrystals. a) 'Mn thin' nanocrystal is the CeO_2/Mn_3O_4 nanocrystal with thin layer of Mn oxide. b) 'CeO_2/Mn_3O_4' nanocrystal is the sample with optimized Mn amount in the Mn_3O_4 layer. c) 'Mn shell' nanocrystal is the CeO_2/Mn_3O_4 nanocrystal with the Mn_3O_4 layer that encloses most of the CeO_2 surface.

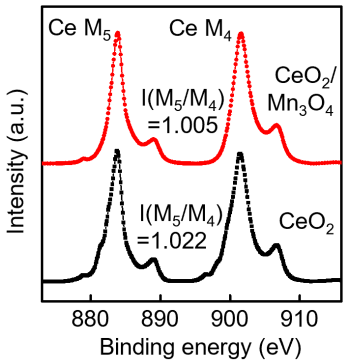

Figure 3.10. Ce $M_{4,5}$-edge XAS analysis of CeO_2/Mn_3O_4 nanocrystals.

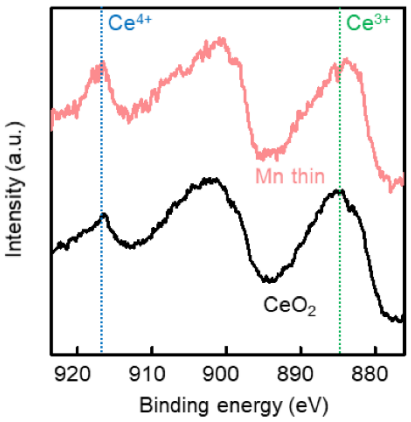

Figure 3.11. Ce 3d XPS analysis for characterization of the interface of CeO_2 and Mn oxide with thin layer of Mn oxide. The as-synthesized CeO_2 nanocrystals were slightly oxidized after the reaction with Mn^{2+}, evidenced by XPS.

The surface defect states of CeO_2 and CeO_2/Mn_3O_4 nanocrystals were compared using UV Raman spectroscopy (Figure 3.12). The intensity ratio of the defect-induced (D mode) peak at 598 cm^{-1} to F_{2g} peak at 452 cm^{-1} (I_D/I_{F2g}) increases after the Mn_3O_4 deposition, indicating that the number of oxygen vacancies increases on the surface of the CeO_2 nanocrystals. Such nanocrystals with abundant oxygen vacancies are expected to have improved ROS scavenging activities.[17] O 1s XPS spectra further verifies the defective oxide surface (Figure 3.13). The higher ratio of oxygen defects to lattice oxygen in CeO_2/Mn_3O_4 nanocrystals (0.85) compared to CeO_2 nanocrystals (0.60) results from the higher oxygen vacancy level, which agrees with the UV Raman results.

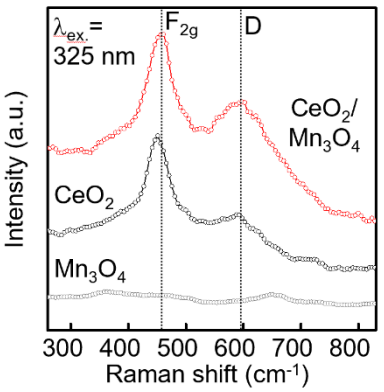

Figure 3.12. UV Raman spectra of CeO_2/Mn_3O_4, CeO_2, and Mn_3O_4 nanocrystals.

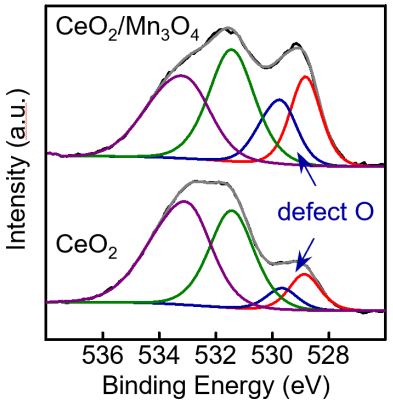

Figure 3.13. O 1s XPS spectra with binding energies assigned to lattice oxygen (~529 eV, red), oxygen defects (~530 eV, blue), surface adsorbed oxygen (~531 eV, green) and surface oxygen (~533 eV, purple).

Though the primary comparison is between CeO_2 and CeO_2/Mn_3O_4 nanocrystals, monometallic Mn_3O_4 nanocrystals are added to the comparison set as a reference sample (Figure 3.14). The comparison demonstrates the enhanced antioxidant effects of CeO_2/Mn_3O_4 nanocrystals originated from epitaxially strained Mn_3O_4 layers and not from the presence of Mn_3O_4 itself. To evaluate the surface reducibility of the nanocrystals, we performed temperature-programmed reduction (TPR) experiments with H_2 (Figure 3.15). Compared with the oxygen reduction peaks for CeO_2 (507 ^oC) and Mn_3O_4 (498 ^oC) nanocrystals, the peak for CeO_2/Mn_3O_4 nanocrystals is significantly shifted to a lower temperature (382 ^oC), indicating an enhanced surface reducibility.

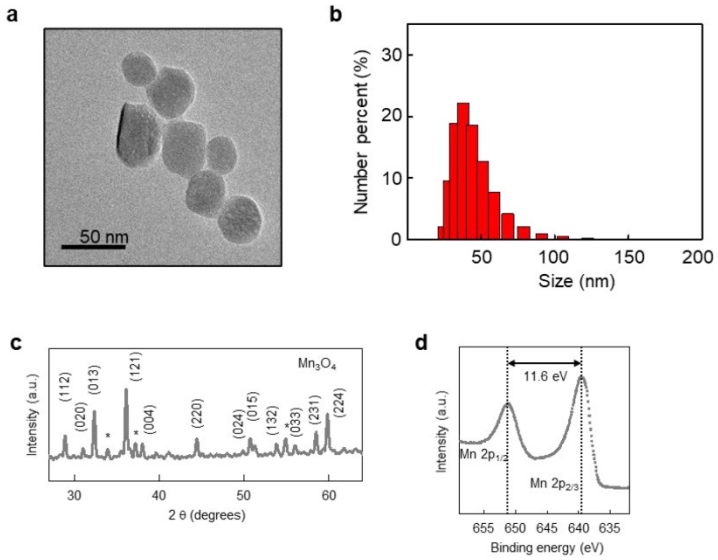

Figure 3.14. Characterization of Mn_3O_4 nanocrystal. a) TEM image of Mn_3O_4 nanocrystals. b) Hydrodynamic diameter of Mn_3O_4 nanocrystals in water is around 42 nm. c) XRD pattern of Mn_3O_4 nanocrystals shows that the manganese oxide phase is Mn_3O_4 spinel structure (JCPDS #24-0734). Asterisks indicate the peaks from Si and SiC. d) Mn 2p XPS analysis for Mn_3O_4 reference sample. The two peaks separated by about 11.6 eV is in good agreement with the characteristics of bulk Mn_3O_4.

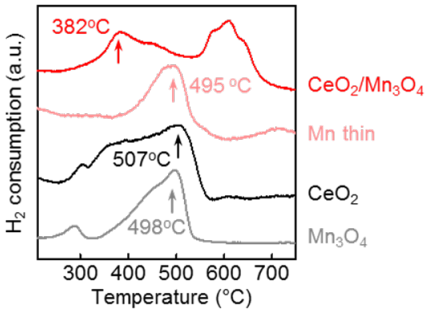

Figure 3.15. H_2-Temperature programmed reduction curves for CeO_2, Mn_3O_4, Mn thin and CeO_2/Mn_3O_4 nanocrystal. The surface oxygen reduction peak at 507 ºC for CeO_2 moved to a lower temperature in Mn thin sample (495 ºC), while the peak moved to far lower temperature (382 ºC), in CeO_2/Mn_3O_4 sample.

The abilities of each type of nanocrystal and the reference samples to eliminate ROS was further evaluated by measuring electrocatalytic reduction of H_2O_2 and oxygen. Linear-sweep voltammetry (LSV) was performed with the nanocrystals supported on glassy carbon electrode either in Ar-saturated phosphate-buffered saline (PBS, 0.01 M) containing 5 mM H_2O_2 or in O_2-saturated PBS (Figure 3.16). The measured catalytic activities were compared in terms of onset potential (measured at -0.15 mA cm^{-2}) and current density (measured at -0.25 V) (Figure 3.17). The larger onset potential and current density values observed for CeO_2/Mn_3O_4 nanocrystals clearly demonstrate their higher catalytic reduction activities than those of CeO_2 or Mn_3O_4 nanocrystals. Moreover, the CeO_2/Mn_3O_4 nanocrystals with the Mn_3O_4 islands exhibit a higher activity than those with thinner Mn_3O_4 layer or with Mn_3O_4 shell that covers most of the CeO_2 surface (Figure 3.18). The sample with higher atomic ratio of Mn to Ce, named as 'Mn shell', has more amount of Mn oxide at the surfaces, which means Mn_3O_4 shell mostly covering CeO_2 and surface of CeO_2 is less exposed (see also Figure 3.9). The surface coverage is roughly estimated based on the atomic ratio of Mn to Ce from the XPS data. The orders of onset potential at -0.15 mA cm^{-2} are CeO_2/Mn_3O_4 > Mn shell > Mn thin for both H_2O_2 reduction and O_2 reduction. As the Mn_3O_4 islands cover the CeO_2 surface above the certain amount of Mn_3O_4, the activity decreases.

This indicates that the enhanced activity originates from the synergistic effect by the exposed CeO_2 surface and the highly strained Mn_3O_4 islands.

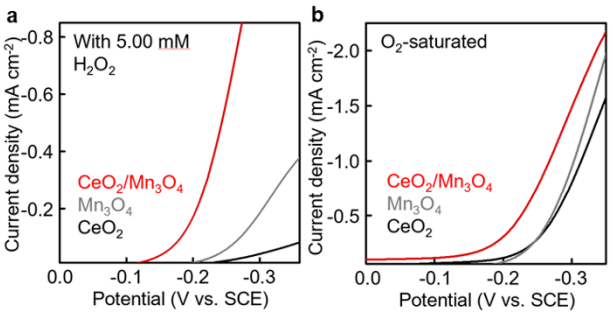

Figure 3.16. LSV curves for H_2O_2 reduction in Ar-saturated PBS (a) or oxygen reduction in O_2-saturated PBS (b).

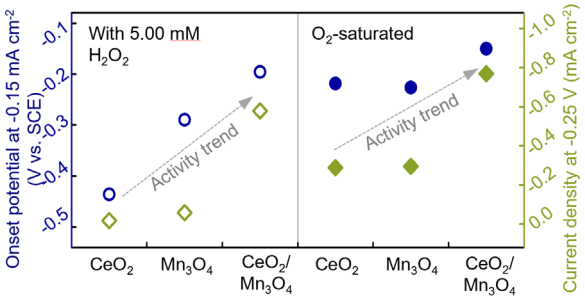

Figure 3.17. H_2O_2 and oxygen reduction activities in terms of onset potential and current density.

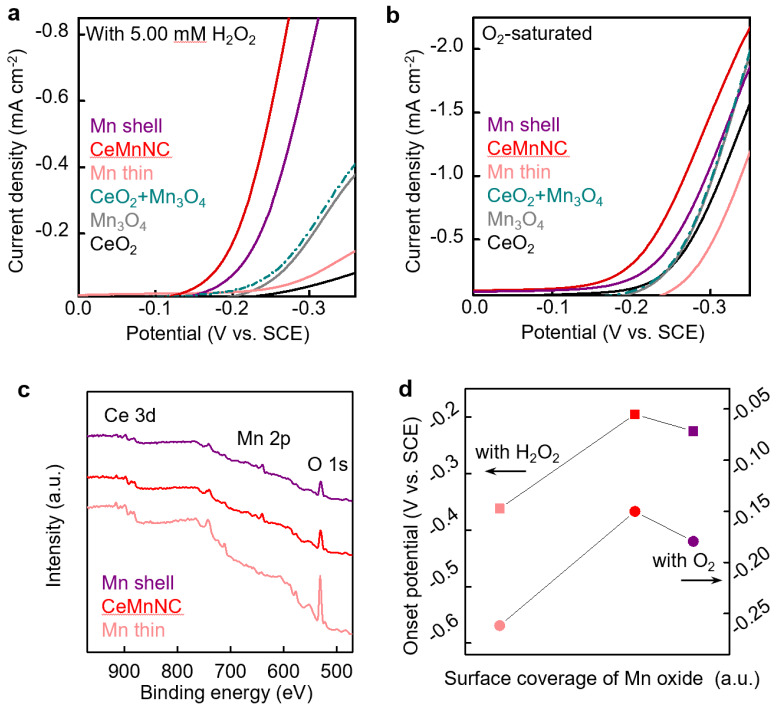

Figure 3.18. Electrocatalytic properties and characterization of CeO_2, Mn_3O_4 and various types of CeO_2/Mn_3O_4 nanocrystals. a-b) Linear-sweep voltammetry curves at a scan rate of 50 mV s^{-1} for H_2O_2 reduction (a) and oxygen reduction (b) in Ar-saturated and O_2-saturated PBS solution (pH=7.4), respectively. CeO_2+Mn_3O_4 is denoted as physically mixing CeO_2 nanocrystals and Mn_3O_4 nanocrystals. c) XPS survey spectra of the Mn thin, CeO_2/Mn_3O_4, and Mn shell samples. d) Onset potentials as a function of the surface coverage of Mn oxide (a.u.).

In addition to the original electrocatalytic tests, we also conducted SOD and catalase mimetic assays to demonstrate the ROS scavenging activities of Mn_3O_4 nanocrystals in a water-soluble biological environment. The as-synthesized hydrophobic CeO_2/Mn_3O_4 nanocrystals were transferred into PBS using the PEGylation method[18] (Figure 3.19a), and the PEGylated nanocrystals showed an average hydrodynamic diameter of ~10 nm (Figure 3.19b). The synthesized CeO_2/Mn_3O_4 nanocrystals in aqueous solution showed no significant cellular toxicity up to 176 μM (Figure 3.20). The SOD- and catalase-mimetic assays showed similar ROS-scavenging trends to electrocatalytic tests (Figure 3.21). These assays showed that Mn_3O_4 nanocrystals exhibited similar catalytic trends as antioxidant Mn_3O_4 nanozyme particles reported previously[18].

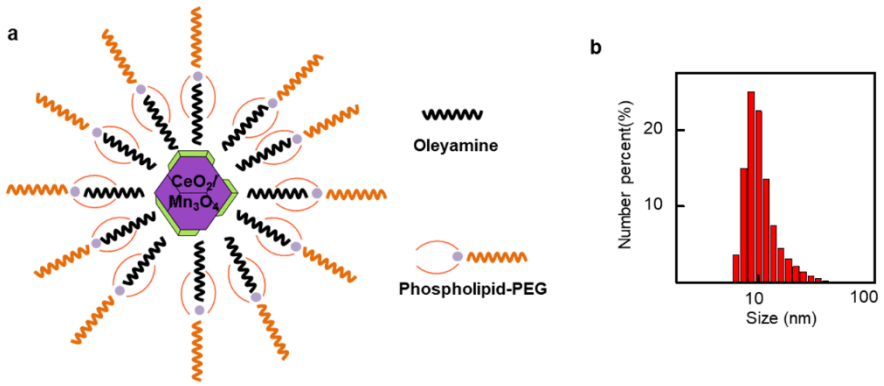

Figure 3.19. Illustration and characterization of PEGylated CeO_2/Mn_3O_4 nanocrystals. a) Illustration of the structure of PEGylated CeO_2/Mn_3O_4 nanocrystals. b) Hydrodynamic diameter of CeO_2/Mn_3O_4 nanocrystals in water.

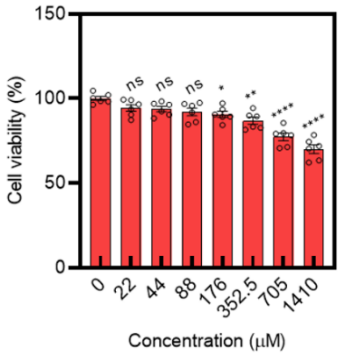

Figure 3.20. Cytotoxicity test results of PEGylated CeO_2/Mn_3O_4 nanocrystals for HeLa cells show no significant toxicity up to 176 μM (n = 6). Data are expressed as average ± s.e.m. One-way ANOVA is performed with Tukey's multiple comparison tests. Significance is set at *P < 0.05, **P < 0.01, ***P < 0.001, ****P < 0.0001 versus 0 μM; ns, not statistically significant.

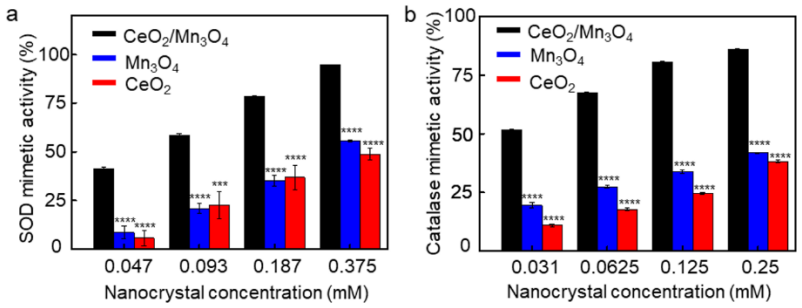

Figure 3.21. Antioxidant activity assays. a) SOD-mimetic activity assay, b) catalase-mimetic assay of the nanocrystals of CeO_2/Mn_3O_4, CeO_2 and Mn_3O_4 show that CeO_2/Mn_3O_4 nanocrystals have better antioxidant activity than that of CeO_2 or Mn_3O_4 nanocrystals.

3.4 Conclusion

In summary, our results show that the antioxidant activity of heterostructured CeO_2/Mn_3O_4 nanocrystals is powerful enough to protect the hematopoietic intestinal stem cells from irradiation-induced ROS damage. Manganese ions deposited on the surface of CeO_2 nanocrystals form the islands of epitaxially strained Mn_3O_4 layers, generating abundant oxygen vacancies in the CeO_2 phase. The increased number of oxygen vacancies effectively improved the oxygen adsorption efficiency on the nanocrystal surface, allowing the nanocrystals to scavenge ROS more efficiently. We show that only a small dose of the CeO_2/Mn_3O_4 nanocrystals is required to protect the ICSs from the irradiation-induced ROS damage using a hIO model and mRNA sequencing. In a mouse model, a small dose of the CeO_2/Mn_3O_4 nanocrystals can effectively improve the survival rate after TBI. Our results demonstrate that the surface strain tuning of CeO_2 nanocrystals can enhance their antioxidant properties, making them highly effective radio-protectants for preventing ARS induced by TBI.

3.5 References

[1] J. Xie, C. Wang, F. Zhao, Z. Gu, Y. Zhao, *Adv. Healthc. Mater*. **2018**, 7, 1800421.

[2] K. R. Brown, E. Rzucidlo, *J. Vasc. Surg*. **2011**, 53, 15S.

[3] J. R. Kouvaris, V. E. Kouloulias, L. J. Vlahos, *Oncologist* **2007**, 12, 738.

[4] V. K. Singh, T. M. Seed, *Expert Opin. Drug Saf*. **2019**, 18, 1077.

[5] a) Q. Bao, P. Hu, Y. Xu, T. Cheng, C. Wei, L. Pan, J. Shi, *ACS Nano* **2018**, 12, 6794; b) K. Korschelt, M. N. Tahir, W. Tremel, *Chem. Eur. J*. **2018**, 24, 9703; c) D. Jiang, D. Ni, Z. T. Rosenkrans, P. Huang, X. Yan, W. Cai, *Chem. Soc. Rev*. **2019**, 48, 3683.

[6] a) N. Singh, M. A. Savanur, S. Srivastava, P. D'Silva, G. Mugesh, *Angew. Chem. Int. Ed*. **2017**, 56, 14267; b) B. Yang, Y. Chen, J. Shi, *Adv. Mater*. **2019**, 31, 1901778.

[7] F. Natalio, R. André, A. F. Hartog, B. Stoll, K. P. Jochum, R. Wever, W. Tremel, *Nat. Nanotechnol*. **2012**, 7, 530.

[8] a) L. Gao, J. Zhuang, L. Nie, J. Zhang, Y. Zhang, N. Gu, T. Wang, J. Feng, D. Yang, S. Perrett, X. Yan, *Nat. Nanotechnol.* **2007**, 2, 577; b) G. Y. Tonga, Y. Jeong, B. Duncan, T. Mizuhara, R. Mout, R. Das, S. T. Kim, Y.-C. Yeh, B. Yan, S. Hou, V. M. Rotello, *Nat. Chem*. **2015**, 7, 597; c) A.

Ghosh, S. Basak, B. H. Wunsch, R. Kumar, F. Stellacci, *Angew. Chem. Int. Ed*. **2011**, 50, 7900; d) R. Das, R. F. Landis, G. Y. Tonga, R. Cao-Milán, D. C. Luther, V. M. Rotello, *ACS Nano* **2019**, 13, 229; e) T. Kang, Y. G. Kim, D. Kim, T. Hyeon, *Coord. Chem. Rev.* **2020**, 403, 213092.

[9] a) M. Liang, X. Yan, *Acc. Chem. Res*. **2019**, 52, 2190; b) N. Singh, G. Mugesh, *Angew. Chem. Int. Ed*. **2019**, 58, 7797; c) J. Wu, X. Wang, Q. Wang, Z. Lou, S. Li, Y. Zhu, L. Qin, H. Wei, *Chem. Soc. Rev.* **2019**, 48, 1004.

[10] a) M. Soh, D.-W. Kang, H.-G. Jeong, D. Kim, D. Y. Kim, W. Yang, C. Song, S. Baik, I.-Y. Choi, S.-K. Ki, H. J. Kwon, T. Kim, C. K. Kim, S.-H. Lee, T. Hyeon, *Angew. Chem. Int. Ed*. **2017**, 56, 11399; b) B. Yang, Y. Chen, J. Shi, *Chem. Rev*. **2019**, 119, 4881.

[11] V. Cagno, P. Andreozzi, M. D'Alicarnasso, P. Jacob Silva, M. Mueller, M. Galloux, R. Le Goffic, S. T. Jones, M. Vallino, J. Hodek, J. Weber, S. Sen, E.-R. Janeček, A. Bekdemir, B. Sanavio, C. Martinelli, M. Donalisio, M.-A. Rameix Welti, J.-F. Eleouet, Y. Han, L. Kaiser, L. Vukovic, C. Tapparel, P. Král, S. Krol, D. Lembo, F. Stellacci, *Nat. Mater*. **2018**, 17, 195.

[12] a) M. Chen, D. Kumar, C.-W. Yi, D. W. Goodman, *Science* **2005**, 310, 291; b) J. Zhang, M. B. Vukmirovic, Y. Xu, M. Mavrikakis, R. R. Adzic,

Angew. Chem. Int. Ed. **2005**, 44, 2132.

[13] a) L. Bu, N. Zhang, S. Guo, X. Zhang, J. Li, J. Yao, T. Wu, G. Lu, J.-Y. Ma, D. Su, X. Huang, *Science* **2016**, 354, 1410; b) M. Luo, S. Guo, *Nat. Rev. Mater*. **2017**, 2, 17059.

[14] a) M. H. Oh, T. Yu, S.-H. Yu, B. Lim, K.-T. Ko, M.-G. Willinger, D.-H. Seo, B. H. Kim, M. G. Cho, J.-H. Park, K. Kang, Y.-E. Sung, N. Pinna, T. Hyeon, *Science* **2013**, 340, 964; b) M. H. Oh, M. G. Cho, D. Y. Chung, I. Park, Y. P. Kwon, C. Ophus, D. Kim, M. G. Kim, B. Jeong, X. W. Gu, J. Jo, J. M. Yoo, J. Hong, S. McMains, K. Kang, Y.-E. Sung, A. P. Alivisatos, T. Hyeon, *Nature* **2020**, 577, 359.

[15] C. Y. Kang, H. Kusaba, H. Yahiro, K. Sasaki, Y. Teraoka, *Solid State Ion.* **2006**, 177, 1799.

[16] M. Risch, K. A. Stoerzinger, B. Han, T. Z. Regier, D. Peak, S. Y. Sayed, C. Wei, Z. Xu, Y. Shao-Horn, *J. Phys. Chem. C* **2017**, 121, 17682.

[17] J.-D. Cafun, K. O. Kvashnina, E. Casals, V. F. Puntes, P. Glatzel, *ACS Nano* **2013**, 7, 10726.

[18] N. Singh, M. Geethika, S. M. Eswarappa, G. Mugesh, *Chem. Eur. J.* **2018**, 24, 8393.

Bibliography

1) Myoung Hwan Oh, **Min Gee Cho**, Dong Young Chung, Inchul Park, Youngwook Paul Kwon, Colin Ophus, Dokyoon Kim, Min Gyu Kim, Beomgyun Jeong, X. Wendy Gu, Jinwoung Jo, Ji Mun Yoo, Jaeyoung Hong, Sara McMains, Kisuk Kang, Yung-Eun Sung, A. Paul Alivisatos, and Taeghwan Hyeon "*Design and synthesis of multigrain nanocrystals via geometric misfit strain*" *Nature* **577**, 359–363 (2020). **(Cover article, Press released) (Equally contributed first author)**

2) Sang Ihn Han, Sang-woo Lee, **Min Gee Cho**, Ji Mun Yoo, Myoung Hwan Oh, Beomgyun Jeong, Dokyoon Kim, Ok Kyu Park, Junchul Kim, Eun Namkoong, Jinwoung Jo, Nohyun Lee, Chaehong Lim, Min Soh, Yung-Eun Sung, Jongman Yoo, Kyungpyo Park, Taeghwan Hyeon "*Epitaxially Strained CeO_2/Mn_3O_4 Nanocrystals as an Enhanced Antioxidant for Radioprotection*" *Adv. Mater.* 2001566 (2020). **(Cover article, Press released) (Equally contributed first author)**

3) Sung-Kyun Jung, Hyunchul Kim, **Min Gee Cho**, Sung-Pyo Cho, Byungju Lee, Hyungsub Kim, Young-Uk Park, Jihyun Hong, Kyu-Young Park, Gabin Yoon, Won Mo Seong, Yongbeom Cho, Myoung Hwan Oh, Haegyeom Kim, Hyeokjo Gwon, Insang Hwang, Taeghwan Hyeon, Won-Sub Yoon, and Kisuk Kang, "*Lithium-free transition metal monoxides for positive electrodes in lithium-ion batteries*" *Nat. Energy* **2**, 16208 (2017).

4) Myoung Hwan Oh, Taekyung Yu, Seung-Ho Yu, Byungkwon Lim, Kyung-Tae Ko, Marc-Georg Willinger, Dong-Hwa Seo, Byung Hyo Kim, **Min Gee Cho**, Jae-Hoon Park, Kisuk Kang, Yung-Eun Sung, Nicola Pinna, and Taeghwan Hyeon "*Galvanic Replacement Reactions in Metal Oxide Nanocrystals*" *Science* **340,** 964 (2013). (Highlighted in *Science* Magazine: Maria Ibanez and Andreu Cabot "*All Changes for Nanocrystals*" *Science* **2013**, *340*, 935-934)

초 록

무기 나노 결정의 변형 엔지니어링은 에너지, 자원 및 환경과 같은 전 지구적인 문제를 해결하는 데 필요한 유망한 접근법이다. 서로 다른 재료를 조합하여 이종 구조화된 나노 결정을 생성할 때, 에피택셜 변형된 격자는 이종 계면에 형성될 수 있다. 특히, 나노 규모에서의 변형 효과는 표면의 격자 간격을 변경하고 표면 원자의 전자 구조를 조정하여, 촉매 활성을 변형시킬 수 있다. 변형은 상이한 결정 구조나 결정학적 배향의 기판과 증착상 사이의 격자 부정합에 의해 조정된다. 변형 엔지니어링은 금속, 반도체 및 산화물을 포함한 다양한 재료 조합된 이종구조 나노 결정에서 개발되어 왔다. 그러나 산화물 나노 결정에서의 변형 구조에 대한 연구는 이러한 구조의 합성법이 잘 확립되지 않았기 때문에 제한적이다. 이 논문에서, 더 나은 촉매의 설계를 위하여 표면의 전자 구조 조절에 대한 변형 효과를 연구할 수 있는 모델 시스템을 설계하고 합성했다. 변형된 이종구조 산화물 나노 결정은 종자 매개 성장을 사용하여 제조되었다. 이러한 나노 결정의 독특한 구조는 전자 현미경으로 성공적으로 연구되었다.

이 논문의 1 장은 2 차원 박막 기술의 에피택셜 성장과 3 차원 다면체와의 유사성에 대한 개요이다. 2 장은 고도로 정돈된 멀티 그레인 나노 구조를 생성하기 위한 설계 원리를 설명한다. 원리 발견은 부정합 변형이 유발된 균일한 경계 결함으로 나노 결정을 합성하고, 주사 투과 전자 현미경을 사용하여 나노 미터 스케일에서 변형된 구조를 이미징하고, 변형 장을 측정함으로써 달성되었다. 시드 매개 접근법을 사용하여 입방형 Co_3O_4 결정 코어에서 Mn_3O_4 입자를 성장시킬 수 있다. 기판인 입방체 나노 결정의 면은 쉘의 성장 방향을 안내 할 수 있고, 인접한 Mn_3O_4 입자의 격자 사이에 틈을 생성한다. 이종 에피택셜 변형에 대한 이전의 연구와는 달리, 이 새로운 다결정 나노 결정에서의 입자 경계 결함은 인접한 Mn_3O_4 입자 사이의 기하학적 부정합 변형에 의해 유발되었다. 결함은 코어의 가장자리를 따라 발생하기 때문에 균일한 경계 결함을 달성하기 위해서는 균일한 형상의 코어가 전제 조건이다. 경계 결함 격자 근처의 변형 텐서는 Mn_3O_4 쉘이 전위 없이 경계 결함 당 큰 에피택셜 변형을 수용한다는 것을 보여준다.

3 장에서는 항산화제 적용을 위한 에피택셜 변형된 CeO_2/Mn_3O_4 나노 결정을 제시한다. Mn_3O_4 격자는 CeO_2 와 Mn_3O_4 사이의 큰 격자

부정합으로 인해 상당히 변형된다. 상이한 조성을 갖는 이종 구조화된 나노 결정을 제조하여 표면 산소 공극 및 표면 환원 특성에 대한 변형 효과를 비교, 연구하였다. 향상된 활성산소 제거 능력을 나타내는 변형된 Mn_3O_4 층을 갖는 나노 결정을 이용하여 조혈장 줄기 세포를 방사선 조사로부터 보호할 수 있었다.

주요어 : 에피택셜 성장, 이종구조 산화물 나노 결정, 멀티 그레인 나노 결정, 변형 엔지니어링, 원자 규모 이미징, 전기 촉매.

학 번 : 2012-22587